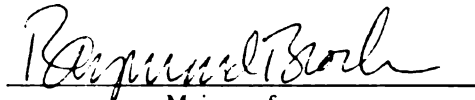This is to certify that the

dissertation entitled

Multimuon Final States in
Neutrino-Nucleon Scattering

presented by

Robert William Hatcher

has been accepted towards fulfillment
of the requirements for

Phd _____ degree in __ Physics __

_____
Major professor

Date January 24, 1994

0-12771

**LIBRARY
Michigan State
University**

DATE DUE	DATE DUE	DATE DUE
_____	_____	_____
_____	_____	_____
_____	_____	_____
_____	_____	_____
_____	_____	_____
_____	_____	_____
_____	_____	_____

MULTIMUON FINAL STATES IN NEUTRINO-NUCLEON SCATTERING

By

Robert William Hatcher

A DISSERTATION

Submitted to
Michigan State University
in partial fulfillment of the requirements
for the degree of

DOCTOR OF PHILOSOPHY

Department of Physics and Astronomy

1994

ABSTRACT

Multimuon Final States in Neutrino-Nucleon Scattering

By

Robert William Hatcher

Results on the production of dimuons in high energy neutrino interactions are presented. The events were observed in the FMMF detector exposed to the FNAL Tevatron wide-band ν beam. The sample of 146 ν_μ and 23 $\overline{\nu}_\mu$ induced $\mu^\mp \mu^\pm$ events with $E_\mu \geq 10$ GeV, $E_h \geq 10$ GeV, and $30 \leq E_\nu \leq 1000$ GeV were observed in the total 45453 ν_μ and 8039 $\overline{\nu}_\mu$ induced charged-current interactions. This signal is analyzed under the assumption of a model of charm production followed by the semileptonic decay of the charmed hadron. A background resulting from decays by ordinary hadrons in the shower is subtracted.

Using the slow-rescaling *Ansatz* the ratio of the strange to nonstrange sea in the nucleon, $\kappa = \frac{2\overline{S}}{U+D}$ was measured to be $0.534^{+0.068}_{-0.066}$ when the charm-to-muon

branching fraction is fixed at $Br_c = 9.3\%$ and the charmed quark mass $m_c = 1.5$ GeV/c^2. Allowing Br_c to float freely gives $\kappa = 0.482^{+0.366}_{-0.193}$ and $Br_c = 9.88^{+2.92}_{-2.87}\%$. When all three parameters are allowed to vary, the best fit is obtained for the parameter values: $\kappa = 0.797^{+0.157}_{-0.147}$, $Br_c = 7.76^{+1.24}_{-1.00}\%$, and $m_c = 1.811^{+0.314}_{-0.296}$ GeV/c^2. The values quoted use the HMRS parton distribution functions for the up and down quarks and the strange-sea shape. A comparison is made to fits using different partons distributions, as well as the next-to-leading order cross section.

The rate of same-sign dimuon production is shown to be consistent with the prediction based on standard π/K decay.

Acknowledgements

Say, from whence
You owe this strange intelligence?
                                   – William Shakespeare [*Macbeth* I, iii]

No man is an island and experiments in high-energy physics are, by necessity, group efforts. In this era of enormous collaborations (> 350 physicists) it is odd to reflect on the fact that this experiment was performed by a group of individuals smaller in number than the list of *institutions* involved in some current experiments. It was nice to actually *know* everyone involved.

With such an small group to draw from, one is often called upon to perform a diverse nature to tasks. I wish to thank all those that taught me the tricks-of-the-trades: plumber, handyman, electrician, digital electronics designer, crane operator, and so forth. At least I learned some useful real world skills. I appreciate those

technicians (Ron Richards, in particular) and others who were so generous with their time. It should also be noted that nothing in a bureaucratic environment ever gets accomplished without the ubiquitous secretaries; thanks to the many that smoothed the way so that I could get some "real" work done.

A list of collaborators can be found in Appendix 6.3. Of course, much of my gratitude goes to my advisor Raymond Brock. He had so much faith in my abilities that he left me to do it my way (maybe a little too often). The details of who deserves extra thanks is too lengthy to list here; many others will have to be satisfied with knowing that they've "done good". Tom Mattison, a hold-over from the previous incarnation of this experiment, deserves credit for the philosophy behind the MHS algorithm that plays such a crucial role in this analysis. He also served as a role model – one *can* be Dr. Doom and still a cheerful, friendly person.

While not strictly the case of "too many scientists and not enough hunchbacks", most of the work on the experiment did fall squarely on the shoulders of the graduate students. I commend Bill Cobau and George Perkins for completing their analyses ahead of myself, and heartily thank these fellow scientist-hunchbacks for their input and contributions to joint efforts. In these two I found camaraderie even on 12 hour owl shifts and early mornings when the temperature hit $-20°F$. The debt I owe these two is too great for words.

As a matter of course, no dissertation is complete without credit given to supportive family members. Since I lacked those .... Seriously, I wish to thank Mom and Dad for *everything* they taught me and for putting such value on learning. You

didn't know what a monster you would create. I am finishing up just so that I never again have to hear the words "So, when are you going to graduate?". Thanks to my siblings for not teasing me too much about my perpetual-student status.

And finally but most importantly, my wife Marina Morrow deserves extra praise for her love and moral support. She possessed the ability to look past the claims of "just one more year" and see a light at the end. I thank her for not becoming too jealous of the computers with whom I often spent more time and for putting up with my late night hours. We met at a Society of Physics Students meeting, but she provides variety and spontaneity to my life with her myriad of other interests. That, along with her ability to discuss serious science topics, makes my life so much more complete.

Contents

List of Tables

List of Figures

Chapter 1

Theory of Neutrino Dimuon Production

I have done a terrible thing, I have postulated a particle that cannot be detected.

– Wolfgang Pauli

Neutrino physics is largely an art of learning a great deal by observing nothing.

– Haim Harari

1.1 Partons and The Standard Model

1.1.1 Overview

Modern elementary particle physics is the study of the fundamental constituents of matter and their interactions. Interactions are described in terms of forces. Four distinct forms of interactions are recognized under current theories. In order of

decreasing strength, along with representative examples in nature, they are:

- **strong:** confining quarks into hadrons; the residual force binds protons and neutrons into nuclei.

- **electromagnetic:** light; radio waves; magnets; atomic binding (chemistry).

- **weak:** β-decay of nuclei; muon decay; neutrino interactions.

- **gravitation:** the attraction between massive particles, and the bending of space-time that affects massless particles.

As one moves from large distances to smaller, any theory must account for quantum mechanical effects. Similarly, as the energies involved grow, so do relativistic effects. In the regime of interest the interactions are best described by a quantum field theory, where fields, rather than particles, interact. No suitable quantum field theory of gravity currently exists, but in the interactions under study the effects of gravity are negligible and thus ignored. The *Standard Model* covers all but gravity.

This thesis makes no attempt to be *the* comprehensive or definitive work on particle physics in general or even neutrino physics in particular. Numerous books provide a more than adequate introduction to the basics of particle physics and the reader is encouraged to read them for a more complete coverage of the subjects reviewed, often at the cursory level, in this chapter[1, 2, 3, 4, 5].

1.1.2 Elementary Particles

Elementary particles are considered to be structureless[1], pointlike[2] particles. The elementary particles/fields (Tables 1.1, 1.2 and 1.3) can be classified as matter and gauge particles. Each particle carries some fixed quantum of intrinsic angular momentum or *spin*. The fields are described by a *wavefunction* that represents the particle's probability distribution.

Fermions (matter) carry half-integral spins ($\frac{1}{2}\hbar$) and obey Fermi-Dirac spin-statistics under interchange of identical particles. That is, the wavefunction ψ that describes the pair is anti-symmetric: $\psi(1,2) = -\psi(2,1)$. This requirement is expressed in the Pauli exclusion principle which forbids two identical fermions from occupying the exact same quantum state. This restriction profoundly affects the nature of many interactions.

Each fermion type has a corresponding anti-particle; these are normally denoted by an overbar above their symbol. All the massive fermions (i.e., all but the neutrinos) can take on either left- or right-handed helicity. Right-handed helicity has the spin aligned with the direction of motion, left-handed antiparallel. In contrast, the massless neutrinos are always left-handed and the anti-neutrinos right-handed.

The gauge particles that mediate forces have integral spin ($\hbar$), obey Bose-Einstein statistics and have symmetric wavefunctions: $\psi(1,2) = +\psi(2,1)$.

---

[1]Actually the continuous emission and reabsorption of photons and fermion pairs, under QED, could be considered "structure" but this is mostly swept under the rug by the renormalization procedure

[2]For example the electron appears to have a size no larger than $\sim 1 \times 10^{-16}$ cm.

Table 1.1: Lepton Properties: fermions, spin $\frac{1}{2}\hbar$

	LEPTONS		ANTI-LEPTONS		
Name	Symbol	Charge (e)	Symbol	Charge (e)	Mass (GeV/c^2)
electron	e^-	-1	e^+	$+1$	0.000511
electron neutrino	ν_e	0	$\overline{\nu}_e$	0	0
muon	μ^-	-1	μ^+	$+1$	0.10566
muon neutrino	ν_μ	0	$\overline{\nu}_\mu$	0	0
tau	τ^-	-1	τ^+	$+1$	1.784
tau neutrino	ν_τ	0	$\overline{\nu}_\tau$	0	0

Table 1.2: Quark Properties: fermions, spin $\frac{1}{2}\hbar$

	Quarks (Baryon# =+1/3)		Anti-Quarks (Baryon# =-1/3)		
Flavor Name	Symbol	Charge (e)	Symbol	Charge (e)	Bare mass (GeV/c^2)
down	d	$-1/3$	$\overline{d}$	$+1/3$	$\approx .007$
up	u	$+2/3$	$\overline{u}$	$-2/3$	$\approx .004$
strange	s	$-1/3$	$\overline{s}$	$+1/3$	$\approx .15$
charm	c	$+2/3$	$\overline{c}$	$-2/3$	≈ 1.1
bottom	b	$-1/3$	$\overline{b}$	$+1/3$	≈ 4.2
top	t	$+2/3$	$\overline{t}$	$-2/3$	> 92

Table 1.3: Gauge Bosons: force mediators, spin $1\hbar$

exchange particle	interaction	interacting particles
γ	E&M	electrically charged particles
$W^{\pm}, Z^0$	weak	quarks, leptons
8 gluons - g_{ij}	strong	quarks, gluons

Quantum numbers, such as electric or weak charge, are carried by the fields. The six leptons and six quarks are each grouped in three pairs (*families* or *generations*), with the non-neutrino constituents increasing in mass with each generation. Members of a family have related quantum numbers that are generally conserved during interactions. Leptons of each family (electron, muon, tau) carry quanta of "lepton number" $+L_i$ ($i = 1, 2, 3$), and their anti-particles carry $-L_i$. Similarly, quarks carry "baryon number" and "flavor". Particles within a quark or lepton family are coupled by the absorption or emission of a gauge boson (Figure 1.1). Weak interactions break the symmetry by coupling members of different quark families (flavor mixing). All the elementary fermions but the top quark have been experimentally verified by either direct or indirect measurement. There are strong theoretical reasons to believe the the last quark family is complete.
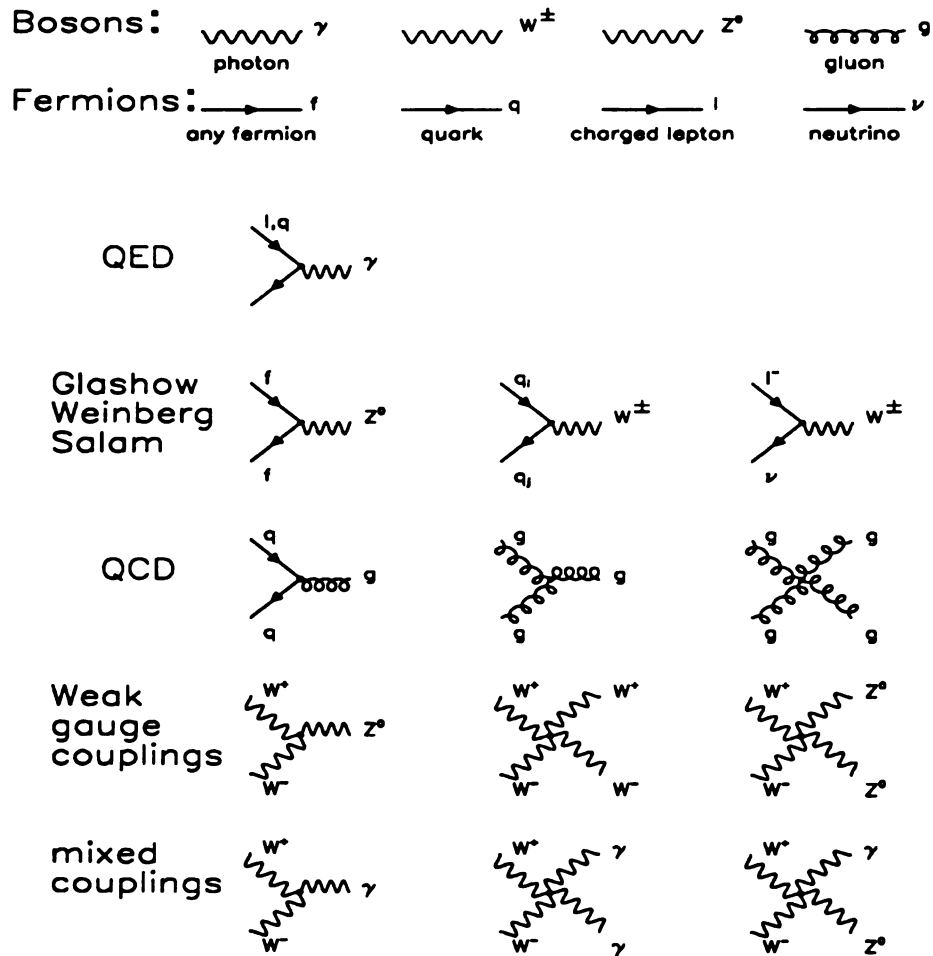
Figure 1.1: Tree Level Feynman Diagrams of Gauge Boson Couplings

1.1.3 QED and the Electroweak Theories

The electromagnetic force is described by the theory "Quantum Electrodynamics" or

QED, where charged fermions couple to the photon (γ) with a strength characterized

by the electric charge e. This theory has the property of *renormalizability* in order

to deal with the emission and reabsorption of virtual photons (and fermion pairs);

the infinities arising from such processes are collected into the "bare" mass or charge

and then redefined by replacing the sum of the two by the physical values. Thus

defined, other divergent integrals in any physical calculation will always cancel.

The weak interaction is the coupling of fermions to $W^{\pm}$ and Z^0's with a strength

characterized by the weak charge g (and $g' = g/\sin\theta_W$). The theories of electromag-

netic and weak interactions were unified by Glashow, Weinberg and Salam in 1967;

the combination is now referred to as the electroweak interaction. This model is a

local quantum gauge theory based on the $SU(2)_L \times U(1)_Y$ gauge group and describe

the interactions among the fermions via γ, $W^{\pm}$, Z^0. Both the dimensionless quan-

tities $\alpha = e^2/4\pi\hbar c$ and $\alpha_w = g^2/4\pi\hbar c$, which represent the coupling strengths, are

small ($\simeq 1/137$, 10^{-5}) and consequently these interactions are dominated by a single

quantum exchange. So-called higher order contributions involving the exchange of

two gauge bosons are thus only a small correction. The higher order effects can

be handled under perturbation theory, similar in principle to a mathematical series

expansion that is truncated after a fixed number of terms.

The process of *spontaneous symmetry breaking*, by means of the Higgs scalar,

give the W$^\pm$ and Z^0 mass while retaining the renormalizability of the theory. The electroweak interaction energy, represented by the Lagrangian density, is:

$$\mathcal{L} = \frac{g}{\sqrt{2}}(J_-^\mu W_\mu^+ + J_+^\mu W_\mu^-) + \frac{g}{\cos\theta_W}(J_{(3)} - \sin^2\theta_W J_{em}^\mu)Z_\mu + g\sin\theta_W J_{em}^\mu A_\mu.$$

The terms represent the weak charged current (CC) with W$^\pm$ exchange, the weak neutral current (NC) involving the Z^0, and the electromagnetic neutral current (EM) involving the photon. The terms W, Z, A represent the gauge boson fields, while the J terms represent the fermion currents. In particular the CC term is of interest:

$$J_+^\mu = (\bar{u}, \bar{c}, \bar{t})\gamma^\mu(1 - \gamma^5)V_{ckm}\begin{pmatrix} d \\ s \\ b \end{pmatrix} + (\bar{\nu}_e, \bar{\nu}_\mu, \bar{\nu}_\tau)\gamma^\mu(1 - \gamma^5)\begin{pmatrix} e \\ \mu \\ \tau \end{pmatrix}.$$

The matrix V_{ckm} represents the *amplitude* of the mixing between quark families that arises in weak interactions. This matrix is nearly unity, but the small off diagonal elements allow for the non-conservation of flavor. The $\gamma^\mu(1 - \gamma^5)$ structure ensures that only the left handed fermions participate in the interaction. This is the $V - A$ coupling. The normal coupling constant for EM interactions is related to the weak coupling constant by $e = g\sin\theta_W$, where the angle θ_W is called the weak mixing angle (or Weinberg angle).

1.1.4 Quantum Chromodynamics

The theory of "Quantum Chromodynamics" (QCD) is a $SU(3)_c$ gauge group describing the strong interactions between quarks by gluons. The quantum number of *color* charge, analogous to electric charge, is carried only by quarks and gluons. Unlike the two types of electric charge, there are three colors and three anti-colors. Quarks carry a quantum of color, anti-quarks carry anti-color, and gluons one quantum of each. Bound systems of quarks are called *hadrons*. One axiom of the theory is that a hadron must have zero net color, i.e. it must be colorless. Baryons, in the naive model, contain three quarks where each carries one of the three colors (that is one red, one green, and one blue quark). Obviously, anti-baryons consisting of anti-quarks are also present in the theory. The most common baryons are the nucleons: protons and neutrons, consisting of *uud* and *udd* quark combinations[3]. Mesons contain a colored quark and a anti-colored anti-quark (such as a red quark and a anti-red anti-quark). The lightest of the mesons are the π meson family ($\pi^+ = u\bar{d}$, $\pi^0 = (u\bar{u} + d\bar{d})/\sqrt{2}$, $\pi^- = d\bar{u}$) and the K meson involving the strange quark.

The major difference between QED and QCD lies in the fact that the gluon can couple to another gluon, while the photon can not directly interact with another photon. This is a direct consequence of the gluon carrying quanta of color, while the photon carries no electric charge. The self-coupling of the mediating gluon field to itself arises from the nature of the underlying non-Abelian $SU(3)_c$ group. A corollary

---

[3]These "net" quarks are called the valence quarks; in addition there are the sundry gluons and quark-antiquark pairs that form a background "sea".

of such a theory, taken in conjunction with the number of fermions and colors found in nature, is the concept of *asymptotic freedom*. This refers to the case where the effective coupling at sufficiently small distances (or equivalently, large momentum transfers) becomes small; while at relatively large (1 fm $= 10^{-15}$ m) distances the coupling becomes very strong – resulting in quark confinement. One can compare the form of the *running coupling constants*, evaluated at a momentum transfer scale Q^2, for QED (starting with an intial scale m) and QCD (initial scale μ):

$$\alpha_R(Q^2) = \alpha_R(m^2) \left[1 + \frac{\alpha_R(m^2)}{3\pi} \log \frac{Q^2}{m^2} + \mathcal{O}(\alpha_R^2) \right] \tag{1.1}$$

$$\alpha_s(Q^2) = \alpha_s(\mu^2) \left[1 + (2n_f - 11N_c)\frac{\alpha_s(\mu^2)}{12\pi} \log \frac{Q^2}{\mu^2} + \mathcal{O}(\alpha_s^2) \right] \tag{1.2}$$

The factors n_f and N_c refer to the number of light quark flavors ($m_q \ll Q/2$) and the number of colors. Substantial evidence exists that there are three colors and there is no evidence for more than six flavors total; the sign of the second term in the QCD formula thus is opposite that of the QED equation. This implies that free quarks are never seen at large scales and all observed bound systems are colorless.

The electroweak theory combined with that of the QCD forms the basis of what is called the "Standard Model". Feynman devised the term *parton* in reference to the quasi-free, pointlike constituents inside hadrons; in QCD these are quarks, anti-quarks and gluons. When probed at small enough distances (high energies, or small Δt) the partons behave as free particles.

1.2   Deep Inelastic Scattering

1.2.1   The Early Years

By 1910 there existed much experimental evidence that atoms contained electrons[4]. Since atoms are normally neutral, it was deduced that they must also contain positive charge equal in magnitude to the negative charge of their collective electrons. A tentative model of the atom proposed by J. J. Thomson was the "plum pudding" model consisting of a sphere of positive charge with electrons uniformly distributed throughout. This model was conclusively proven to be inadequate in 1911 by Ernest Rutherford. Rutherford's experiments involved the scattering of α particles (doubly ionized helium atoms) by atoms. By measuring the angular distribution of the scattered α particles he deduced that positive charge was concentrated in a *nucleus* much smaller in size than that of the atom (now taken to be the cloud of electrons). At these energies the α acts as a structureless particle, and thus can be used to probe the structure of the atom. Logically the next question is: what is the structure of a nucleus[5]? Or more generally, what is the structure of hadrons?

The Rutherford formula predicts the nonrelativistic Coulomb (electric) scattering of two spinless, point particles into a given solid angle Ω. The Rutherford formula may be extended to account for relativistic and target recoil effects (Mott scattering).

---

[4]This is credited to J.J. Thomson, who in 1897, measured the ratio of the charge e to mass m_e by observing the electron's deflection in combined magnetic and electric fields

[5]The "structure" of the electron cloud is what binds, via the Coulomb force, atoms together. Thus, the study of this is in the modern world more properly considered (quantum) *chemistry*. Much of this arises from the Pauli exclusion principle.

The *charge* structure of the nucleons can be characterized using:

$$\frac{d\sigma}{d\Omega} = \frac{d\sigma}{d\Omega}_{\text{Mott}} |F_N(Q^2)|^2.$$

This functional form parameterizes the deviation from the simple expected scattering and thus extracts the interesting physics from the mundane. One starts by defining $\mathbf{k} = (E, \vec{k})$, $\mathbf{k}' = (E', \vec{k}')$ as the 4-vectors of the incoming and outgoing probe. Then one can construct the quantity $Q^2 = |\mathbf{q}|^2$ as simply the magnitude of the 4-momentum transfer of the probe: $\mathbf{q} = \mathbf{k} - \mathbf{k}' = (\nu, \vec{q})$. Because $\vec{q}$ and $\vec{r}$ act as conjugate variables, the measurement of the Nuclear Form Factor $|F_N(Q^2)|^2$ can be seen as the Fourier transform of the nuclear charge density $\rho(\vec{r})$.

$$\rho(R) = \frac{1}{2\pi^2} \int F(Q^2) \frac{\sin qR}{qR} q^2 dq$$

At yet higher energies magnetic scattering becomes important due to spin effects, which leads to the Rosenbluth scattering formula. This involves two form factors (one electric, one magnetic). It is important to remember that these are *elastic* scatterings where the energy of the probe does not change ($\nu \equiv 0$), only the direction. When extended to *inelastic* scattering there is an additional degree of freedom.

At larger energy transfers the probability that the entire nuclei recoils intact is small. It appears that scattering occurs as a quasielastic scattering off individual nucleons (protons and neutrons) within the nucleus. That it is only quasielastic is due to the fact that the nucleons are bound in a potential well and have an associated

Fermi motion. In this case: $\nu \simeq q^2/2M_{\text{nucleon}}$. The cross-section for electron-nucleon can be written:

$$\frac{d^2\sigma}{dq^2 d\nu} = \frac{4\pi\alpha^2}{q^4}\frac{E'}{EM}\left[W_2(q^2, \nu)\cos^2\frac{\theta}{2} + 2W_1(q^2, \nu)\sin^2\frac{\theta}{2}\right]$$

where W_1, W_2 are the (charged) structure functions of the nucleon.

At even larger energy transfers the nucleon no longer recoils unaffected. We begin to "see" the constituents of the nucleon itself, which appear as pointlike *partons*. These latter objects are identified as quarks and gluons.

1.2.2   Deep Inelastic Neutrino-Nucleon Scattering

So far we have dealt with scattering via the electromagnetic interaction. The probe (electron) is unchanged, except in energy and momentum, when it emits a photon that couples to the charged nucleus, nucleon or quark. The concept can be extended to proceed via the weak interaction. The approach of the current experiment is to use point-like neutrinos as a probe of structure of nucleons. Since the neutrino carries no quanta of color or charge, it can interact *only* through the weak interaction[6]. The drawback of using neutrinos as a probe is simply that the weak interaction lives up to its name: *weak*. The neutrino-nucleon cross section is very small ($\sigma \sim E_\nu \times 10^{-38}$ cm²/GeV; ten orders of magnitude smaller than proton-nucleon cross-section at 100 GeV). Literally thousands of millions of neutrinos must pass through a multi-ton

---

[6]At the energy and distance scales involved the effect of gravity can safely be ignored.

detector for even one to have a reasonable probability of interacting.

Neutrino (and anti-neutrino) scattering can occur with the exchange of either a Z^0 or a W^+ (W^-) with a nucleon, N. At large energy transfers one quark in the nucleon is struck so hard that it initially becomes widely separated from the rest of what was a bound system. Since QCD does not allow free quarks to exist, quark anti-quark pairs are created from some of the energy, in a fragmentation chain, that results in a final system of hadrons, X. The details of this final hadronic system are unimportant in general. The reactions

$$\nu_\mu + N \to \mu^- + X \quad , \quad \overline{\nu}_\mu + N \to \mu^+ + X \quad , \quad \overset{(-)}{\nu}_\mu + N \to \overset{(-)}{\nu}_\mu + X$$

are shown pictorially in Figure 1.2(a)-(d). In the last case the (anti-)neutrino is left unchanged except for the momentum 4-vector; this is called *(weak) neutral current scattering*. The first two represent *(weak) charged current* scattering, where the emission of a charged W requires that the neutrino change into its charged lepton partner. From this point on we will restrict our concern to the charged current case.

In the parton model, the nucleon consists of a cloud of electrically charged quarks and neutral gluons interacting amongst themselves. Overall, the nucleon has a net excess of three quarks over the sea of gluons and quark-antiquark pairs. The W boson will couple only to the (anti-)quarks and not directly to the gluons. The W^+ from a $\nu \to \mu^-$ lepton vertex can interact within the nucleon *only* with the charge $(-\frac{1}{3}e)$ quarks (down, strange, bottom), or the $(-\frac{2}{3}e)$ anti-quarks ($\bar{u}, \bar{c}, \bar{t}$) and still

conserve charge and baryon number (Table 1.2).

If life were simple the quarks would transform within their own family in a manner similar to the leptons. Unfortunately, this is not the case. The mass (or physical) eigenstates of quarks are not the same as eigenstates of the weak interaction. This is elegantly expressed in the Cabibbo-Kobayashi-Maskawa mechanism where we have:

$$\text{physical: } \begin{pmatrix} u \\ d \end{pmatrix}, \begin{pmatrix} c \\ s \end{pmatrix}, \begin{pmatrix} t \\ b \end{pmatrix} \text{weak: } \begin{pmatrix} u \\ d' \end{pmatrix}, \begin{pmatrix} c \\ s' \end{pmatrix}, \begin{pmatrix} t \\ b' \end{pmatrix}$$

$$\begin{pmatrix} d' \\ s' \\ b' \end{pmatrix} = \begin{pmatrix} V_{ud} & V_{us} & V_{ub} \\ V_{cd} & V_{cs} & V_{cb} \\ V_{td} & V_{ts} & V_{tb} \end{pmatrix} \begin{pmatrix} d \\ s \\ b \end{pmatrix}$$

This makes the d', s', b' quarks linear combinations of the physical quarks. A particular element V_{cd}, for example, measures the coupling of the d to c quarks. The CKM matrix is nearly the identity matrix and so cross family coupling is suppressed. Experimentally, the magnitudes[7] within confidence limits are given by [6]:

$$\begin{pmatrix} 0.9747 - 0.9759 & 0.218 - 0.224 & 0.002 - 0.007 \\ 0.218 - 0.224 & 0.9735 - 0.9751 & 0.032 - 0.054 \\ 0.003 - 0.018 & 0.030 - 0.054 & 0.9985 - 0.9995 \end{pmatrix}$$

---

[7]the CKM matrix also encompasses a phase (δ) which we will ignore as it contributes nothing to neutrino scattering. This phase characterizes the CP violation in weak interactions. It should be noted as well that the matrix must be *unitary* and so choosing a specific value for one element further restricts the ranges of several others

where the elements are related by the constraint of the "standard" parameterization:

$$
\begin{pmatrix}
c_{12}c_{13} & s_{12}c_{13} & s_{13}e^{-i\delta} \\
-s_{12}c_{23} - c_{12}s_{23}s_{13}e^{i\delta} & c_{12}c_{23} - s_{12}s_{23}s_{13}e^{i\delta} & s_{23}c_{13} \\
s_{12}s_{23} - c_{12}c_{23}s_{13}e^{i\delta} & -c_{12}s_{23} - s_{12}c_{23}s_{13}e^{i\delta} & c_{23}c_{13}
\end{pmatrix}
$$

Here $c_{ij} = \cos\theta_{ij}$ and $s_{ij} = \sin\theta_{ij}$, with i and j being generation labels: $i, j = 1, 2, 3$.

1.2.3 Kinematics

The Feynman diagram in Figure 1.2 schematically describes the charged-current interaction. In the minimal parton model, let us define the following invariant kinematic quantities. The four-momenta and their nucleon rest frame components are:

$$
\mathbf{k} = (E, \vec{k}) = (E_\nu, 0, 0, E_\nu) \tag{1.3}
$$

$$
\mathbf{k'} = (E', \vec{k'}) = (E_\mu, p_\mu \sin\theta_\mu \cos\phi_\mu, p_\mu \sin\theta_\mu \sin\phi_\mu, p_\mu \cos\theta_\mu) \tag{1.4}
$$

$$
\mathbf{P} = (E_N, \vec{p_N}) = (M, 0, 0, 0) \tag{1.5}
$$

$$
\mathbf{X} = (E_h, \vec{p_h}) = \mathbf{p} + \mathbf{q} = \mathbf{p} + (\mathbf{k} - \mathbf{k'}) \tag{1.6}
$$

$$
\mathbf{q} = \mathbf{k} - \mathbf{k'} = \mathbf{P} - \mathbf{X} \tag{1.7}
$$

which represent: incident neutrino, outgoing muon, target nucleon, final state hadron system, and 4-momentum transfer.
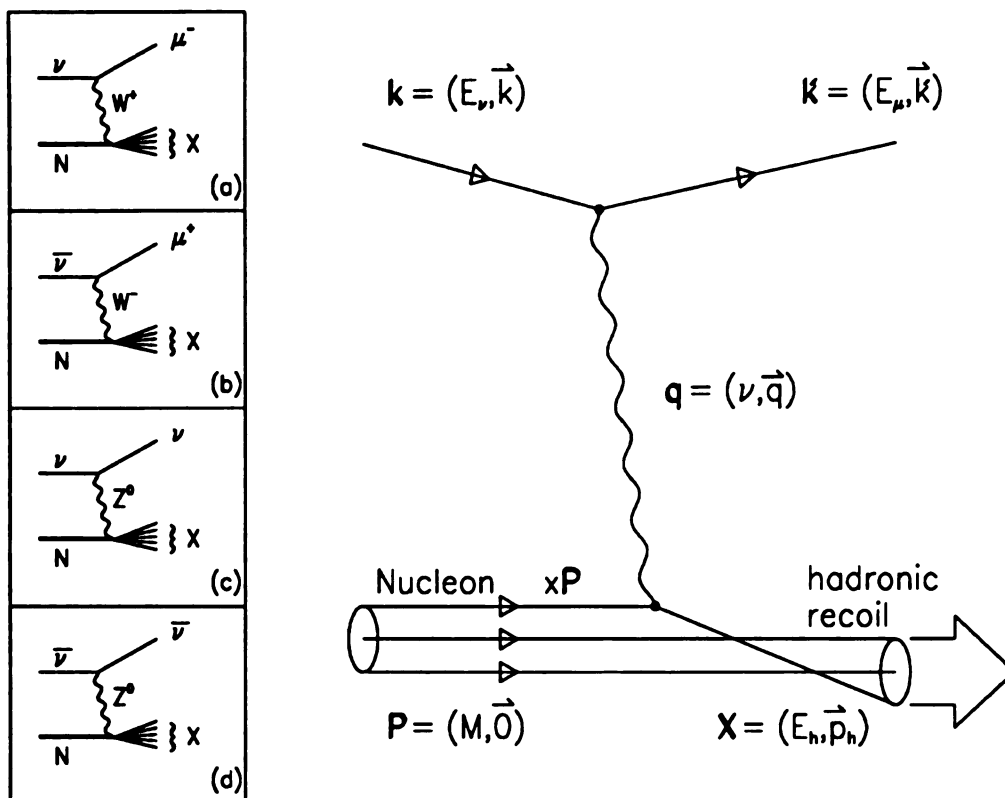
Figure 1.2: Leading order diagrams of neutrino-nucleon deep inelastic scattering.
A pictorial representation of Deep Inelastic Scattering (DIS) is shown with the relevant 4-vectors attached to the components. Sub-diagrams (a) through (d) demonstrate the four possible (anti)neutrino interactions: neutrino and anti-neutrino charged current scattering, neutrino and anti-neutrino neutral current scattering. The struck quark or anti-quark carries xP of the total nucleon momentum, and is assumed to be collinear.

From these we can construct several Lorentz invariant scalar quantities:

$$s = (\mathbf{P} + \mathbf{k})^2 = M^2 + 2ME \tag{1.8}$$

$$\nu = \frac{\mathbf{q} \cdot \mathbf{P}}{M} = E - E' \tag{1.9}$$

$$Q^2 = -q^2 = (\mathbf{k} - \mathbf{k}')^2 = 2(EE' - \vec{k} \cdot \vec{k}') - m_l^2 - m_{l'}^2 \tag{1.10}$$

$$W^2 = (\mathbf{P} + \mathbf{q})^2 = M^2 + 2M\nu - Q^2 \tag{1.11}$$

$$x = \frac{-q^2}{2\mathbf{P} \cdot \mathbf{q}} = \frac{Q^2}{2M\nu} \tag{1.12}$$

$$y = \frac{\mathbf{q} \cdot \mathbf{P}}{\mathbf{k} \cdot \mathbf{P}} = \frac{\nu}{E} \tag{1.13}$$

Several of these have simple physical interpretations: $\sqrt{s}$ is the center of mass energy, ν is the energy transfer to the hadronic system in the lab frame, W is the invariant mass of the hadronic shower. The variable x is the Bjorken scaling variable which, in the minimal parton model, represents the fraction of the total nucleon momentum carried by the struck quark. The inelasticity y is the fraction of energy lost by the neutrino in the lab frame and is related to the scattering angle of the lepton in the center of mass frame. Of these only three are truly independent; the usual combination chosen consists of (s, x, y). It should be noted that given the virtual nature of the exchange boson and the chosen Lorentz metric $\{+, -, -, -\}$, the quantity $q^2 = |\mathbf{q}|^2$ is negative and $Q^2 = -q^2$ is used for notational convenience.

The *Parton Model* takes advantage of the asymptotic freedom of the system, where at high energy transfers the interaction time frame is short enough that there are no inter-partonic exchanges and the struck quark sees only the exchange boson.

This is the *scaling limit* where both ν and Q^2 approach infinity[8]. While interactions that fall very short of these limits are not proscribed by nature, they are not well described by the model. Experimental cuts are used to some degree to exclude these problematic events. The second assumption that is made, and to some degree is broken, is the presumption that the partons are entirely collinear to the proton as a whole. In general the model ignores the transverse momentum (and spin) components.

1.3 Charged Current Cross Sections

Using the charged current Lagrangian and the kinematic formalism from the previous section, in the limit of small lepton and quark masses and lowest order interactions, the charged current cross section can be written in the form:

$$\frac{d^2\sigma}{dxdy} = \frac{G_F^2(s - M^2)}{2\pi(\hbar c)^4} \times \frac{M_W^4}{(Q^2 + M_W^2)^2} \times \qquad (1.14)$$
$$\left\{ [1 - y - \frac{M^2xy}{(s - M^2)}]F_2^{(\overline{\nu})CC} + \frac{y^2}{2}2xF_1^{(\overline{\nu})CC} \pm (y - \frac{y^2}{2})xF_3^{(\overline{\nu})CC} \right\}$$

with M representing the nucleon mass. In the case of neutrino scattering the third term is taken with a positive sign, while for anti-neutrinos it is negative.

The Fermi constant $G_F = 1.6637 \times 10^{-5}(\hbar c)^3$ is related to the weak charge g by $\frac{G_F}{\sqrt{2}} = \frac{g^2}{8M_W^2}$. By appropriately juggling the symbols one can easily show that $s - M^2$

---

[8]Both Q^2 and ν must also be constrained by $0 < Q^2/\nu < 2M$ as required by the definitions and simple 4-momentum conservation.

reduces to $2ME_\nu$ and thus the first part predicts a simple linear relationship as a function of neutrino energy. The factor explicitly involving the mass of the W boson, M_W, represents the propagator term and accounts for the massive nature of the W, currently measured to be 80.40 ± 0.84 GeV/c^2. In fact, the W is so heavy that "real" W's are not actually created, but instead only "virtual" W bosons are exchanged. Such virtual particles do not satisfy the normal relationship $E^2 = p^2c^2 + m^2c^4$, and are said to be "off the mass shell". They are virtual in the sense that they only exist as an intermediate state during the short time period of the interaction.

The structure functions $2xF_1$, F_2, and xF_3 represent the structure of the nucleon. In the scaling limit where ν and Q^2 become large, the naive theory would have these structure functions simply as a function of x. They are normally parameterized as functions of x and and some "scale" that characterizes the process. Traditionally this scale is chosen to be Q, but that choice is not unique.

1.3.1   The Callan-Gross Relationship

In the quark-parton model formalism, the ratio of absorption cross-sections for longitudinal to transverse bosons is defined as R_L and given by:

$$R_L = \frac{\sigma_L}{\sigma_T} = \frac{F_2}{2xF_1}(1 + \frac{Q^2}{\nu^2}) - 1.$$

The value of R_L would be identically zero in the naive quark model and its smallness follows from the spin $\frac{1}{2}$ nature of quarks. In the appropriate limits

$$\lim_{\nu, Q^2 \to \infty} R_L = 0 \qquad Q^2 \ll \nu^2$$

this reduces to the familiar Callan-Gross relationship: $2xF_1(x, Q) = F_2(x, Q)$.

In reality truly infinite Q^2 and ν are not achieved. The $(1 + \frac{Q^2}{\nu^2})$ correction was explicitly kept in the calculated cross sections. There is evidence for a non-zero R_L in the regimes of interest, but no solid measurement and so calculations were performed assuming $R_L = 0$.

1.3.2 Parton Distribution Functions

The structure functions can be further reduced, in the lowest order model, into simple combinations of quark probability distributions. Namely, the quantity $f_q(x, Q)dx$ is the probability that a parton of type q carries a momentum fraction between x and $x + dx$ of the nucleon's momentum in a frame where the nucleon's momentum is large. In this model the structure functions are given by the expressions:

$$F_2^\nu = 2xF_1^\nu = 2x[f_d(x, Q) + f_s(x, Q) + f_{\bar{u}}(x, Q) + f_{\bar{c}}(x, Q)]$$

$$F_3^\nu = 2x[f_d(x, Q) + f_s(x, Q) - f_{\bar{u}}(x, Q) - f_{\bar{c}}(x, Q)]$$

$$F_2^{\bar{\nu}} = 2xF_1^{\bar{\nu}} = 2x[f_u(x, Q) + f_c(x, Q) + f_{\bar{d}}(x, Q) + f_s(x, Q)]$$

$$F_3^{\bar{\nu}} = 2x[f_u(x, Q) + f_c(x, Q) - f_{\bar{d}}(x, Q) - f_s(x, Q)]$$

The bottom and top quarks would play a role analogous to down or strange and up or charm quarks, but are so massive that they can be entirely neglected for the energies available at hand. In general, the Parton Distribution Functions (PDFs) are defined with respect to the proton and those for the neutron are assumed to simply be the result of the interchange of $f_u(x, Q)$ and $f_d(x, Q)$. Traditionally some notational simplification is gained by replacing substituting $a(x, Q)$ for $f_a(x, Q)$ (*e.g.* $f_d(x, Q) \rightarrow d(x, Q)$ and $f_s(x, Q) \rightarrow \bar{s}(x, Q)$).

In the theory of QCD the PDFs are universal across different physics processes, but inherently incalculable in the perturbative expansion scheme. This is the result of the *Factorization Theorem* which provides a scheme for separating out the soft (i.e. low energy) processes that are incalculable in perturbative QCD from the expansion-derived "hard" interactions. The physical cross section $(\mathcal{W})$ is well defined and must be scheme-independent; it is broken down into a convolution of scheme dependent parton cross sections $(\hat{\omega}_q)$ and PDFs:

$$\mathcal{W}(q, P) = \sum_a \int \frac{d\xi}{\xi} f_a(\xi, \ldots) \otimes \hat{\omega}_a(q, \xi P)$$

There are sum rules that relate and constrain the distributions and a relationship that transforms their shapes at $Q = Q_0$ to that at $Q > Q_0$. The evolution of the PDFs (including $f_g(x, Q)$, the gluon PDF) is described quantitatively by a set of coupled differential equations, known as the Altarelli-Parisi equations[7]. One effect of this evolution is the apparent shift towards low x of the PDF at higher Q.

One of the major thrusts of neutrino interaction experiments is to extract as much information as possible about the PDFs, so they can be used as input distribution in other experiments that test alternative aspects of QCD. The variation of the PDFs with Q is relatively small and while accounted for, it will often be dropped from the formalism and the PDFs expressed as a simple function of x.

1.3.3 Spin Structure of the Interactions

The spin and angular structure of this cross section can be most clearly seen when viewed in the center-of-momentum frame. Bear in mind that (anti-)neutrinos come only in a fixed helicity: (right)left-handed[9]. While fermions with a non-zero mass have no fixed helicity, only left-handed quarks and right-handed antiquarks participate due to the $\gamma^\mu(1 - \gamma^5)$ structure of the Lagrangian. The inelasticity y is related to the lepton scattering angle in the center-of-mass frame by $\frac{1}{4}(1 + \cos\theta^*)^2 = (1-y)^2$. The cross section then becomes (neglecting the small terms in the appropriate limits):

$$\frac{d^2\sigma^\nu}{dxdy} \sim [q(x) + (1 - y)^2\bar{q}(x)] \qquad \frac{d^2\sigma^{\bar\nu}}{dxdy} \sim [(1 - y)^2 q(x) + \bar{q}(x)]$$

---

[9] *Helicity* is technically the normalized dot product of the particle's spin and momentum direction vectors: $\lambda = 2\vec{\sigma} \cdot \hat{p} = \pm 1$. For massless particles the terms in $\mathcal{L}$ involving $(1 \pm \gamma^5)$ act to project out (or select) a particular helicity.
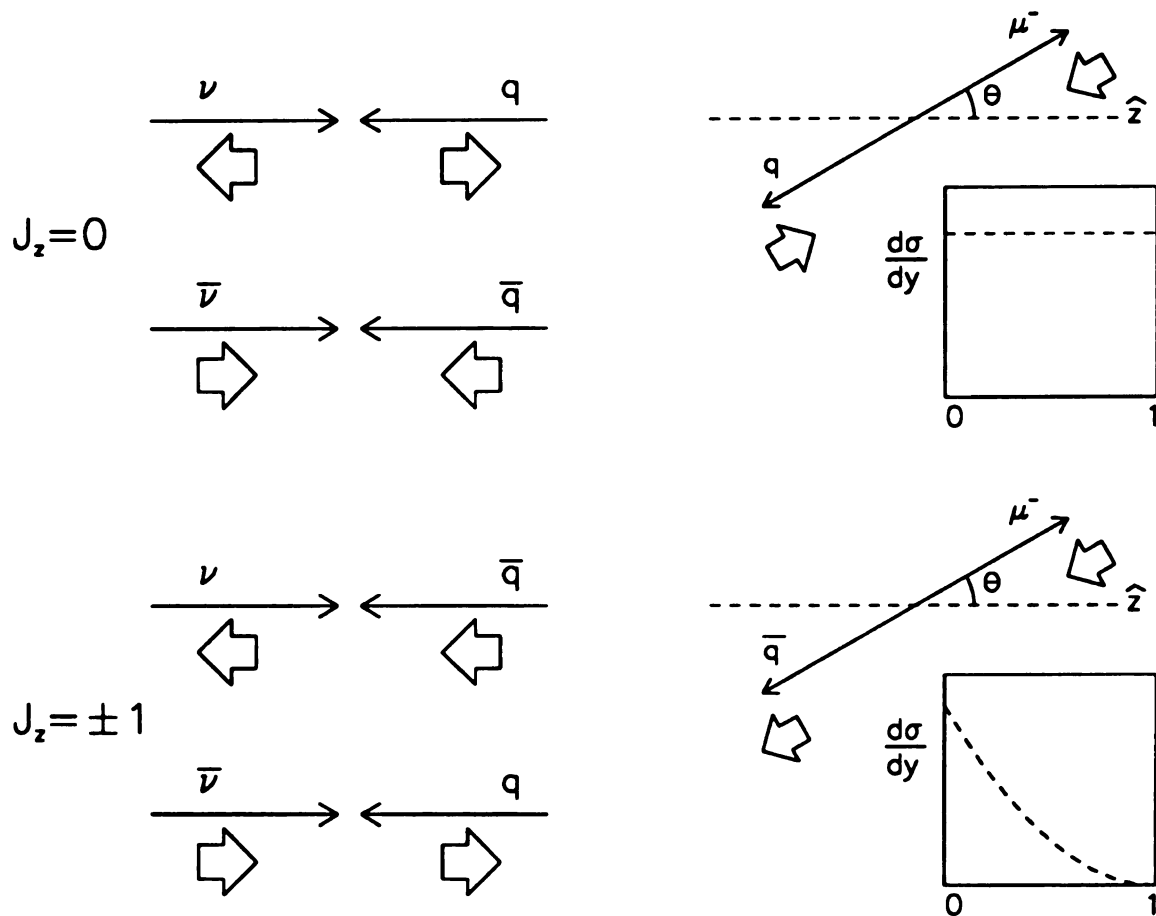
Figure 1.3: The helicity structure of νq interactions.

In the case of νq and $\bar{\nu}\bar{q}$ interaction the net spin $J = 0$ and and thus there is no preferred direction. As a result one would expect an isotropic angular distribution of the end products in the center-of-momentum frame. From the kinematics one can show that $1 - y = (1 + \cos\theta^*)$ demonstrating the flat y dependence. In the $J = 1$ case $y = 1$ would require a complete spin flip from the created intermediate state and is thus forbidden.

1.4 Effects of a Massive Quarks

The two lightest quarks, up and down, are essentially massless relative to the nominal scale ($\Lambda_{QCD} \sim 100 - 200$ MeV) of strong interactions. The strange quark mass is on the same order as Λ_{QCD} which leads to effects that differentiate its PDF from those of the up and down sea (non-valence contribution). But the striking effects appear when discussing charm, bottom, and top quarks, which experimentally have masses of roughly 1.5, 5, >90 GeV, respectively. We will focus mainly on the charm quark, as the last two are for the most part energetically out of reach of this experiment as well as severely suppressed by the CKM mixing mechanism.

The large mass difference between the light quarks and the charm quark implies that there must be some sort of production threshold behaviour. Below threshold it is energetically infeasible to produce the heavy quark. A number of simple parameterizations of this feature were proposed for the Quark Parton Model [8, 9, 10, 11, 12, 13]. The most commonly used *Ansatz* is the *slow rescale mechanism*. This introduces the threshold by scaling the structure functions not by the usual x but by ξ, defined by:

$$\xi \equiv x + \frac{m_c^2}{2M\nu} = x(1 + m_c^2/Q^2).$$

This characterization leaves one free parameter, m_c, which is meant to suggest the charm mass. This formulation ignores target mass and longitudinal structure function effects, which approach the heavy quark effects in some of the regimes of interest. For a more complete criticism of this simplistic (albeit traditional) approach

the reader is directed to work by Tung, *et al.*[14].

The justification of such a scheme is as follows: assume that the struck quark (in this case it must be either a *d* or *s* quark) in the nucleon carries a momentum fraction ξP, where P the the four-momentum of the nucleon. Upon interacting with the W boson of momentum q it produces an on-shell charm quark of mass m_c in the final state. Conservation of four-momenta then requires that

$$(\xi P + q)^2 = m_c^2.$$

Expanding this out, one sees that

$$(\xi P)^2 + 2\xi P \cdot q + q^2 = m_c^2$$

$$\xi^2 M^2 + 2\xi M \nu - Q^2 = m_c^2$$

which leads to

$$\xi \simeq \frac{Q^2}{2M\nu} + \frac{m_c^2}{2M\nu} = x + \frac{m_c^2}{2M\nu}$$

This obviously has the right limit for the case of the massless final state quark, where $\xi \to x$. Thus it is ξ rather than x that is used in the structure functions. Additional restrictions are imposed on this part of the cross section which constrain available phase space by requiring $\xi < 1$ and applying an extra factor of

$$T(x, y, E_\nu) = 1 - y + \frac{xy}{\xi} = 1 - \frac{m_c^2}{2M E_\nu \xi}.$$

These enforce the restrictions

$$x < 1 - \frac{m_c^2}{2M\nu}$$

and

$$\frac{m_c^2}{2ME_\nu} \le y \le 1.$$

Thus the heavy quark production portions of the cross section make the transformation $x f_q(x, Q) \Rightarrow T(x, y, E_\nu)\Theta(1 - \xi)\xi f_q(\xi, Q)$.

Picking out only the charm producing portion of the scattering cross section, we are left with:

$$\frac{d^2\sigma(\nu N \to c\mu^-)}{d\xi dy} = \frac{G_F^2 M E_\nu}{\pi(\hbar c)^4}\mathcal{P}(Q^2)T(x, y, E_\nu)\Theta(1 - \xi) \tag{1.15}$$

$$\xi\left[(u(\xi, Q)f_n + d(\xi, Q)f_p)|V_{cd}|^2 + s(\xi, Q)|V_{cs}|^2\right]$$

$$\frac{d^2\sigma(\bar{\nu} N \to \bar{c}\mu^+)}{d\xi dy} = \frac{G_F^2 M E_\nu}{\pi(\hbar c)^4}\mathcal{P}(Q^2)T(x, y, E_\nu)\Theta(1 - \xi) \tag{1.16}$$

$$\xi\left[(\bar{u}(\xi, Q)f_n + \bar{d}(\xi, Q)f_p)|V_{cd}|^2 + \bar{s}(\xi, Q)|V_{cs}|^2\right]$$

The term $\mathcal{P}(Q^2)$ represents the propagator factor

$$\mathcal{P}(Q^2) = \frac{M_W^4}{(Q^2 + M_W^2)^2} \approx 1$$

as previously discussed. The mixed nature of the target nucleons (protons,neutrons) is expressed in the terms f_p and f_n ($f_p + f_n = 1$) which represent the fraction of the targets of each type. This assumes an isospin symmetry.

A quaintly written article by de Rùjula *et al.*[15] discusses the probable effects of the existence of the charm quark and some of the properties involved in neutrino production, *before* it was even first observed via the J/ψ in e^+e^- collisions. As well as the threshold induced by the "slow rescaling" mechanism, they make it clear that threshold must exist to account for the mere production of the charmed hadron. They introduced this as a simple theta function: $\Theta(W - M_h)$. This "fast rescaling" principle insists that the recoil system mass must be sufficient to produce the heavy hadron. In general one is unlikely to produce a charmed baryon, and instead the requirement is for light baryon (the proton being the lightest) and a light charmed meson (the D meson). This can be expressed by the simple restriction:

$$W^2 > (M_p + M_D)^2 = (2.803)^2 = 7.855 \text{ GeV}^2.$$

This same paper anticipated the use of opposite-sign dimuons as an indicator of charm production two year prior to the experimental observation of the signal.

At this stage it would be prudent to make a few pertinent observations.

- In the limit that the heavy quark mass is negligible these cross sections lose their dependence on y. It is primarily the threshold behaviour that is responsible for deviations of the physical cross section from a flat distribution. The PDF evolution as a function of Q introduces a small additional slope towards lower y values. Cuts must be applied to the measured quantities to exclude poorly measured regions; these further mask the underlying y independence in

the observed distributions. The distributions of E_ν, x, and y derived from the model will all have some dependence on the parameter m_c.

- It has been observed that the CKM matrix is nearly the identity matrix with $|V_{cd}|^2 \ll |V_{cs}|^2$ ($|V_{cd}|^2 \simeq .0484$ and $|V_{cs}|^2 \simeq .9494$). Thus it is reasonable to expect that the majority of the $\bar{\nu}$-induced anti-charm events will originate from the scattering off anti-strange quarks in the nucleon. This holds true as long as the strange sea is roughly the same size as the non-strange sea.

- On the other hand, for a neutrino scattering scattering off a nucleon there are all the d valence quarks in addition to the d and s sea quarks. Experimentally it has been shown that the valence quarks carry roughly one third the total momentum of the nucleon; less than 20% is carried by sea quarks with the remainder carried by gluons. For an isoscalar target (equal numbers of protons and neutrons) we then expect that roughly half of the charm production will come from non-strange scattering.

1.5 Strange Sea Content of the Nucleon

A world where the sea contribution of u, d, and s quarks were equal would be characterized as a $SU(3)$ flavor symmetry. The breaking of this symmetry can crudely

be expressed by a single value κ. One defines

$$U = \int x u(x) dx \qquad D = \int x d(x) dx$$

$$\overline{U} = \int x \bar{u}(x) dx \qquad \overline{D} = \int x \bar{d}(x) dx$$

$$\overline{S} = S = \int x s(x) dx$$

the last line takes into account the net non-strangeness quality of the nucleon. It is then straightforward to define

$$\kappa = \frac{2\overline{S}}{\overline{U} + \overline{D}} \quad \text{and} \quad \eta = \frac{2S}{U + D}. \tag{1.17}$$

Then κ is simply the fraction of strange quarks relative to the non-strange quarks in the sea (ignoring the heavier quarks). A value of $\kappa = 1$ would indicate a fully $SU(3)$ flavor symmetric sea, while $\kappa = 0$ indicates the total lack of s quarks. Experimentally κ has been previously measured to be in the range 0.3 – 0.9. The lower to mid-range values are indicative of the direct measurements via neutrino dimuon interactions [16, 17, 18, 19, 20]. The high end of the range is preferred by some global analyses fits using a wider sample of data sources, cf. [21]. This statistically significant discrepancy is the cause of some concern.

1.6   Opposite Sign Dimuon Events

Once produced, the charm quark and nucleon remnants must fragment into a hadronic system composed of colorless particles. This complex process is incalculable using

perturbative QCD and must be modelled phenomenologically. It is normally characterized by a fragmentation function $D_c^H(z)$ which represents the probability of the charm quark c becoming a hadron of type H carrying $z = E^{hadron}/E^{quark}$ of the intial charm quark energy. The dependence of the fragmentation on z alone, independent of the quark's previous history, is part of the *factorization hypothesis*. The end result is a single charmed hadron (most likely a D or D* meson) amongst a throng of other hadrons. Unless one had a means of inspecting each hadron individually there would generally be no hope of distinguishing the charm producing events from less interesting events.

Detailed measurements of hadrons in the recoil system are generally impractical. A detector large enough to give reasonable interaction rates would be prohibitively expensive to instrument with sufficient resolution to distinguish a charmed hadron from a prosaic uncharmed one. Alternatively one could choose an indicator that preferentially tagged charm events. One obvious characteristic of charmed hadrons is their relatively short lifetime. Even boosted to high energies (in the lab frame), they do not travel very far before decaying. In roughly 10% of the cases the charmed hadron will semi-leptonically decay into a muon, a neutrino and pions or kaons. The sign of this "secondary" muon will always be opposite that of the "primary" muon resulting from the $\overset{(-)}{\nu} \rightarrow \mu^{\mp}$ lepton vertex. The muon signature is easily recognizable in the laboratory, thus the presence of a second muon acts as a tag. This works because the rate of interactions of the ordinary hadronic debris with the detector is much larger than the probability of those hadrons (generally pions and

kaons) decaying into muons. One defines the branching ratio Br_c as the relative rate of the direct decay of a charmed hadron into any state containing a muon:

$$Br_c \equiv \frac{\Gamma(H_c \to \mu\nu X)}{\Gamma(H_c)}$$

The relatively low branching fraction Br_c means that the majority of the actual charm producing events are indistinguishable from other events and thus "lost".

From the point of view of this model, the production of dimuon events can be seen as a three step process: the production of a charmed quark by a W boson scattering from a quark in a nucleon, the fragmentation of the charm quark into a charmed hadron, and the subsequent decay of the hadron into a muon. Thus the final dimuon cross section can be characterized by the equation (for neutrinos)

$$\frac{d^3\sigma(\nu N \to \mu^-\mu^+ X)}{d\xi dy dz} = \frac{d^2\sigma(\nu N \to c\mu^- X')}{d\xi dy} D_c^H(z) Br_c(H \to \mu^+\nu X'') \tag{1.18}$$

Experimentally the $\mu^-\mu^+$ cross section is measured to be $\simeq 1\%$ of the total charged-current cross section above 200 GeV[20, 19].

Chapter 2

Apparatus

*The fundamental principle of science, definition
almost, is this:* sole test of the validity of any
idea is experiment.

— Richard P. Feynman

The execution of this experiment depends on two major pieces of equipment: a source of neutrinos and a detector to measure the properties of their interactions with nucleons. Here the detector also acts as the source of target nucleons.

2.1 Particle Beam Sources

2.1.1 The FNAL Accelerator System

Neutrinos and antineutrinos used by this experiment were produced as a tertiary wide band beam by protons extracted from the Tevatron at the Fermi National

Accelerator Laboratory (FNAL). The protons that form the primary beam were raised to an energy of 800 GeV[1] in a multi-step fashion. This was necessitated by the wide range of RF (radio frequency) and magnetic fields required to bring protons essentially at rest to within 1 part in 10^6 of the speed of light. An overview of the physical relationships between the large scale components can be found in Figure 2.1. The FMMF detector was located in Lab C.

☐ Negatively charged ions of hydrogen (H⁻) were produced in the *ion source*. This was accomplished by interactions with a hot cesium cathode. Electrons liberated from the cesium became loosely bound to the molecular hydrogen gas.

☐ These ions were then whisked away and accelerated to energies of 750-800 KeV by a Cockroft-Walton electrostatic accelerator.

☐ The next stage is a 150 m long linear accelerator, which brings the energy up to 200 MeV using an array of high frequency RF cavities. As the ions exit the linac they pass through a thin carbon foil which strips off both electrons.

☐ The positively charged protons enter the "Booster" synchrotron which *boosts* the protons from 200 MeV to 8 GeV. This small synchrotron is a ring of magnets 500 m in circumference.

---

[1]It is conventional in the field to speak about energies in terms of eV (electron Volts), the energy gained or lost moving an particle with the charge of one electron through a 1 Volt potential. Often this notation is carried over, though strictly incorrect, to referring to momenta and masses as well. For momenta and masses the dimensionally correct quantities are eV/c and eV/c², respectively. But as all High Energy physicists know $c = 1$ in the *appropriate* units, and the references to c are often dropped for notational convenience.
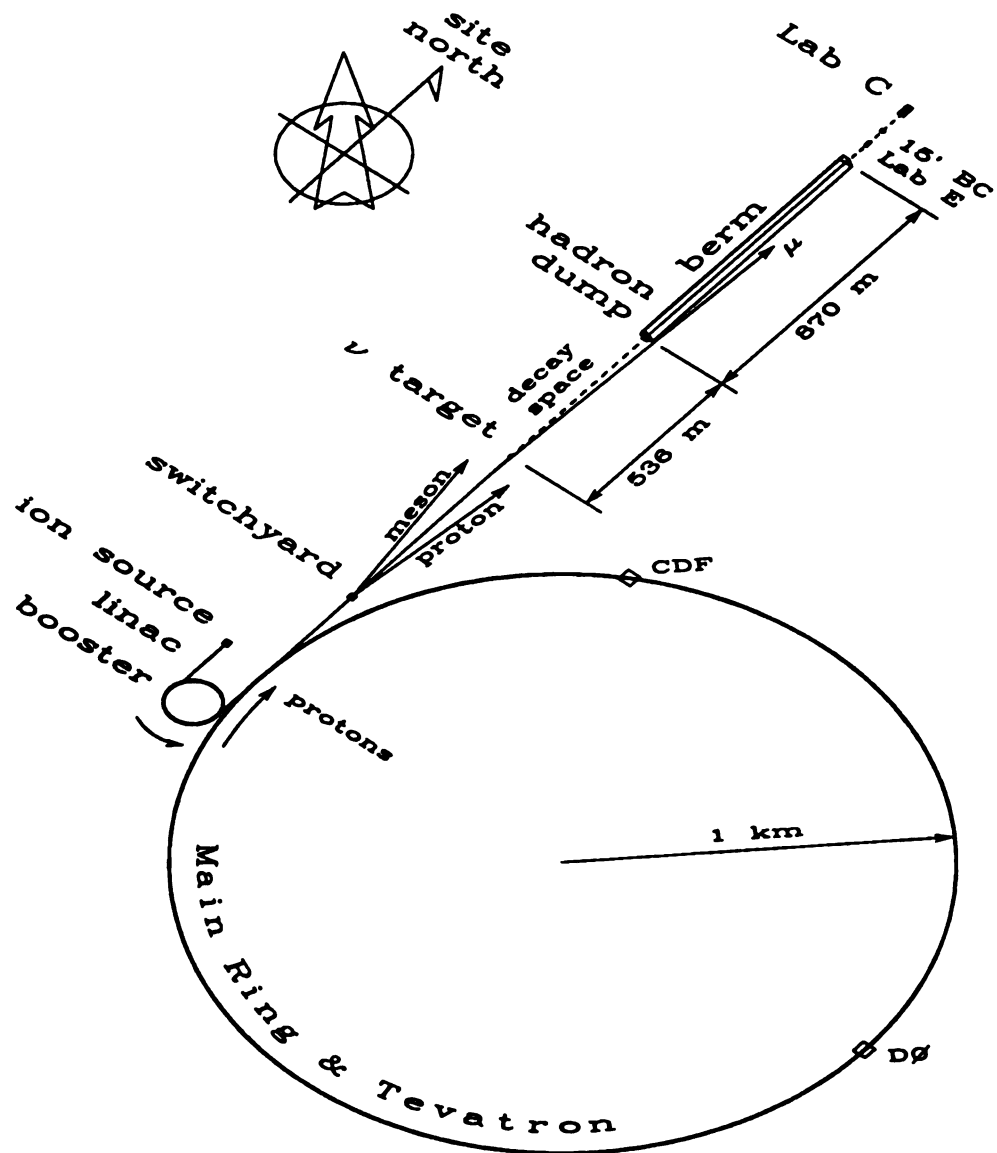
Figure 2.1: The FNAL Tevatron accelerator and neutrino beam line.

❑ The relativistic protons were extracted from the Booster and injected into the "Main Ring" synchrotron. The Main Ring consists of more than 1000 conventional copper-wire wound iron magnets located in a tunnel 6.3 km in circumference. The Main Ring is capable of energies up to 500 GeV, but with the addition of the Tevatron accelerator it was operated a lower energy (150 GeV) to save on electrical costs. The beam in the Main Ring is structured not as a continuous stream of protons, but rather as 12 circulating *buckets* or bunches.

❑ In the final acceleration step the protons were injected into the "Tevatron" superconducting synchrotron. The Tevatron ring of magnets hangs 64 cm below those of the Main Ring in the same 1 km radius tunnel. These more powerful magnets (40 KGauss) allow containment of higher energy beams, without the large dissipative current losses found in conventional magnets. During the two neutrino data-taking runs the Tevatron did not run at the full 1 TeV energy, but instead at 800 GeV. The beam sub-structure in the Tevatron consists of buckets 2 nanosecond wide separated by 18.8 nsec.

  • Once injected into the Tevatron the magnet currents and the RF were ramped up to their final values over a 10 second period (Figure 2.2). Upon reaching the operating energy the particles were ready for extraction. The period of constant proton energy was referred to as "flat-top". Two modes of extraction occurred during flat-top: *slow spill* and *fast spill.*

  • Slow spill was the gradual extraction of a small fraction of the beam over an approximately 23 second period. These protons were then distributed

Accelerator cycle $(Tl_{i+1} - Tl_i)$ ~ 60 sec   time ———————▶

                        10 sec

Tevatron Beam Energy

∝ magnet current   *flat top*

    T1   T2   T5   T6   T7

                          fast extraction "pings"

Accelerator
Beam Intensity

    slow spill extraction
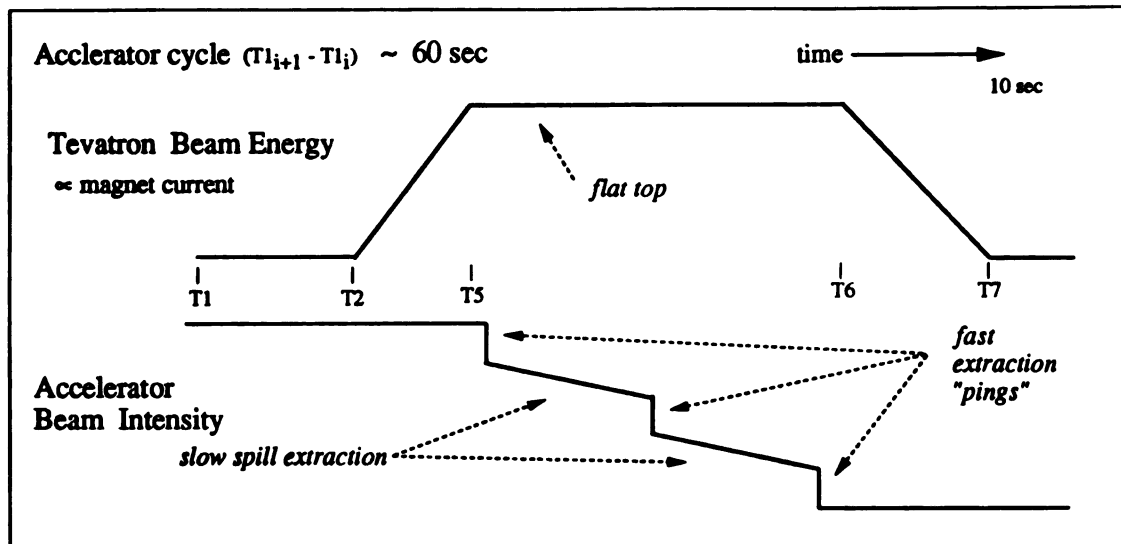
Figure 2.2: Tevatron Fixed Target Spill Structure

Magnet currents (field strengths) were proportional to proton energies. Beam current shows slow decline during normal extraction, and sudden losses during the three fast extraction periods.

to various parts of the lab by the proton switchyard. One of the destinations of this beam was the target that formed the beginning of the NH secondary beam line (Figure 2.6); this lower energy beam was used in this experiment for calibration and decay rate studies.

• The fast spill pertained only to the neutrino beam line which is discussed in detail below.

2.1.2 The Neutrino Beam

The NC neutrino beam was only operative during the fast resonant extraction phase. Fast extraction consisted of approximately 2×10^{12} protons (about 10% of the total) being kicked out of the Tevatron during a few millisecond window. Within this

time frame all the extracted beam was directed down the NC beam line. These *pings* occurred 3 times during the flat-top. Following the final ping, the accelerator magnets were ramped down over a 10 second period; the cycle repeated approximately every 60 seconds (Figure 2.2). Protons extracted during the pings constituted the *primary* beam. This beam was focussed to a 2 mm spot on a target composed of a 14 cm of beryllium oxide powder (in the form of 8 pellets). Within the target a multitude of secondary particles were generated; the more stable of these exited the target with some angular spread. The low atomic number Z of the target minimized angular dispersion and secondary interactions.

A collimator following the target eliminated high angle and low energy particles from the beam. The remaining secondary particles were collected by the *quadrupole-triplet* (QT) magnet train. The quad-triplet actually consisted of 4 (rather than 3) quadrupole magnets forming the focussing elements. The magnet configuration provided point-to-parallel optics for secondaries at 300 GeV. Secondaries at other energies are either over or under focussed but are not stopped. The lack of momentum or secondary sign selection is what characterizes this as a *wide band beam* neutrino source. Primary protons that did not interact continued down the beam pipe along with the secondaries.

The particles traveled through a series of evacuated pipes of increasing diameter (12", 16" and 30"). While in flight some of the secondary kaons and pions decayed resulting in neutrinos and antineutrinos. Hence the term *tertiary beam* from the decay of secondary particles. Other decay products accompanied the neutrinos:

leptons ($\mu^{\pm}$ and $e^{\pm}$) and for each three-body decay of a kaon an additional π^0. Since there was no momentum selection of the secondaries, even the two-body decays resulted in a broad energy spectrum of neutrinos (Figure 2.3)[2]. The available decay space was 536 meters long. At the end of this tunnel was a hadron beam dump, where the remaining primary and secondary particles are deposited into a aluminum and steel block to be absorbed. An additional 870 m of iron and earth shielding constituted the *berm*. The berm absorbed the majority of the muons produced as well as all of the particles escaping the dump.

The QT beam has the advantage of providing a high flux of neutrinos, but at the loss of some systematic controls:

- With a quasi-monochromatic beam there is a strong correlation between the vertex radius (from beam center) and the neutrino energy. In the case of a QT beam one must rely entirely on the reconstructed visible energy. This is wrought with resolution effects as well as systematic effects. It is obvious for Neutral Current (NC) interactions the available information is incomplete, as the out-going neutrino is unmeasured. Similarly in dimuon events there is an unobserved neutrino from the charmed quark decay.

- Since there was no sign selection of the secondary pions and kaons, events originate from both ν and $\bar{\nu}$ interactions. For opposite sign dimuon events this means that an event can not be unambiguously identified. A classification

---

[2]Alternatively a *narrow band* or momentum selected secondary beam results in an quasi-monochromatic neutrino beam for those originating from 2-body decays.

must be assigned using a selection algorithm; such an algorithm can be tested using models (MC) available but leaves some uncertainty in the assignment.

- No attempt at direct flux measurement was made. Thus one can only measure the cross section relative to the single muon cross section.

Some of the characteristic features of QT neutrino beam are demonstrated in Figures 2.3 and 2.4. The dominance of the flux by π decay is obvious. The correlation between E_ν and radius from the beam center is not as distinct as in a narrow-band beam, but exists never-the-less. These plots are for (anti-) neutrinos passing through the fiducial volume of the detector (Section 4.9).

Monitoring devices placed in the beamline provided intensity and position measurements of the primary and secondary beams. A combination of wire chambers and wire SEM (secondary emission monitors) supplied steering information. A toroidal inductor surrounding the primary beam line was the fundamental measure of the proton intensity. A processed and discriminated signal derived from the toroid pulse monitor became the *dynamic beam gate* (DBG) which signaled that neutrinos should be arriving at the detector. This signal was used in conjunction with a simple timing gate tied to the accelerator cycle to determine the trigger window (Figure 2.5).

2.1.3   The Calibration Beam

In addition to the neutrino beam, an auxiliary beam of either hadrons or muons was brought in to the front of the detector. These particles of known energy were used
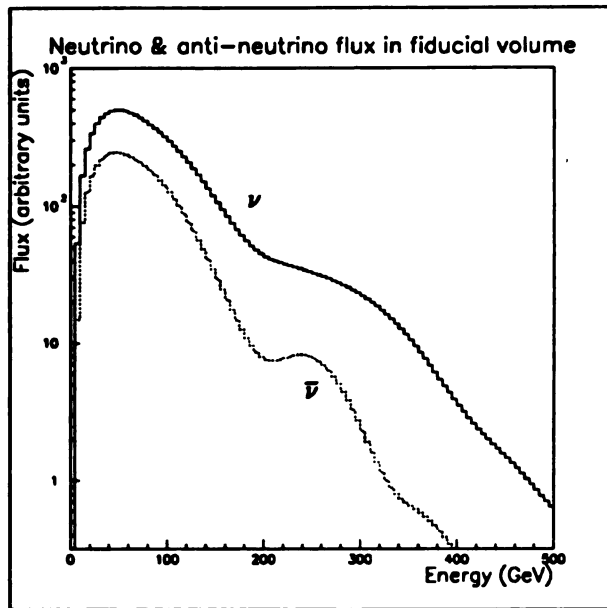
Figure 2.3: Flux spectrum of ν and $\bar{\nu}$ beams.
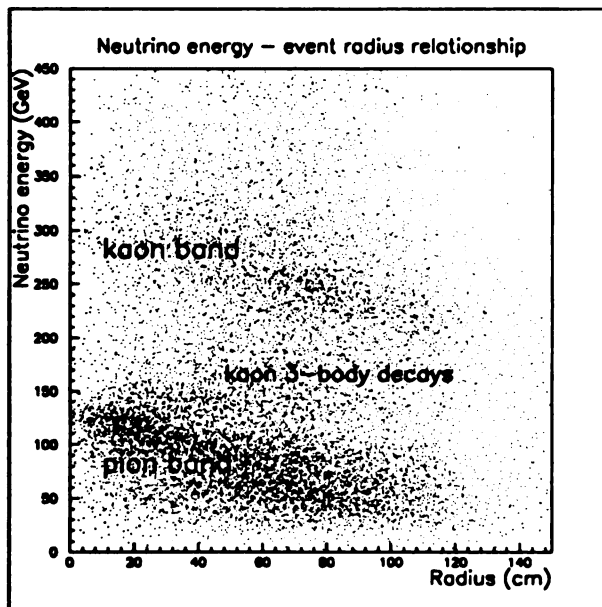
Figure 2.4: Relationship between ν energy and radius at the detector.
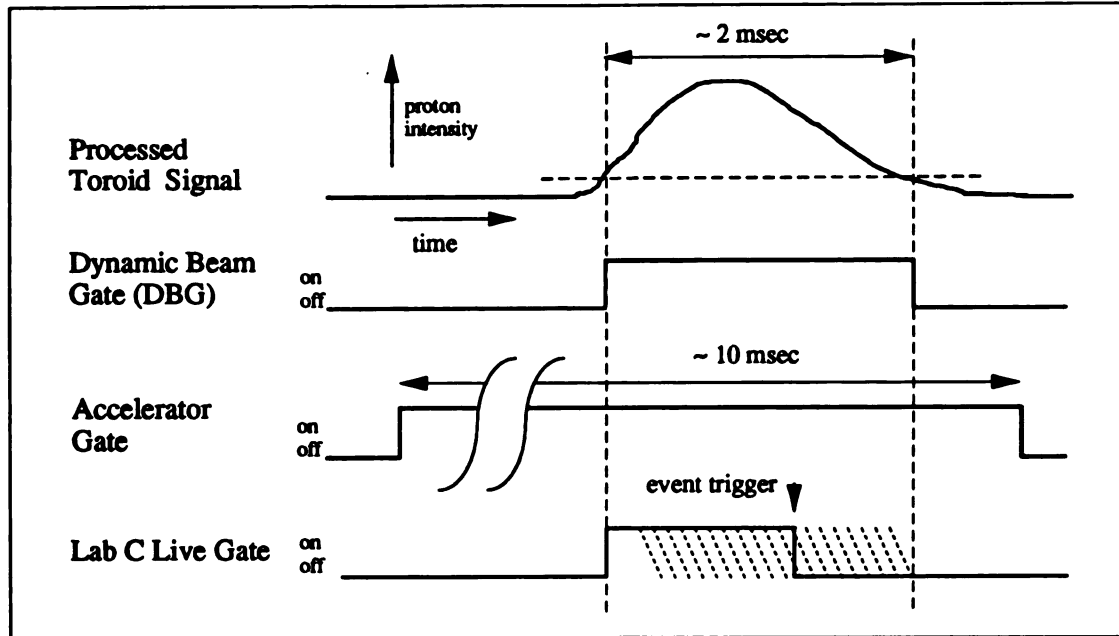
Figure 2.5: Fast Extraction Proton Toroid signal and Dynamic Beam Gate

to calibrate the energy scales of the detector. They also provided a mechanism for studying some of the other features of the detector and cross checks on reconstruction algorithms. The NH beamline layout can be found in Figure 2.6. A slow, steady trickle of these secondary particles entered the front face of the detector between the neutrino spills. At any given time the magnet currents were set to accept particles of energies in the range 25 to 400 GeV with a momentum bite of $\delta p/p \approx 3\%$ full width at half maximum. When the beamline was configured for muons the intensity was increased and a large aluminum block was rolled into place to act as a beam dump to remove the hadrons. Throughout the 1985 run the beam angle was fixed at 69 mrad west off the detector axis; during the 1987-88 run additional dipole magnets provided a mechanism for control, albeit limited, over the entry angle and position of the beam. Requiring a coincidence signal from a series of scintillator paddles ensured

that the particle had traversed the prescribed path and was therefore of the right energy.

Two Čerenkov counters in the beam line provided a cross check on the momentum selection. They were also used in an attempt to identify the particle type by setting parameters so as to differentiate between π, K, μ and electrons. These counters consist mainly of a large tube filled with a transparent gas (typically nitrogen or helium) that acts as a radiator. The gas has an index of refraction (n) dependent upon the gas type and density. The Čerenkov radiation (light) is emitted at an angle

$$\cos\theta = \frac{1}{\beta n}, \quad \beta > \frac{1}{n}$$

whenever the incoming particle velocity βc exceeds speed of light in a dielectric medium (c/n). The light is collected using mirrors and focussed onto photomultiplier tubes to give a signal proportional to the light intensity. A scan of response as a function of pressure resulted in a characteristic curve where the threshold was crossed for different particle types (Figure 2.7). The downstream counter was a differential counter that could discriminate between two different particle masses by selecting an angular range of the collected light.

2.2 Detector Overview

The E733 Lab C detector was located approximately 1 km downstream from the end of the decay tunnel. The detector consisted of three main components: the

Beam Lines to Lab C

- N-Center Neutrino beam line
- NH calibration beam line

v Detectors

Lab C: (FMMF)

Lab A: 15-foot Bubble Chamber

Lab E: (CCFRR)

Lab F: Tohoku Bubble Chamber

870 meters of steel & soil to filter out all but neutrinos

BEAM DUMP

Shielded pipe for decay of secondaries to v

Split to N-West

"Quad Triplet" focuses secondary particles from proton interactions in target

Target moves in for fast spill (v), out for slow spill to N-West

steering/focus onto target

Beam monitors

passive Aluminum beam-shield

beamline split: NC (magnet on) NE (magnet off)

steering/focus into Neutrino Area

v line

proton beam from switchyard

ON: slow spill
OFF: fast spill

Beam pipe through Bubble Chamber Yard, Cerenkov counter and final bend magnet

Lab E pad dipoles

Cerenkov counter in Lab F

Movable beam dump for choosing hadrons or muons

Beam pipe through berm to Lab F

Final focus in NEB for path around Lab E on the way to Lab C

NT to Lab E

NH to Lab C

NE/NT/NH beamlines

Magnets and devices steer and split the slow-spill beam, which hits a target in enclosure NE8, producing secondaries. Once tuned to a desired momentum, the NH beam splits from the NT beam in enclosure NEB and heads for Lab C.

NOTES:

Figures are not to any consistent scale.

Most beam position and intensity measuring devices are not shown for either beam line.

Magnet symbols may represent groups of magnets rather than single magnets. Polarity/orientation of magnet symbols is for the sole purpose of showing that they are not all the same; no specific identification is intended..

LEGEND

quadrupole magnet (two polarities)

dipole magnet (two orientations)

beam shield/ collimator

Figure 2.6: Schematic layout of beam line to Lab C

Diagrammatic representation of the general features of the beams entering Lab C. The N-Center beamline provides the source of ν and $\bar{\nu}$, and forms a straight line from the switchyard. The NH beam provided the calibration beam of hadrons and muons. The NH line was offset from the NC line to avoid most of the berm and in order not to interfere with decay space. [22]
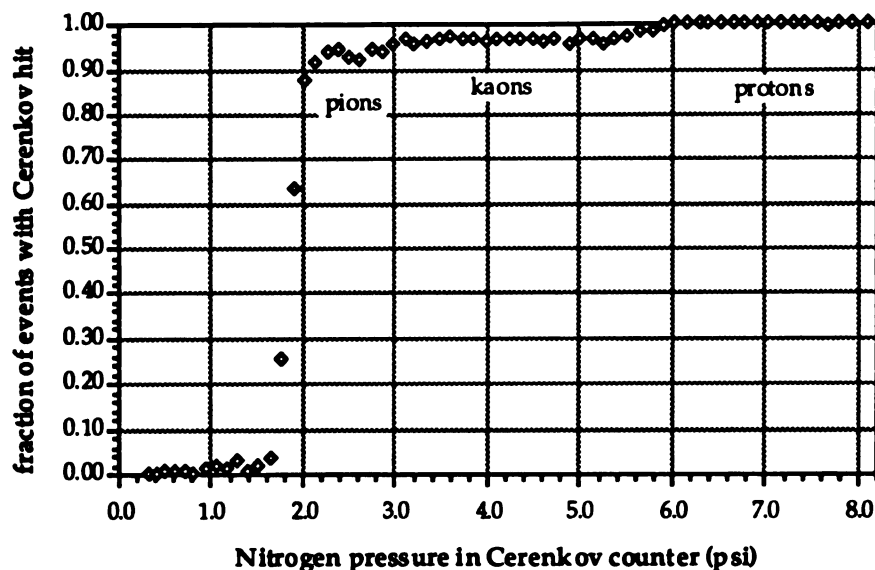
Figure 2.7: Čerenkov counter response-vs-pressure curve

The sensitivity of Čerenkov counter to particles in the beam as the nitrogen pressure increases is shown. The gas temperature was kept constant; the index of refraction changed with density. As the density goes up particles of higher mass cross the threshold for Čerenkov light production.

fine grained tracking calorimeter, the muon spectrometer, and the beam muon veto wall. The calorimeter provides target material for the neutrinos and allows one to measure many characteristics of the interaction: longitudinal and lateral vertex position, hadron energy and angle, and muon identification and angle. It also allowed one to track muons to the exit of the calorimeter in order to "point" their trajectories downstream into the spectrometer. The muon spectrometer was used to measure the energy of the outgoing muons. These two elements provide sufficient measurements to reconstruct the event parameters. The veto wall was located in front of the calorimeter and consisted of fast detector elements that permitted the rejection of potential triggers caused by muons entering the detector. Such muons may be the result of either the secondary decays or upstream neutrino interactions. The general

Table 2.1: Overall Detector Properties

$$\Lambda_{abs} = 85 \text{ cm} \qquad \langle \rho \rangle = 1.35 \text{ g} \cdot \text{cm}^{-3}$$
$$X_0 = 14 \text{ cm} \qquad \langle Z \rangle = 9.8$$
$$E_{crit} = 38.9 \text{ MeV} \qquad \langle A \rangle = 20.2$$

$$\text{FiducialMass} \simeq 100 \text{ metric tons}$$
$$\text{proton/neutron} = .942$$

Detector	Segmentation Transverse	Segmentation Longitudinal	Sampling X_0	Sampling Λ_{abs}
Flash Chamber	6 mm	3.2 cm $(4.3 \frac{g}{cm^2})$	0.22	0.04
Prop Tubes	10 cm	46 cm $(67.5 \frac{g}{cm^2})$	3.5	0.59

detector characteristics are presented in Table 2.1. A schematic representation of the detector is shown in Figure 2.8. The example event picture shown in Figure 2.9 displays all the relevant features directly measured by the detector.

2.3 Upstream Veto

The upstream veto had the job of preventing triggering; the flash chambers could be triggered only **once** every fast extraction and thus it was imperative to reject triggering the system readout on the tail end of upstream showers or muons from either the decay of secondaries that escape the berm or upstream neutrino interactions. Ideally such a system would give a early signal with high efficiency for rejecting even low energy-loss muons. The veto wall also needed to cover a large area, the entire 3.7 m × 3.7 m front face of the calorimeter. The obvious choice of material for
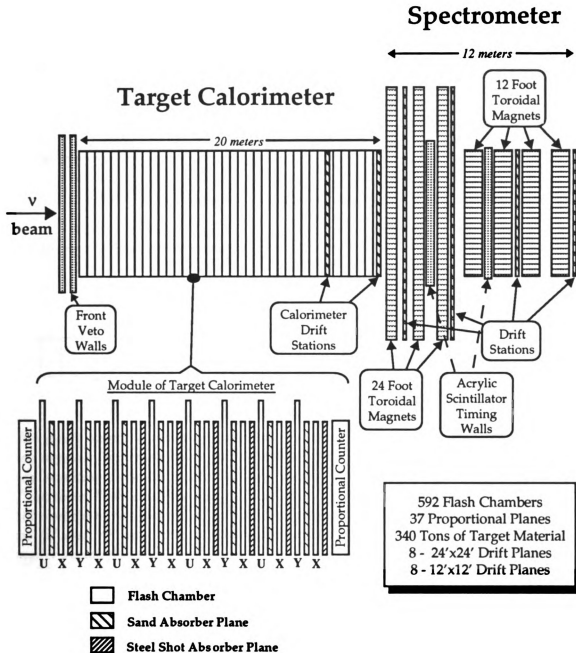
Figure 2.8: The E733 Neutrino Detector

A side view demonstrates the relative positions of the components that make up the E733 detector. [23]
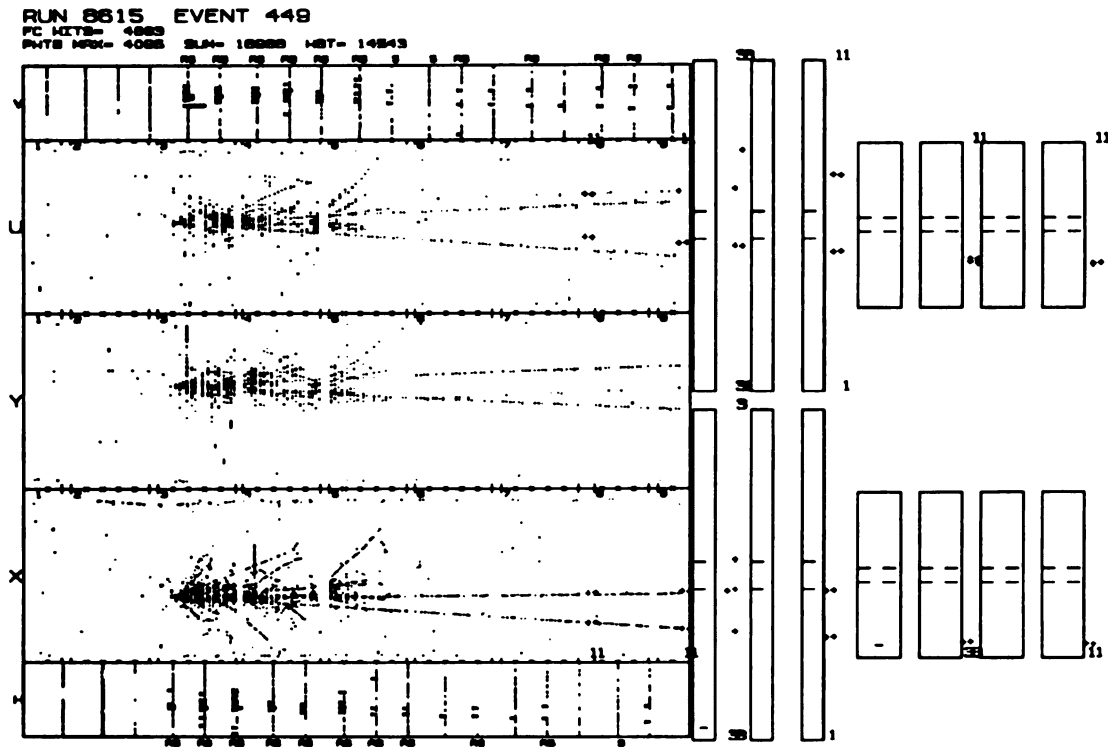
Figure 2.9: Standard event picture

This figure shows a representative dimuon event in the standard FMMF event display layout. Neutrinos enter from the left in this orientation; no incoming track is seen resulting from the neutrino. The display is dominated by the representations of the three flash chamber views. The lower (X) view corresponds to the chambers that contain horizontal tubes, and thus measure the vertical displacement. The upper two (U and Y) views give a pseudo-stereoscopic view, each 10° from vertical. The smaller rectangles above and below the flash chambers contain the information from the 37 proportional chambers. The signal from each chamber's 36 amplifiers is represented as a small histogram. On the right side of the figure, the two sets of seven rectangles are projections of the toroidal magnets that provide bending fields for the spectrometer. The small + markers represent hits in the drift planes. The calorimeter drift planes are located just before the first magnet and just upstream (left) of the bay 8 boundary. The spectrometer planes are located in the first, third and fifth gap and after the last magnet. Not shown are the liquid scintillator tanks and the WIMP counters. The veto wall would be at the extreme left and the STOP counters occupied the second and fourth gaps in the toroids.

RUN 9633 EVENT 68
FC HITS= 6140
PHTB MAX= 4096 SUM= 22269 HST= 21462
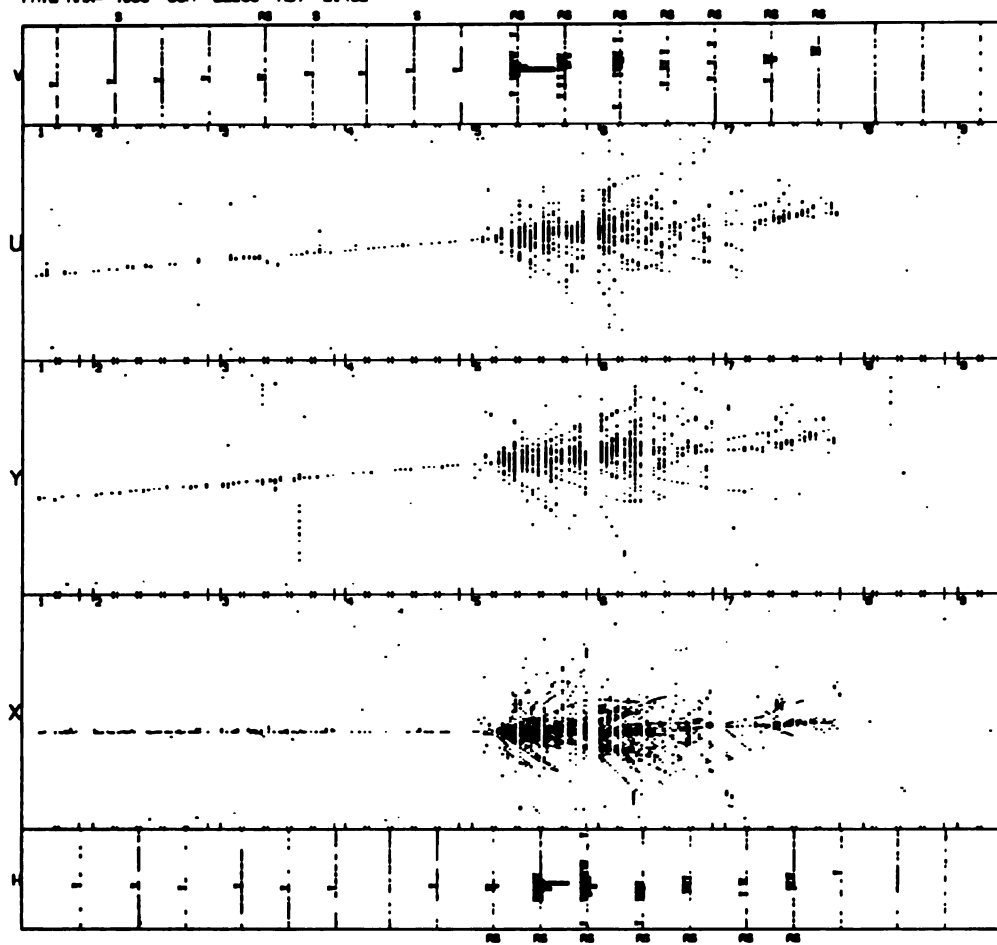
Figure 2.10: Example 150 GeV hadron test beam shower

constructing such a detector was scintillating-doped plastic. It gives a fast response, with high efficiency for detecting muons, and sheets can be combined to cover large areas at reasonable costs.

For the 1895 run such a veto wall was constructed of eight 4 ft by 8 ft sheets of 1 inch thick plastic. Along all edges of each of the sheets there was a light guide of wave shifter material. This absorbed photons of the energy produced by the scintillator doping (UV) and re-emitted blue photons that had the highest photomultiplier tube efficiency. Photomultiplier tubes (RCA 8575) were mounted at *each* corner of each sheet. The signals from the tubes were combined in coincidences and logical-ORs to give a signal with a 99.5% efficiency for detecting a muon without an excessive false signal rate.

In principle that was all that was necessary. But at the beginning of the 1985 run it was quickly recognized that the veto was "lit" up during each fast extraction and the generation of neutrinos. This effect was due to the production of many low energy thermal neutrons within the secondary beam area from the multiple interactions of primary and secondary high energy hadrons. The neutrons would then scatter off molecules of air and eventually many would result in *sky-shine*. Thermal neutrons have a high cross section for interaction with the many protons in the plastic resulting in an abnormally large energy deposition and signal rates. These neutrons were also slow and thus uncorrelated with any events or each other. This also played havoc with the STOP planes of similar construction in the spectrometer (refer to Section 2.5.2). The sky-shine had a less profound effect on the gaseous

detector elements and produced no more than a slight *haze* around the edges.

It was decided, due to the uncorrelated nature of the neutrons, to move the 1985 upstream veto back into the spectrometer. Used in coincidence with the existing STOP plane, the two independent indicators of an outgoing muon would result in a low random background while still maintaining high efficiency for a single true muon. This solved the dire problem of generating a drift TDC stop signal, but left the veto question unresolved. A reasonably efficient veto was constructed by increasing the voltage on the first two proportional planes and using the "or" of any signal from the first liquid scintillator tank or either of P4 or P5 SINGLES.

Prior to the 1987 data-taking run a new set of veto walls were constructed. Again, sheets of scintillator were used, though with only two photomultiplier tubes, positioned at opposite corners. Racks of 4 sheets hung off 4 overhead rails, on movable trolleys. This allow the racks to be configured as two walls each covering the front of the detector. This gave a 99.4% efficiency for detecting muons, again with low random background noise.

2.4   Calorimeter

The calorimeter was 19 meters long and had an active area of roughly 3.7 m × 3.7 m. The components of the calorimeter can be divided into two types: passive and active. The passive components constitute the majority of the target material from which the neutrinos scatter. This target material consisted mostly of silicon-dioxide

and iro

chamb

The

tally o

indepe

with t

"U" ch

cells w

the cell

reconst

chambe

At s

hierarch

beam:

module

⁴Modu

and iron. The active (or sensitive) components were used for triggering (proportional chambers) and measuring properties of the event (flash- and proportional chambers).

The proportional chambers consisted of aluminum planes of alternately horizontally or vertically oriented 1 inch square cells and provided both a trigger and an independent measure of shower energy. The flash chambers came in 3 orientations, with the 5 mm cells running horizontally ("X") or $\pm 10°$ from vertical ("Y" and "U" chambers respectively). Each chamber contained approximately 600 to 635 cells which gave a binary on-off response depending on whether the ionization in the cell exceeding threshold. Hit summing and pattern recognition allowed for the reconstruction of total shower energy, energy flow and muon tracking using this flash chamber information.

At this point it becomes necessary to introduce some jargon used to describe the hierarchical structure of the E733 detector.

beam: A beam formed the overall the fundamental grouping of flash chamber and target components; it consisted of 2 planes each of sand and steel shot, and 4 flash chambers (in a U-sand-X-steel-Y-sand-X-steel configuration).

module: Four beams and a proportional chamber formed a module. The proportional planes alternated in orientation, horizontal – vertical wires, module by module. There were 36 full modules and two partial modules for a total of 148 beams and 37 proportional planes[3].

---

[3]Modules 8-1 and 9-2 only contained two beams in order to provide room for the drift planes.

bay: The modules were further grouped into bays, with 2 to 5 modules per bay. Support structures and scintillators occupied the bay boundaries.

Also included in the calorimeter were 8 wire layers of drift planes in the form of four chambers. These could be used for muon tracking, but their importance lay in the critical role they played in alignment procedures and connecting the calorimeter to the spectrometer. The tanks of scintillating liquid and stations of plastic scintillator in the bay boundaries were not used in this analysis. These simply added to the passive target material.

2.4.1   Target Material

Most of the target material was made up of planes of lucite ($C_4H_8O_2$), filled alternately with sand (SiO_2) and steel (Fe) shot. These were interleaved between the the active components. The lucite planes are formed from 3 panels of extruded plastic 1.58 cm thick, 120 cm wide and 381 cm long. The lucite occupied 29% of the volume, giving the shot and sand filled planes an average density of 3.11 and 1.444 g/cm^3 respectively. These target planes constituted 90% of the mass of the detector.

2.4.2 Flash Chambers

Basic Principles

The purpose of the flash chamber was to provide muon tracking in the calorimeter and fine-grained sampling of hadronic showers. In all, there were 592 flash chambers each with over 600 cells; thus ~355,000 individually distinguishable channels filled a large volume at relatively low cost. Each chamber was constructed from three panels of corrugated polypropylene plastic. Panels were formed from extruded sheets of plastic composed of tubes running the length of the panel. The large flat surfaces were covered with foil electrodes and the cells were filled with spark-chamber gas. When a high voltage pulse was applied, an ionization track left by a particle traversing the chamber formed a plasma in the tube. By capacitively picking up the presence of the plasma individual "hits" could be recorded. Since the entire tube filled with the plasma it was impossible to distinguish where along the length of the tube the hit occurred. For that reason chambers were produced in three variant orientations:

X: cells ran horizontally, and thus measured vertical displacements.

U: cells were rotated from vertical by approximately 10°; displaced to the east at the top, and to the west at the bottom.

Y: cells were angled the opposite direction of U chambers, also rotated by 10°.

The two nearly vertical chambers allowed for a pseudo-stereoscopic view of the detector. This additional information permitted the track matching algorithms to discriminate against false pairing of hits in the orthogonal views.

General Construction

Panels approximately 4 feet (1.22 m) wide and 16 feet long were extrusion formed of rectangular tubes 5.8 mm wide and 5 mm thick. Each chamber was constructed from three panels attached with mylar tape. For the U and Y style chambers extra material was added to form an overall rectangular shape for structural and mounting purposes. Polypropylene gas manifolds were attached to the open ends of the panels and heat sealed to form a gas tight chamber. A tube running the length of the manifold, with 1 mm holes every 2 inches, evenly distributed the gas pressure.

The large flat surfaces were then covered by 5 mil (.13 mm) aluminum foil. The mylar tape holding the panels together acted as an insulator between the front and back electrodes at the joints. The foil was attached using a water based latex contact cement and the 3 ft wide strips overlapped by 3 inches. The overlaps and edges were then sealed with conductive aluminum tape to form a single conductive electrode. This was done to both the front and back surfaces. The approximate active area was 370 cm by 417 cm; the electrodes extended no closer than 12 inches from the ends of the tubes in order to prevent cross-talk. Tube-to-tube cross-talk occurred if the plasma could travel out of the tube into the manifold and back into nearby tubes.
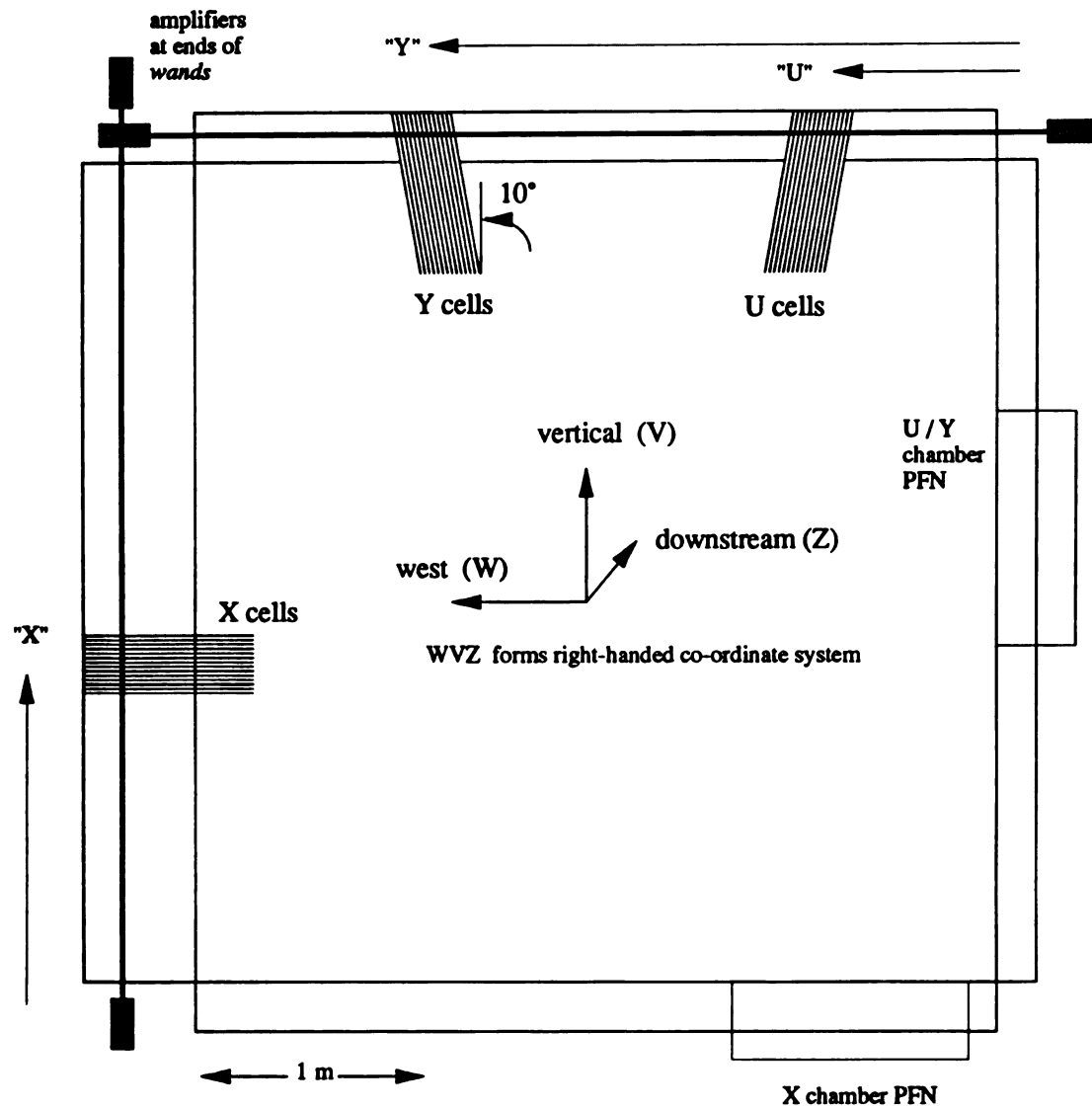
Figure 2.11: Orientation and Co-ordinate System of the Flash Chambers.
The relative sizes and orientations of the three variants of flash chambers are shown with representative sections of cells. Cell sizes are not to scale. The detector based (WVZ) co-ordinate system is superimposed.

Gas Recirculation

The chambers were filled with a mixture of 90% Neon, 10% Helium, ~0.125% Argon mixture. Maintaining gas purity was critical to proper flash chamber operation. Diffusion of the standard gasses out through the relatively thin (0.5 mm) walls of the chamber and atmospheric contaminants into the chamber necessitated that the gas flow provide approximately two complete volume changes per hour.

Collisions with the argon served to de-excite the long lived meta-stable Ne states. Atmospheric H_2O, O_2, N_2 are all electronegative gasses; which means that they tend to absorb free electrons. In large quantities they would remove the ionization necessary to initiate the plasma before the chamber could be fired, or prematurely quench the plasma. In trace quantities they helped control re-ignition, bringing the probability of a previously hit cell spontaneously re-firing down to 1–2% (when the chamber was pulsed at a 10 second repetition rate). To allow for this, approximately one-third the of recirculated gas was not purified. The remaining gas was cleaned and replenished by the gas carts.

Gas recirculation and purification was performed using a large distribution system of pipes and two gas carts. All the panels in a single beam were fed by the same manifold (called a pig) (see Figure 2.12). The pigs in turn were supplied from a large PVC pipe running from the gas cart. Each supply pig was accompanied by a flow-meter/regulator and the return pig had a shutoff valve. In case of a puncture only a single beam need be starved for gas until it could be tracked down and fixed.

The gas cart consisted of a two water-cooled heat exchangers, followed by a warm (room temperature) and a cold (liquid N_2) molecular sieve. These sieves absorbed the contaminants. On a regular schedule the gas flow was switched over to the other cart and the tainted sieves were heated and a vacuum pump removed the out-gassed contaminants. Check valves, pressure regulators and flow meters ensured that parameters were kept under control. Provisions were made to supply a continual flow of argon and pre-mixed He-Ne to make up for losses (diffusion and small leaks) in the system. In particular, most of the argon was removed by the cold sieve and had to be re-added just prior to re-circulating the gas to the chambers. The gas purity was checked once every shift (8–12 hours) by means of a gas chromatograph.

High Voltage

In order to form a plasma the charges in the ionization trail must be accelerated in a large electric field to create a cascade. This field is generated by applying a high voltage pulse to the "hot" electrode while keeping the other at ground potential. Such a pulse is generated by an arrangement of capacitors, inductors and resistors called a pulse-forming-network (PFN) as show in Figure 2.13. This is attached to the chamber by an edge connector formed of spring-metal contacts; the electrodes on the chambers extend out on to a tongue from which the PFN was hung. On X style chambers these tongues were located on the bottom near the East corner; on U and Y chambers these were half way up the East side. Alternating the placement
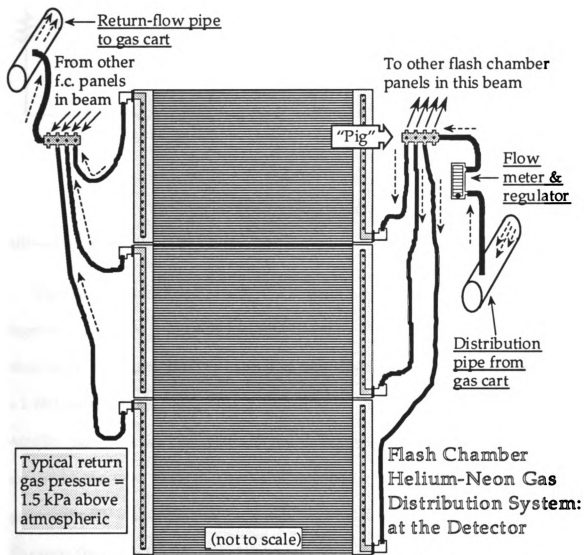
Figure 2.12: Flash Chamber Gas Distribution System

Flash Chamber HV System: the Pulse-Forming Network
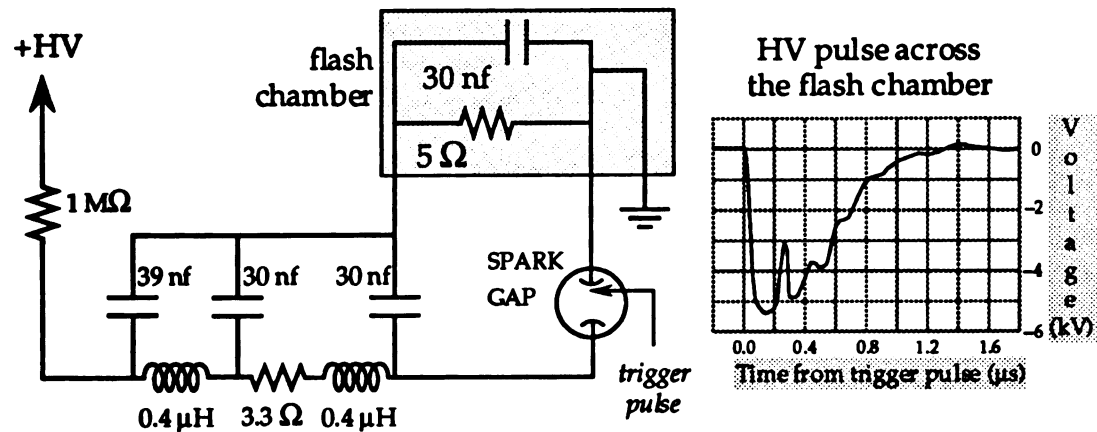
Figure 2.13: Flash Chamber HV Pulse Forming Network

allowed for sufficient space between PFNs.

The chamber itself acted as a 30 nF capacitor and the electrodes were connected together via two 10 Ω resistors opposite the PFN. These played an integral part of shaping the HV pulse. The PFN capacitors were slowly charged up to 8500 V through a 1 MΩ resistor. This voltage was generated by two centrally located Hipotronic HV supplies (one each for the upstream and downstream halves of the detector) and carried to the PFNs through a series of distribution panels. During the charging process the HV side of the PFN capacitors were isolated from all but the HV supply. To create the pulse, the hot side of these capacitors were electrically connected to the "hot" electrode. This was accomplished quickly and simultaneously for 592 chambers by means of spark gaps.

Every PFN contained a lucite cylinder with aluminum caps; one cap electrically connected to the capacitors, the other to the chamber. One end also held a marine

spark plug (Champion L-20V), which when fired formed a electrical connection to the electrode-bolt in the other. The gap was supplied with dry N_2 gas to avoid fire hazards and delay the oxidation of contaminants. The sparks were in turn initiated by the output of one of the 8 thyratron pulsers. These devices supply a short duration 2.5 kV HV pulse with a very short rise time and a very stable trigger-to-trigger consistency. The rise time for the spark pulse was of order 10–15 ns, with very little jitter. The thyratrons were slaved to the externally generated overall event trigger (Section 2.6). The electrode-bolt in the spark gap was adjusted until the distance between it and the spark plug was just greater than the critical breakdown distance. This "tuning" ensured that the spread in breakdown times was less than 15 ns.

Figure 2.13 also show the typical shape of the resultant HV pulse from a PFN as measured on the chamber. The fast rise time (50–60 ns) was an important feature; if the rise is too slow or the voltage too low, the field would act to sweep away the ionization trail rather than form a plasma. The typical measured peak voltage was of order 5 to 5.5 kV, and the pulse duration was 450–600 ns. The long duration ensured that once a plasma was generated at some location in a tube, it re-generated more plasma nearby until the entire tube was filled. The plasma transit time was roughly 150 ns. The pulse is large enough that it could be evenly distributed over the chamber with no adverse affects, such as drooping, when many cells are active.

Safety, always a concern, was important for a detector composed of flammable plastic with sparks and high voltages in close proximity. An errant random break-down in a spark gap was always apparent from the tattle-tale snap sound and the

62

accompanying bright flash. Such gaps, once tracked down, were re-tuned. Other precautions included limits on the current draw of the Hipotronic HV supplies. A 4.5 second window starting at trigger time allowed for full current draw during the PFN recharge phase. The supplies would trip if greater than 1 mA was drawn outside the window. Such trips brought down all the flash chamber HV supplies and required a manual reset. This limit was sufficient to handle the occasional aberrant discharge, but sympathetic discharges of multiple chambers crashed the system. A bypass was supplied for tracking down problem conditions by allowing a ~5 mA draw. This mode required human intervention: one person was required to constantly hold down a push button, while another could investigate the problem. Crash buttons at regular intervals along the detector would instantly trip the HV supplies when depressed. A key system prevented the HV from being activated when work was being done on the detector: the removal of a key disabled the HV system.

Chamber Readout

At this stage all that has happened is that cells hit by ionizing particles are filled with a neon plasma. Early proto-types of this type of detector played with the idea of taking edge-on photographs of the cells, like a large series of neon light bulbs. This method has obvious attendant drawbacks: the need for mirrors and other optics; film handling and processing; events must be re-digitized for processing with modern computers. On the other hand, individually instrumenting each cell with some kind of electronic pickup would have been prohibitively expensive. The solution to these

constraints was quite clever in turning a large parallel problem into a smaller serially oriented one.

In the readout region of each chamber the ground electrode was lifted away from the plane by a spacer and a series of photo-etched copper strips ("fingers") were placed against the polypropylene. A strip was aligned with each cell. These strips, formed from copper-cladding over mylar, were 508 mm long and 3 mm wide. At the outside edge they narrowed to a thin wire before joining a common ground bus. Each strip acted as one plate of a 3 pF capacitor; when the intervening dielectric changed from He-Ne gas to a plasma, a current flow of ~500 mA travelled through the wire to the ground bus. The geometry involved is illustrated in Figure 2.14.

Cells that were not struck also had a small pick up from the HV pulse, but approximately five fold smaller. This was further reduced by the addition of a 2 inch aluminum bucking strip that extended the length of the detector perpendicular to the pickup fingers. This strip was isolated from the copper by two 10 mil (.25 mm) mylar spacers. A one-to-one inverting transformer connected to the "hot" electrode, in conjunction with appropriately chosen resistors, induced a HV pulse of opposite polarity to the pickup near the sense wire. This served to cancel the pickup in the unhit cells, without severly affecting the true signals. With the bucking in place the signal to noise ratio was greater than 10:1.

The key was to turn the problem of over 600 potential parallel signals (per chamber) into a smaller serial problem that could be handled by 1978–era technology (when this part of the detector was built). One should note that a changing current

From Hot Plane

R_1

Bucking
Strip

Bucking
Transformer

Copper Pickup Strips
3 mm × 508 mm

Top View

Polypropylene

Ground Bus

Magnetostrictive
Wire

R_2

Side View

Magnetostrictive Wand

Bucking Strip

10 mils Mylar

Polypropylene Spacer

Ground Bus

Ground Plane

508 mm

Hot Plane

M.S. Wire

Photoetched Mylar
(pickup region)

Polypropylene of Chamber
(Cells run left to right)

Gas Manifold

Figure 2.14: Details of Flash Chamber Readout System

flow in the copper wires is accompanied by a changing magnetic field. There just happens to be such objects as Remendur-27 magnetostrictive (m.s.) wires. These 5 × 12 mil (.13 mm × .30 mm) wires respond to a magnetic field pulse by a local contraction and relaxation. This local phenomena forms a longitudinal acoustic pulse that launches, at the speed of sound (5000 m/s), both directions down the m.s. wire. This material's speed of sound corresponds to separating adjacent hit cells by roughly 1 μsec and neatly spreads the original signals out into packets that can be easily handled by even slow electronics.

The m.s. wire was held in place by a 10 mil deep groove in an aluminum bar (the "wand") and isolated from the wand by a tube of teflon tape. The ends of the m.s. wire were anchored by compressing the wire between the flat head of a screw and an aluminum plate. The anchor, along with a flag of mylar tape, minimized reflections. A steady trickle of dry N_2 gas into the teflon tube deterred corrosion of the m.s. wire. Periodic degaussing and remagnetization of the m.s. wire ("zapping") was performed by running a current through a loosely wrapped solenoidal coil that ran the length of the wand, surrounding the rectangular cross section. Proper magnetization limited attenuation of the acoustic pulse by minimizing the dispersion. During the 1987 run each wand was zapped between accelerator cycles.

The problem was thus reduced to a series of acoustical pulses arriving at the ends of the wires separated by a minimum of 1 μsec intervals. At this stage the electrical current-to-mechanical motion trick was reversed to give a series of electrical signals. Tiny teflon sleeves wrapped with 50 turns of hair-fine 44-gauge copper wire were

mounted around the m.s. wire, 2 inches from each end. The copper coil's placement along the wire was adjusted to maximize the signal quality as the inductor moved in the field of a small magnet. The acoustic pulse jiggled the coil in the dipole field changing the magnetic flux crossing the loop and thus creating an induced *emf* in the coil. These tiny signals were immediately amplified by a pre-amp mounted to the wand end; this produced a signal gain of ~1000 while a small ferrite toroid choke provided for noise suppression.

The amplified signal (roughly 0.5 V) was then sent to the digitizing crates. These contained cards for discriminating the signals and recording them in local memories. There were approximately 20% losses in the signal between hits near the pickup coil and those at the center. To compensate for such attenuation the discriminator threshold exponentially decreased as hits arrived. The overall level and decay constant were adjusted for each pre-amp (592 × 2). Figure 2.15 demonstrates the digitization process.

A master clock signaled each card to record the current discriminator output in a 1024 by 1-bit memory chip. The length-to-clock conversion was 2.4037 mm per clock count (cc). Since cells were roughly 5.75 mm wide this corresponded to 2.4 clock counts, easily ensuring that adjacent cells could be distinguished. Furthermore, the data buffering system inhibited, in hardware, two adjacent memory locations from recording an ON state. A flash-noise suppression system prevented the system from recording the spurious pickup generated by the large *emf* induced by 592 PFNs simultaneously discharging. Three small wires positioned at the ends and center of
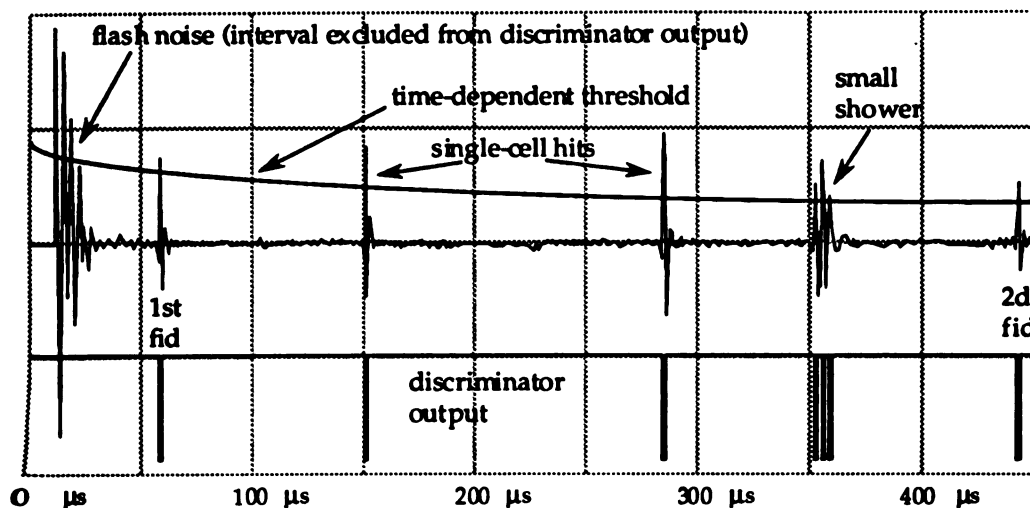
Figure 2.15: Flash Chamber Pre-Amp Output

the active region provided fixed reference points (*fiducial marks*) by always registering a "hit". Only the first 366 cells, slightly over half the chamber, were kept from each wand end. This provided sufficient overlap without having to worry about the large signal degradation of signals from the far end of the wand. Upon completion of the digitization phase, the memory boards were asynchronously read out alternately into one of two 4096 × 16-bit memory buffers. These buffers contained reformatted information, recording only buffer size information, identifiers to hit wands and the clock counts of actual hits (10 bits). These buffers were read as part of the CAMAC data acquisition system tied to the PDP-11/45 computer.

2.4.3 Proportional Chambers

Proportional chambers give a response directly *proportional* to the ionization energy loss within the chamber. These chambers output a continuous signal and thus can

be used for triggering purposes. The first two planes in the calorimeter were used as veto planes during the 1985 data taking run; they were run at a higher voltage and events were required to have little activity in them in order to be accepted. Each plane consisted of 144 cells of extruded Aluminum (8 cells per extrusion). The cells were 1 inch in cross section and 12 feet long; each cell was strung with a single 50 micron diameter Gold-plated Tungsten anode wire under 180 grams of tension. The cells were filled with P10 gas, an Argon-Methane (CH_4) 90%–10% mixture, giving a fast drift time ($\leq$ 200 nsec at 1650 V) for electrons to reach the wire. A calibration background of 21.7 KeV photons was supplied, at a low rate, by radioactive Cd^{109} sources ($0.4\mu C$) mounted outside each tube. The photons interact via the photoelectric effect and deposit the equivalent energy to that left by 3 to 4 minimum ionizing particles.

The extrusions were maintained at ground potential, while a positive high voltage (HV) of 1575 V (1750 V for veto planes) was supplied to the groups of 4 adjacent wires via current limiting 15 MΩ resistors. On the other end of the wires the outputs of a gang of 4 wires were each capacitively coupled to a single amplifier (Figure 2.16). There were 36 charge sensitive amplifiers per plane, 4 per amplifier printed circuit (PC) board. During the run approximately 1 to 2% of the amplifier channels did not work and .4% of all wires were disconnected due to HV short circuits.
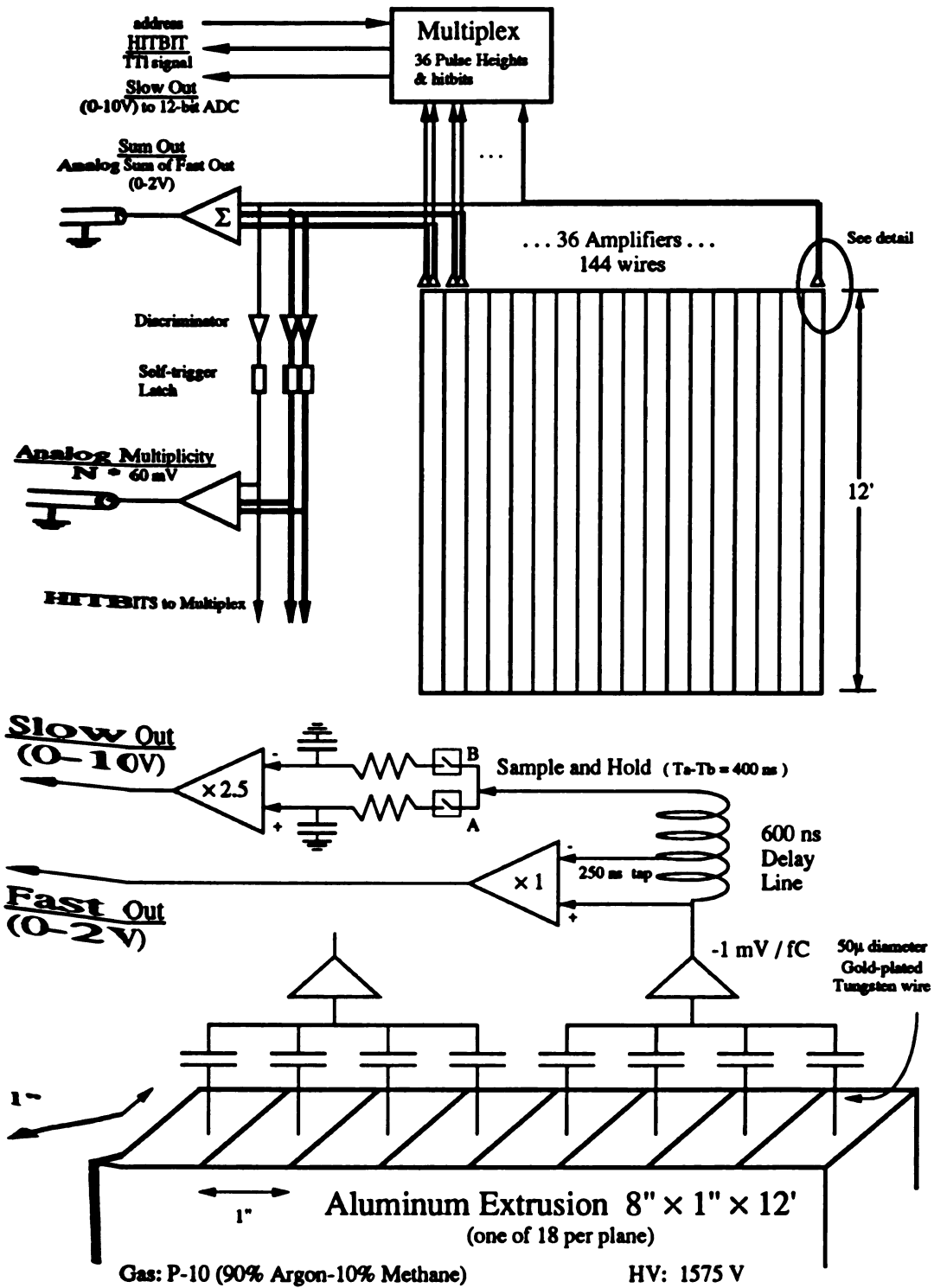
Figure 2.16: Proportional Chamber Readout Schematics

Analog Signals

Each amplifier circuit generated 2 distinct signals: FASTOUT and SLOWOUT. The intial preamplifier generated a signal approximately 1 mV per femto-Coulomb of charge collected. This output was directed into a 600 ns delay line. This delay allows trigger information to be generated and processed before the information disappeared. Two track-and-hold circuits followed the delay line output; each consisted of an analog switch and resistor/capacitor network. The voltage across the capacitor thus reflected to delay line output while the analog switch was closed and held its current voltage when the switch was opened. The *before* track-and-hold circuit switch was opened by a trigger signal before any true signal could exit the 600 ns delay line, and thus sampled the baseline output of the amplifier. The *after* signal was held 400 ns later. The difference of the two signals, amplified by 2.5, constituted the SLOWOUT signal. The stored SLOWOUT signals from each amplifier were directed to an analog multiplexer on the plane. The multiplexed signals from the planes were sent to an 12 bit ADC. These ADC values are the basis for the proportional tube energy calculations.

Taps into the 600 ns delay line at 0 and 250 ns constituted the positive and negative inputs to a unity gain amplifier. The output of this amplifier ranged from 0 to 2 V, and was denoted as the FASTOUT signal. FASTOUT signals were further processed on the plane to produce other signals used in triggering. FASTOUT signals were not individually extracted from the plane.

The SUMOUT signal for each plane was generated as an analog sum of the 36 FASTOUT signals. This total pulse height for the plane was carried by equal timed cables to a central location where each was subjected to processing to produce two further signals. One signal was amplified by a factor of 2 for enhanced sensitivity to single muons, while the second signal was an attenuation by a factor of ten to allow sampling the full range without saturation. Both signals were then digitized by a LeCroy 4301 Fast Encode and Readout ADC. These 11-bit values were transferred to a LeCroy 4302 buffer memory and later read out into the computer. The SUMOUTs were also analog summed to form the SUMSUM ($\Sigma\Sigma$) signal. The $\Sigma\Sigma$ was discriminated at a variety of levels to form components of different triggers.

Latches

Some of the other relevant signals generated from the proportional planes were:

HITBIT   The HITBIT signals for each channel were generated by discriminating (on the plane) the FASTOUT signals at a low threshold. The HITBIT had a 90% efficiency for registering a single normally-incident muon. Each TTL level HITBIT was latched when a trigger was sent to the plane, and they were recorded along with the SLOWOUT signals during the read-out phase. On the standard event display each HITBIT is marked with a > to the left of that channel's zero point.

AM   An analog sum of the HITBITS, 60 mV per ON bit, formed the "Analog

Multiplicity" (AM) signal. The AM signals were sent, via equal timed cables,

to a central location to be further processed to generate various triggers. On

the event display the presence of non-zero signal is signified by a "A" along

side the display for that chamber.

SINGLE The SINGLEs signal was the logical OR of the 36 HITBITs for the plane. This

signal was also sent back to to the central trigger location. On the event

display these are denoted with a "S".

2.4.4 Calorimeter Drift Planes

In the calorimeter there were 4 physical planes (2 wires layers per plane) resulting in

two drift corrected measurements (Section 4.4.2) in each view, horizontal and verti-

cal, of a muon separated from the shower and exiting the back of the calorimeter.

Planes with wires in the vertical orientation were placed at z positions 1653 and

1932 cm, horizontal planes at 1664 and 1943 cm. For cleanly resolved back-to-back

hits with drift information the transverse resolution was approximately 1.25 mm,

giving a slope error of order 1 mrad in each view. Hit inefficiency and the high

probability of noise, such as from associated delta rays, drastically reduced the fre-

quency of getting such a clean measurement. These combinatorics along with the

requirement of the muon separate from the shower before the first drift plane reduced

the importance of the drift planes for tracking neutrino induced muons. In general,

the slope and position measurements from the highly sampled flash chambers were simply superior. The calorimeter drift chambers real relevance lay in their usefulness in determining the alignment of the flash chambers and as a means of tying the calorimeter and spectrometer together. This connection was accomplished using straight through beam and cosmic ray muons.

The construction of the drift planes used in the calorimeter was identical to those in the spectrometer; for a complete description of their physical parameters and readout refer to Sections 2.5.3 and 2.5.4. The only substantial difference from those in the spectrometer was the addition of aluminum covers over the HV supply network and readout cards as shielding against the EM pulse generated during the readout phase of the flash chambers.

2.4.5 Liquid Scintillators and WIMP Counters

Tanks of liquid scintillator occupied the space between the nine bays (for a total of 8 tanks), approximately every 5 modules (80 flash chambers). The liquid scintillator tanks are each viewed by several photomultiplier tubes; the outputs were linearly added using a resistor network and simply discriminated resulting in a mere on/off indication of activity. They were slow, inefficient and unsuitable for any use other than simple low bias triggering on cosmic rays.

The so-called "WIMP" counters (which only existed for the 1987 run) occupied the space following bays 2 through 5, replacing the liquid scintillation tanks. Each

station consisted of 4 sheets of high speed scintillator 2 m by 30 cm by 2 cm hung horizontally, with the flat face incidental to the neutrino beam. Light guide fans collected the light for the photomultiplier tube and base attached at each end. Pulse height and timing information was measured for each tube. This data, in conjunction with measurements of the accelerator clock cycle, give the effective time of flight (TOF) of the interacting particle. For neutrino events, that TOF should be consistent with the speed of light; the existence of events outside the range defined by the speed of light and the time spread of the extracted beam would be indicative of a "Weakly Interacting Massive Particle" (WIMP). The analysis of the data from these counters can be found in a PhD thesis by Elizabeth Gallas [24].

2.5 Muon Spectrometer System

2.5.1 Magnets

The magnets used in this experiment were inherited from an earlier experiment which used the same building[25]. There were seven magnets in total, three were 24 feet in diameter followed by four that were 12 ft in diameter. Both sizes were constructed of flame cut iron slabs welded together to form an overall toroid shape. The 12 ft magnets consisted of 6 annular disks for an average total thickness of 49.5 inches with a center hole 1 ft in diameter. Twelve water-cooled copper coils of 7 turns were evenly spaced around the annulus, passing through the center hole and slightly
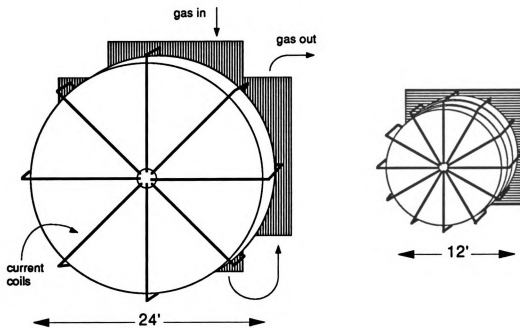
Figure 2.17: Toroidal magnets and their respective drift planes.

beyond the external radius. The 24 ft magnets were formed from 3 pancakes and had an average 26 inch thickness and a 2 ft diameter hole. These were wrapped with only 8 coils but each coil consisted of more turns.

A nominally 800A DC current passed through the coils to produce a magnetic field in the ϕ direction. Figure 2.18 demonstrates the slow variation of field strength as a function of radius. The details of how the magnetic field was used to determine muon momentum can be found in Section 4.4.2. The holes of the magnets were filled with bags of lead shot in order to absorb hadrons. This prevented an event deep in the detector from "blasting" through all the spectrometer drift planes unstopped.
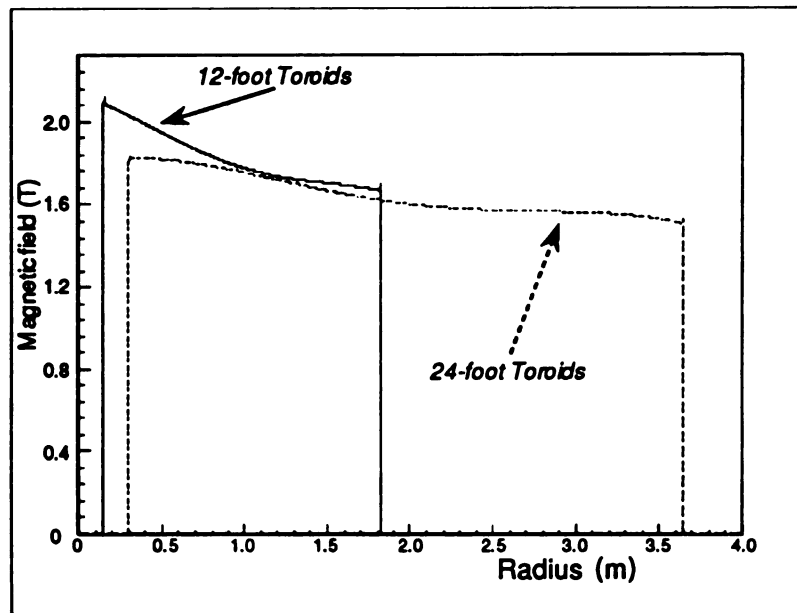
Figure 2.18: Toroid Magnetic Field Strength as a Function of Radius.

These are fitted functions to measurements (using a Hall probe) at numerous points in the magnets. No attempt was made to account for small local deviations due to irregularities in the magnet construction. Also no attempt was made to approximate the fringe fields outside of the iron.

2.5.2 Timing Planes

The timing planes were large scale scintillator walls which signaled the passage of a muon into the spectrometer system. The were constructed using techniques similar to those of the Upstream Veto (refer to Section 2.3). Each wall of consisted of two physical planes. The larger wall was constructed from four sheets of 5 ft×8 ft plastic scintillators in each plane, and was located between the second and third 24 ft magnets. This plane provided at total 16 ft × 16 ft coverage. Each piece of 1 inch thick acrylic sheet was supported by a UniStrut^{tm} framework and the physical planes were made light-tight by enclosing them between sheets of heavy black polyurethane plastic. The second wall was located between the first and second 12 ft magnets. This was constructed of 4 ft×8 ft slabs and enclosed in aluminum boxes, 4 sheets to a box. These boxes, when properly arranged, completely covered a 12 ft × 12 ft area. All four physical planes hung from rolling trolleys attached to horizontal I-beams. This allowed adjustments in the transverse placement of the planes and access for maintenance when they were rolled out of the confined space between magnets.

As with the Upstream Veto, the scintillator light was absorbed, re-radiated and redirected by bars of wave-shifter plastic. The signals were generated by RCA 8575 photomultiplier tubes with transistor controlled bases. Analog signals were sent to a central location via equal length cables. By discriminating and stretching the signals a coincidence could be formed by requiring a hit somewhere in each wall. This coincidence reduced the spurious signals produced by the sky-shine described in Section 2.3. This coincidence signal was labelled STOP and was required for optimal

operation of the drift chambers. It provided a excellent reference time relative to the passage of the muon. When such a signal was unavailable[4] the STOP signal was generated from a delayed version of the original trigger signal. The extra delay was enough to allow a real signal to be seen and to distinguish it from a timing plane generated STOP. The STOP signal generated by the trigger was unreliable for use with the drift system because of the large jitter in time depending on event size and placement in the calorimeter. In order to truly be useful the signal needed a jitter of less than 20 ns relative to the true traversal time; this was not realized by the trigger due to inescapable limitations in the proportional chambers. Large showers produced systematically faster triggers than small showers.

2.5.3   Drift Plane Construction & Operation

Drift chambers operate by applying a HV to a wire which produces an electric field between it and the surrounding grounded material. This in turn causes any liberated electrons to "drift" towards the wire until they are close enough to form an avalanche cascade. This drift velocity is sensitive to the gas mixture and field configuration. By measuring the time it takes for the earliest electrons to drift in one can infer the closest approach of the particle. For the chambers used in this experiment the drift time-to-distance relationship is relatively linear with a kink corresponding to the corner regions. The time resolution of the digitization process resulted in an

---

[4]It was possible, even with the large coverage area, for the muon to miss one or both of the walls. Each wall had a better than 99% efficiency for registering a hit when a muon actually passed through it, so only a 2% inefficiency arose from requiring a coincidence.
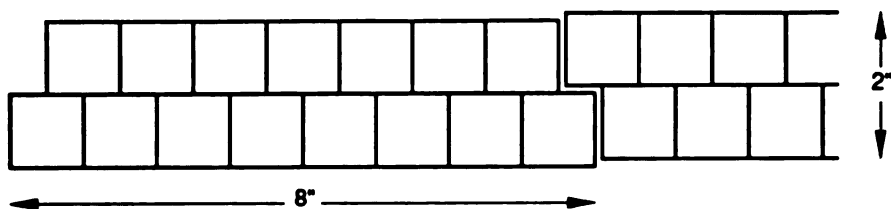
Figure 2.19: End view of aluminum extrusions used to construct the drift planes.

approximately 2 mm spatial resolution.

The drift chambers were constructed from aluminum extrusions. The extrusion had two staggered layers of square (1 inch× 1 inch, nominal) cells, seven cells in one layer, eight in the other. Chambers were constructed by interleaving extrusions to form a large two layer plane (Figure 2.19). A total of 8 (physical) chambers formed the spectrometer measuring stations that occupied the gaps following 4 of the magnets. In each gap a chamber of horizontal wires was followed by one of vertically oriented wires. Those behind the second and fourth 12 ft magnets (like those in the calorimeter) measured 12 ft square. Those immediately downstream of the first and third 24 ft magnets were 24 ft square with notches taken out of the corners. The notches removed sections that would have extended well outward of the projected "shadow" of the magnets.

The cells were strung with a single 50 μm gold-plated tungsten wire under tension ($\approx$ 200 g). The wire was held by a brass tube centered in a nylon bolt epoxied to the extrusion. Current limiting 10 MΩ resistors connects the wires to the HV supply bus. The 12 ft planes were kept at an operating voltage of 1900 V, and the 24 ft wires at 1850 V. The long 24 ft wires were subject to sag and this necessitated the

lower operating voltage. Sagging wires were susceptible to a behavior known as "wire oscillations". The wires would be attracted to the cell wall due to their own electrostatic image. As the wire approached the wall it would discharge and recoil, only to repeat the process.

An E-10 gas mixture of 90% Argon and 10% Ethane was introduced to the cells. A constant back pressure ($\sim$ 10 p.s.i.) was generated by oil filled bubblers on the output. The 12 ft planes received 1 cubic foot per hour, while the 24 ft ran at twice that rate. These were adjusted using flowmeters on the input lines. The gas was not recirculated and was simply exhausted outside the building. The ethane content is sufficiently low that no fire hazard existed.

2.5.4   Drift Electronics and Readout

The HV wires were connected to logically distinct circuits that measured the drift time. The interface cards were connected back to a central drift readout controller that interrogated the interface cards and wrote the non-zero values into a buffer memory available to the data acquisition system.

Each wire was attached to an pulse shaping amplifier/discriminator circuit which feed a TDC (time-to-digital converter). The discriminator included an adjustable threshold. The efficiency for registering a hit in at least one wire layer was approximately 92% for the 12 ft chambers and 88% for the 24 ft chambers[26]. Operating in *common stop* mode, the digital counter on a particular wire initiated counting upon
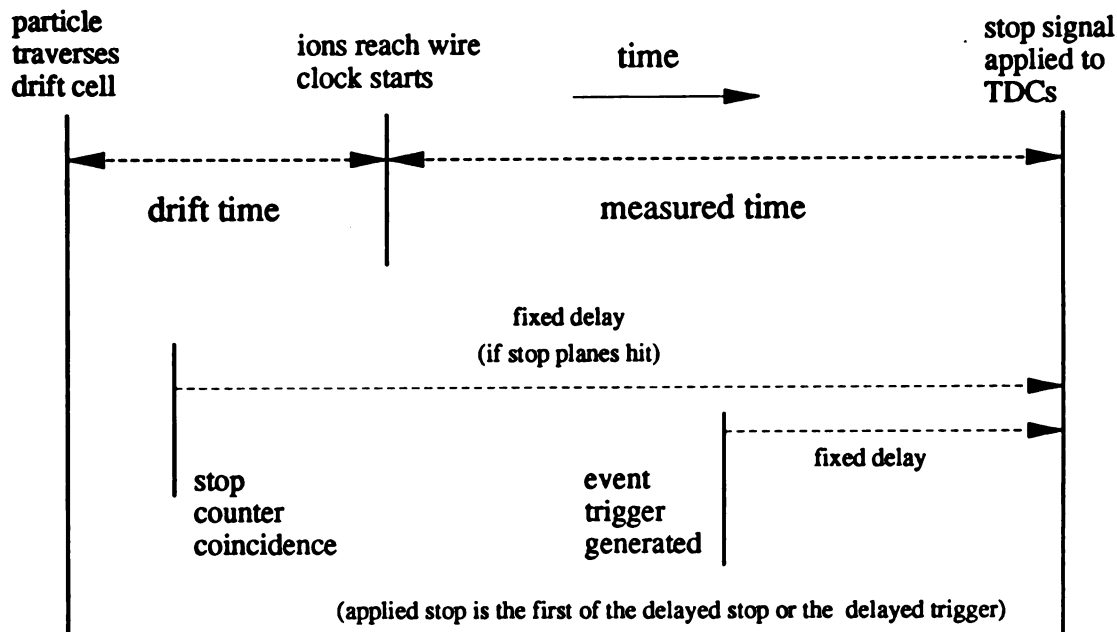
Figure 2.20: Temporal relationship between events involving the drift chambers.

first registering a hit. Counting ceased upon receiving a delayed signal from either the STOP counters or a much delayed trigger signal. The actual drift time was then determined by subtracting the counting time from the known delay (Figure 2.20). Differences in the delay due to different cable lengths could be accounted for by looking at the count ranges registered in each channel .

The counters were capable of 6-bit values (0 to 63). Upon wrap-around they reset and stopped counting. Thus to clear the counters after readout all the non-zero counters were restarted and allowed to count until they reset. The TDCs were locked into a common 50 MHz clock, so each count represented 20 ns. Each TDC card serviced 16 wires and was divided into two separate sections (A/B) for the multiplicity signal. Hit channels contributed a current to that section's AM signal. These signals were summed in an analog fashion on the interface board.

For readout (and AM) purposes all physical chambers were divided into logical (readout) chambers of a single layer consisting of 144 wires. Thus a 12 ft chamber had two logical chambers and a 24 ft had four. Due to the slightly odd construction of the 24 ft chambers not all potential channels had a wire with which to connect. This sequencing mis-match was unfolded in the data unpacking software during event reconstruction. Each interface card provided:

- Address decoding and data multiplexing for reading out the 16 TDC cards.

- Fanout for the 50 MHz clock and RUN/$\overline{\text{HOLD}}$ signals to the TDC cards. The RUN/$\overline{\text{HOLD}}$ signal derived from STOP signal. A "hold" was signaled by the the STOP and cleared by the completion of the readout.

- Analog Multiplicity AM summing for the 18 sections. These were available as co-axial cable signals in three forms: an analog signal (60 mV per hit) and discriminated at the one and two hit levels sent as NIM signals.

The original drift readout system began interrogating the interface cards in a serial fashion immediately following the flash noise suppression delay. This serial processing was relatively slow and took approximately 127 msec to complete. Each channel was accessed by the master drift controller. The chambers were addressed with an outer loop over the 32 (including the calorimeter drift planes) interface cards and an inner one over the 144 possible wires. The controller wrote all the non-zero values, along with their identifying address, into a Lecroy 4299 4k × 16-bit memory buffer. The buffer was subsequently readout via the CAMAC databus system.

Fast Drift Readout Electronics

For the 1987 data taking run, additional electronics were built to allow the acquisition of sub-events beyond the event associated with the flash chamber trigger. By placing memories out on the planes, the TDC values could be stored in parallel in local memories. This reduced the deadtime to only that necessary in reading out 16 values into the 2k × 8-bit memories servicing each TDC card (8 μsec) plus the time to reset the TDCs (1.3μsec)[5]. A pair of printed circuit cards replaced the original interface card. The actual memory chips were located on one board which worked in conjunction with an analog-&-address card that performed the address decoding and handled the AM signals.

The original drift readout controller was replaced by a series of modules that not only read out the memories but allowed for advanced diagnostics. During readout, TDC values and their addresses (and sub-event number) were stored in a 16k × 16-bit LeCroy 4302 memory unit. This was the same type of CAMAC buffer used to store the Fast ADC values from the proportional chambers. The time to store a complete sub-event was ~10 msec.

Provisions were made for writing patterns *out* to the memories on the planes and then reading them back in. This performed a check on the data path up to the TDC card connection. Data read back was checked against a suppression pattern before being written to the LeCroy memory. The value was stored only if the two

---

[5]Contrast this 9.3μsec deadtime to the roughly 10 msec neutrino spill.

NIM signals

PDP 11/45 online
data aquisition
system

NIM/CAMAC input
multiplexing and
latching

intelligent address
generator

enable trigger
enable scan
enable write
reset
latch pattern
latch event #

CAMAC
command decoder

(17) ECL

CAMAC databus

LeCroy 4302
buffer memory

NIM

(17) ECL

scanner
test pattern generator

trigger control &
pattern writer

flash trigger
noflash trigger
clock event #
busy

50 MHz clock
stop signal
AM > 0
AM > 1
analog multiplicity (AM)

} (NIM)

timeout checking &
visual monitor display

(50) TTL bus

Analog and Address
interface board
(1 per logical plane)
(8 per fanout module)

(20 + 13)
differential current

fanout module
(1 of 4)

(30) TTL
(2) ECL
(18) analog

TDC board 0

TDC board 1

TDC local buffer
memory board
(1 per A&A board)

(10) TTL
(1) ECL clock
(2) analog

TDC board 8

Figure 2.21: Data path of fast readout of the drift system.

did not match. A variety of patterns were possible: static patterns and ones derived from various subsections of the plane/channel address. In normal systems operation suppression of an all-zero pattern was performed. The scanner could also be operated in single step mode to allow operation independent of the CAMAC system. A visual display using LEDs was provided.

Due to difficulty in producing a trigger for the alternative sub-events the system was never fully used to its potential.

2.6 Trigger

Triggers are necessary for initiating the acquisition of data. Each trigger defined a unique event. Much of the logic used in creating a trigger was performed using fast devices housed in modular units connected by coaxial cables. Careful attention was payed to delays introduced by the cables. The signals were generally pulses using the NIM standard where logic '0' is ground and logic '1' is -16 mA into a 50 Ω terminator.

The event triggers used a pre-trigger signal (PTwait) as a starting point. This was generated from information output by the free-running proportional chambers in the following steps:

AM   Analog signal from each prop plane, 60 mV for each of the 36 channels

            with the HITBIT on. (See Section 2.4.3 for a description of HITBIT signals)

AM′   A simple resistive division of signal size to 90% of the original; the other 10% was available for routine monitoring on an oscilloscope. These were checked once every shift.

$AM'_{>1c}$ NIM level signal resulting from the discrimination of AM′ from the plane at approximately 77–97 mV. Thus the signal was on if *more* than one channel was above threshold.

$AM'_{>1c,>2p}$ This NIM signal was the coincidence of 3 or more $AM'_{>1c}$ signals.

PTwait   This was the basic component of all the non-pulser triggers; it was simply the $AM'_{>1c,>2p}$ signal stretched and delayed. The delay allowed for other slower components to arrive before requiring a coincidence.

The minimum-bias neutrino trigger was formed logically equivalent to

$$\text{PTwait} \cdot \text{DBG gate} \cdot \overline{\text{VETO}} \cdot (\Sigma\Sigma > 19\text{mV})$$

Beyond the pre-trigger, it simply required the event to occur during the neutrino spill; there be no activity in the Upstream Veto counters; and a minimal amount of energy deposited in the calorimeter. This energy requirement is enforced via the low level discrimination of the sum of proportional chamber SUMOUT signals. The minimum-bias trigger was fully efficient for showers energies greater than 10 GeV. Other neutrino triggers involved either higher $\Sigma\Sigma$ levels or some additional information from the spectrometer timing planes or drift chambers. These triggers were not used in this analysis unless they occurred in conjunction with the minimum bias

trigger. If no trigger was taken by the conclusion of the DBG, then a *no-event pulser trigger* was generated. This ensured that the CAMAC system was read out so that locally generated beamline monitor information was recorded.

2.7   Data Recording, Formatting and Processing

Once a trigger was taken various beamline monitors, assorted latches and scalers, ADC memories (including proportional tube information), flash chamber and drift buffer memories, and such, all contained important information. The process of recording this information started by reading the various devices interfaced to the CAMAC databus system. Crates contained a controller and up to 23 CAMAC devices. The crate supplied power to the 23 stations via an edge-card backplane. Command information, decoded address information (LOOK-AT-ME), and 24 bits each of read and write TTL signal lines were available. Up to seven crates were connected via a databus branch highway cable of 66 wire-pairs. A branch driver connected the highway to the DEC PDP-11/45 running the RSX-11 operating system.

Data acquisition at was handled by a program called MULTI. This program performed the actual reading of the CAMAC buffers and writing the data to 9-track tape reels. Diagnostic information was available online, as was limited data preview capabilities. Sanity checks on the incoming data were performed in order to provide early warning about equipment failures.

Offline the 1600-bps tapes were reformatted onto 6250-bps reel tapes. The data

was also blocked into records of 512 60-bit words. Some preliminary pre-processing was done: notably, the elimination of overlap hits from the central flash chamber region (Section 2.4.2) and the collection of statistics for the removal of the fiducial mark pseudo-hits.

The reformatted data used a block structure impressed on a sequential record format. Logical records were disjoint from the 512×60-bit physical records. The logical records started with a header identifying it as either an *Event* or one of many auxiliary records (e.g. *Begin Run, End Run, Monitor*). Within a record, any number of sub-records (or "blocks") could be imbedded with unique identifiers (Figure 2.22). Blocks could be added or deleted at any time. A framework dealing with the data in a consistent manner was adopted for the experiment. Every data processing program consisted of a call to **ANA** (for *analysis*), which handled the reading and writing of the input and output streams, unpacking the logical block into a central buffer (**/DATBUF/IDAT()**) and calling the appropriate user entry points. Users supplied routines enumerating actions for the following cases:

init   This routine was called before *any* processing was done.

newidvn   The format and details of some of the data structures were modified between runs; these changes were labelled as version numbers. This routine allowed version dependent setup procedures to be called. Normally a file or tape would only contain data of one version so this would be called immediately following **init**, after some data had been read but before
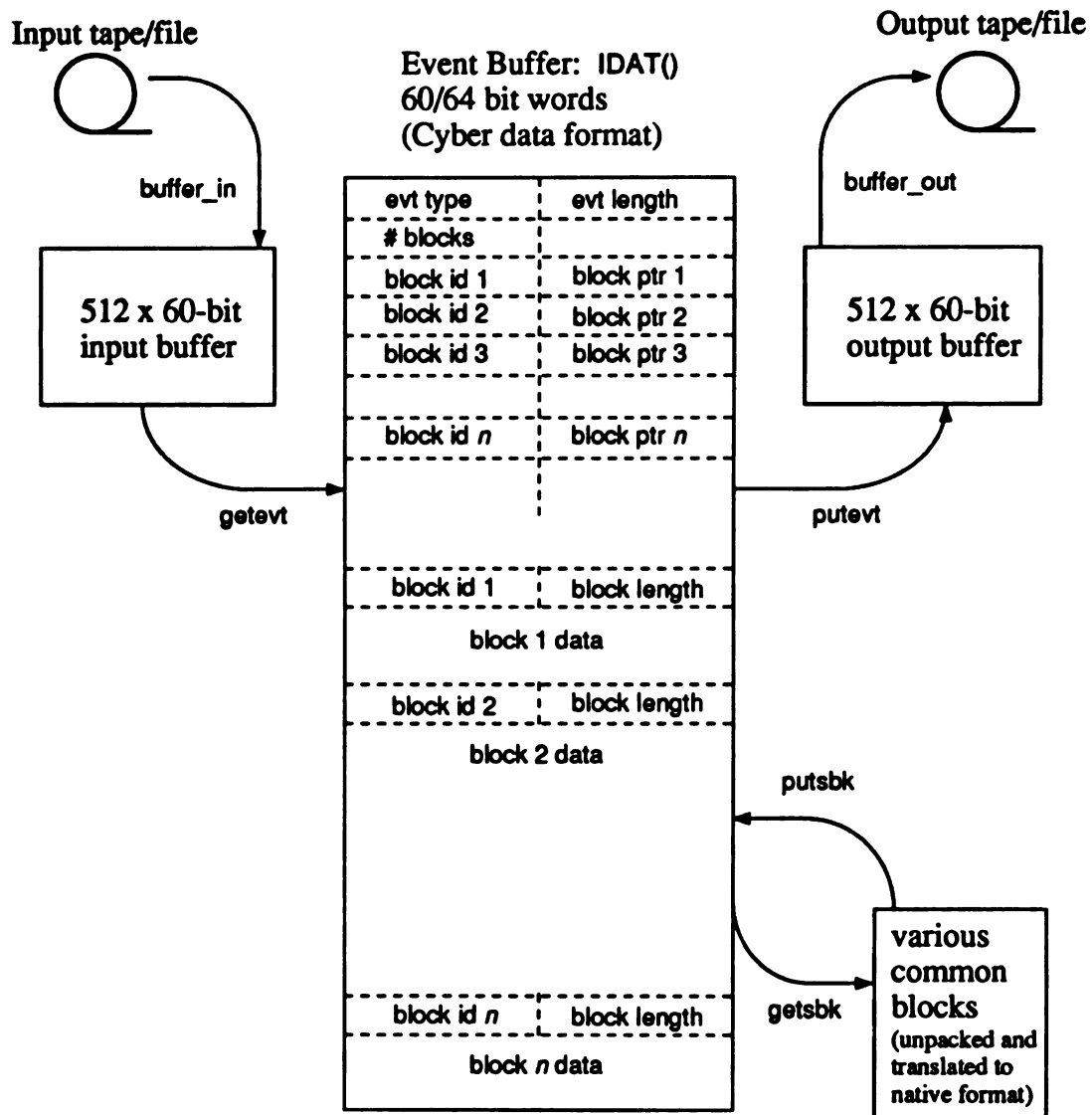
Figure 2.22: Organization of Reformatted Data

Input and output data streams took the form of sequential records blocked at 3840 bytes (512 60-bit words). Logical records (events and ancillary blocks) are of arbitrary length, but an integral number of 60-bit words in length. The routines putsbk *and* getsbk *performed the translation to and from the Cyber format to native VAX format.*

calling either **event** or **notev**.

event All event processing was done in this routine (or routines called by it). The details of this processing are elaborated on in Chapter 3.6.

notev(id) Logical records that were not events were loaded into the central buffer and this routine was called with an integer record-type identifier.

finish This routine was called after *all* processing was complete.

Due to the untimely demise of the Fermilab Cyber system (decommissioned September 1990) an effort was made to ensure access to the data on alternative platforms. Due to availability (and the lack of truly viable alternative choices) the collaboration settled on porting the entire analysis to the VAX VMS system. A large amount of effort was spent[6]. It was decided infeasible to re-write all the data tapes, as both too expensive in 9-track tapes and tape handling resources. Instead provisions were made for reading the 60-bit words and re-buffering them in memory. Sub-blocks ordinarily corresponded to a simple copy of the the information in the associated Cyber common block. On the VAX the data retained the Cyber format and each sub-block had an associated "layout" descriptor to allow conversion from Cyber to VAX formats. The output data stream (usually with information added) was reconverted to the Cyber format to allow interchange during the transition period. The layout descriptors indicating which variables corresponded to floating point, integer, and hollerith datum.

---

[6]The author alone spent over 9 months, essentially full time, converting and testing the code on the new platform.

Chapter 3

Monte Carlo Event Simulations

A table of random numbers, once printed, needs no errata

– Mark Kale

3.1 Overview

Computer simulations using the Monte Carlo (MC) method are a powerful tool for experiment analysis[27]. They provide a representation of what the experiment should see with a given model of the underlying physics. They also are critical in determining the effects of acceptance and resolution due to the particular apparatus used. In this experiment the important subcomponents of the simulation are:

- *the Neutrino Beam simulation:* models the energy, type and position of neutrinos expected to enter the detector.

- *the Neutrino Interaction model:* represents the kinematics of neutrinos scattering off the nucleons. This encapsulates the key physics under investigation.

91

- *the Quark Fragmentation model:* handles the non-perturbative, soft process of turning the high energy out-going quark into physical hadrons.

- *the Hadron Decay simulation:* generates secondary muons. This includes the interesting charm hadron decays and the background from pion and kaon decay.

- *the Detector simulation:* accounts for the effects of a real-world detector on the basic products of the scattering, fragmentation and decay. This may include some subsequent physics such as energy loss and multiple scattering of particles traveling through matter and bending in a magnetic field. These are thought to be well understood, albeit complex, phenomena.

3.2   Beam Files

The neutrino beam flux is the end-product of the the characterization of all that happens upstream of the detector. This information originates by assuming a parameterization of the production of secondaries resulting from 800 GeV protons striking the beryllium oxide target. This production spectrum generated by Malensek[28] is derived from a measurement by Atherton, *et al.* [29] scaled up from 400 GeV to 800 GeV. These distributions of energies and directions of the various secondaries were fed as input to a beam line simulation[30] of the QT train which proceeds to model their transport and decay. The program simulates the magnetic optics properties of the beam line including dipoles, quadrupoles and collimator elements. As the pion or kaon is propagated through the optics a process of random decay is simulated

based on known lifetimes. The kinematics of these decays determine the trajectory and energies of the neutrinos of interest. The neutrino is then straight line translated to the position of the front of the FMMF detector. The small angular divergence of the beam has a negligible effect on the radius over the length of the detector. These positions are recorded in a scatter plot of E_ν vs radius for each parent type ($\pi^\pm, K^\pm$ or K_L^0) and decay mode. These scatter plots are then sampled in appropriate relative ratios to produce a *beam file* consisting of a list of neutrinos and their corresponding information (radial position, energy, parentage and decay type).

3.3   4-Vector Generator

The software framework for the entire simulation of the physics and FMMF detector is referred to as the VLIB package. Extensions were written to allow this to be used in conjunction with the GEANT and LUND MC packages.

3.3.1   Hard Scattering Interaction

The aim of this part of the code is to simulate the coupling of the neutrino to the virtual boson, and the scattering of said-same boson off the quarks in the nucleon. The boson-neutrino coupling is straight forward and unambiguous, but the boson-nucleon coupling is not. For the most part, we employed a leading-order (LO) cross section (Eq. 1.15) that only involves quarks; in this case the coupling is similar to

the boson-neutrino and the only other necessary assumption is the distribution of quarks in the nucleon as parameterized in the Parton Distribution Functions (PDF). No Fermi motion of the nucleon within the nucleus was modelled. This defect in the modelling can be shown to account from some of the discrepancy between the simulation and measurement seen at high energy[23]. Some studies were performed to investigate the Next-to-Leading-Order (NLO) cross section of Tung, *et al.*[31][1]. More details of this cross section can be found in Section B.2.

For the case of the LO cross section, which is formulated under the condition of massless quarks, the slow rescaling prescription was used to handle the non-negligible charm quark mass. This is described in Section 1.4. The NLO cross sections are built up from the helicity formalism and include all the effects of quark masses to the order of the perturbation expansion.

Operationally this step in the simulation is performed by a modified rejection method MC. It starts by choosing a target nucleon and a neutrino from the beam file. Then the invariants x and y chosen by an importance sampling method. From these the differential cross section is calculated using a particular PDF as described in Section 3.3.2. Based on the weights and the calculated cross section the event is either accepted or rejected. If rejected no further processing is done and a new event is generated. If the event is accepted, then the 4-vectors representing the final state kinematics of the muon and the hadron system are calculated.

A correction must be made to the cross section to account for the radiative box

---

[1]The code generously by provided by private arrangement with the authors.

diagram[32, 33, 34, 35]. An additional correction must be made for the possibility of a radiative emission of a (nearly) collinear photon by the the muon which then contributes to the measured hadronic energy and lowers the measured energy of the outgoing muon (Section B.1).

3.3.2 Parton Distributions

The distribution of partons (quarks and gluons) in the nucleon is a field of intensive research. Several collections and global analysis of the world's current data exist, notably Harriman, *et al.*[36], Morfin and Tung[37] and the CTEQ collaboration[21]. Neutrino scattering as a probe of these distributions is one method of constraining these and the FMMF collaboration is in the process of publishing the related structure functions: F_2 and F_3[23].

In this analysis we have primarily relied on the HMRS-B distribution in order to make the comparisons to other measurements. Comparisons using alternative PDFs were made to show the sensitivity to this input.

3.3.3 Fragmentation Functions

Fragmentation is the process by which a quark jet is converted into the physically realized system of hadrons. This soft process is currently not calculable using perturbative QCD. Various phenomenologically based models have been proposed to explain how this occurs. It is presumed, and experimental data indicates, that the

fragmentation of heavy quarks is characteristically different then that of light quarks.

Charm fragmentation

The charm quark can fragment into a variety of hadrons. This analysis modelled the branching modes that make up the most probable possibilities: the $\Lambda_c = [udc]$ baryon, and the mesons $D^0 = [c\bar{u}]$, $D^+ = [c\bar{d}]$, $D_s^+ = [c\bar{s}]$, and their excited brethren the D^{*0}, D^{*+}, D_s^{*+}.

The MC was thrown with a branching fraction to Λ_c fixed at 10%, and in the final analysis reweighted to 7.6%. The D_s^+ production was suppressed in a manner similar to that used by the LUND MC, so that the relative rates $D^0 : D^+ : D_s^+$ were $1 : 1 : 0.5$. From spin statistics $D : D^*$ was fixed at $1 : 3$.

The kinematics of the fragmentation of a charm quark into hadrons was modelled using the Peterson[38] parameterization:

$$D(z) \sim \frac{1}{z\left(1 - \frac{1}{z} - \frac{\epsilon}{1-z}\right)^2}$$

where $z_E = E^{hadron}/E^{quark}$. This leaves one free parameter, ϵ, to be adjusted to match the data. Under this model ϵ is related to m_q^2/m_Q^2 with m_Q being the effective heavy quark mass and m_q being light quark mass that combines with it.

The literature is strewn with instances of z_E and $z_P = p^{hadron}/p^{quark}$ used in an
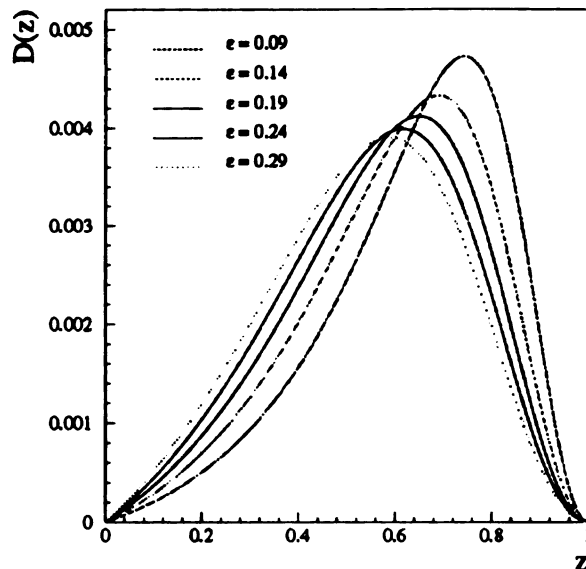
Figure 3.1: Peterson Fragmentation Function

Curves normalized $\int_0^1 D(z) = 1$. Shown for different values of ϵ: .09 (highest peak), .14, .19 (nominal value), .24, .29 (lowest peak)

almost interchangeable fashion. Both are approximations to the light cone variable:

$$z = \frac{(E + p_{||})_{had}}{(E + p)_{quark}}$$

where all three become equivalent in the scaling limit. This choice of z_E places an intrinsic threshold on z due to the restriction $W > (m_p + m_D + m_\pi)$, where W is the invariant mass of the hadronic system. Ultimately this leads to minimum z in the distribution at $z_{min} = m_D/W_{max}$.

The alternative z_p would purports to take on the full range $[0, 1]$ but at the cost having to worry about strict energy conservation at large values of z_p. The problem arises from the inability to split a 4-vector $(E = \sqrt{p_Q^2 + m_Q^2}, 0, 0, p_Q)$ into two 4-vectors $(E = \sqrt{p_D^2 + m_D^2}, 0, 0, p_D)$ and $(E', 0, 0, p')$ in a covariant fashion using

Table 3.1: Peterson Fragmentation Parameterization ϵ

Reference	data	def	energy scale	ϵ		
Kleinknecht[40]	e^+e^-, νN	z_E	various	.11	$\pm$	.04
ARGUS[39]	e^+e^-	z_p	10 GeV	.19	$\pm$	.03
CLEO[40]	e^+e^-	z_p	10 GeV	.156	$\pm$	.015
FNAL E531[41, 42, 43]	νN	z_E	small GeV	.076	$\pm$	.014
same (by CCFRW) [16]	νN	z_p	$W^2 > 30\mathrm{GeV}^2$	.18	$\pm$	.06
CCFRW[16]	νN	z_p	$\sqrt{\langle W^2 \rangle} \simeq 16\mathrm{GeV}$	.22	$\pm$	.05

either definition as a single scaling variable. This manifests itself as an intrinsic limitation of this model of jet fragmentation; namely it encounters difficulties near the production threshold.

The parameter ϵ is measured by the ARGUS collaboration using e^+e^- data[39] to be $\epsilon = .19 \pm .03$ using the z_p scheme. This data was taken at a center of mass energy of 10 GeV at the DORIS II storage ring which is close to $\langle W \rangle \simeq 13$ GeV. The e^+e^- measurement by CLEO[40] gives $\epsilon = .156 \pm .015$. The neutrino emulsion FNAL E531 data[41, 42, 43] reports a value of $\epsilon = .076 \pm .014$, but at a significantly lower $\langle W \rangle$. This data reanalyzed[16] for $W^2 > 30$ GeV^2 yields $\epsilon = .18 \pm .06$. Earlier measurements by others[44] resulted in an average $\epsilon = .11 \pm .04$. The newest estimate from the neutrino experiment CCFRW[16] is $\epsilon = .22 \pm .05$.

This uncertainty in the key parameter, and even in the definition of the scaling variable itself, gives impetus to the assignment of a large uncertainty to ϵ used in the simulation and the investigation of the effect of varying it over a wide range.

The possibility of acquiring a transverse momentum (relative to the c-quark direction) was also included. This has been parameterized numerous different ways

in the literature. Lacking any real guidance or motivation to choose a particular functional form, we have chosen to implement it using the most common form:

$$\frac{dN}{dp_t^2} = \frac{1}{2\beta}e^{-\beta p_t^2} \qquad \text{with } \beta = 1.1$$

Lund

The fragmentation of light quark jets is a much softer spectrum in the scaling variable z. Various models and parameterizations exist to characterize this process. We have chosen to use the popular LUND code that implements a string model. The combination of JETSET 6.3 and LEPTO 4.3[45, 46, 47] were used in two distinct modes in modelling this part of the physics. In both cases the code is primarily used to fragment a struck-spectator quark system into combinations of the hadrons realized in nature. For the studies of pion and kaon decays that contribute to the background, LEPTO was used both as a 4-vector generator (replacing the VLIB generator) and to carry out the entire hadronization of the struck quark and spectator diquark system. In that case the neutrino flux was supplied externally to the package, but the cross section and PDFs were simply the present internal routines. In the case of the one and two muon simulation of the physics, LUND was used only to fragment the non-charm component of the final state hadron system.

The LUND model of fragmentation is based on the picture of a colour flux tube stretched between a quark-antiquark or quark-diquark pair. The stored energy per unit length of tube is assumed to be a constant. The dynamics of jet fragmentation

are then modelled by giving a probability that the tube will break into two pieces as the pair move apart; the newly created endpoints correspond to a quark-antiquark pair pulled out of the vacuum. All the details of requiring a colour singlet meson or colourless baryon are then taken care of by the program. The process is iterative until each intact flux tube is energetically unable to split and only stable particles remain. There is a cost associated with the split in the case of the heavier quarks. The suppression of $u : d : s : c$ is on the order of $1 : 1 : 0.3 : 10^{-11}$. This ratio can be loosely justified if $\kappa = \frac{2S}{U+D}$ is considered to be the relative availability of strange quarks from the sea in the nucleon. Baryon production can also occur by pulling a pair of diquarks from the vacuum, but this is suppressed on the order of $q : qq \simeq 1 : 0.065$ for nonstrange diquarks. The end result is a list of 4-vectors representing mesons and baryons.

The entire LUND model has been tuned, by the program authors, to phenomenologically match a number of earlier experiments that measured individual particles and energies under a variety of processes.

3.3.4 Charm Hadron Decays

The prompt second muons of interest come from the decay of charmed hadrons. The LUND MC facilitated the simulation of the decay of the small number of Λ_c baryons produced ($< 10\%$ of the charm hadrons). This produced a mostly negligible contribution to the prompt signal since the branching ratio $\Lambda_c \to \mu\nu X$ is also small,

Table 3.2: Charm Baryon Semileptonic Branching Ratio

Branching Mode		PDG value [6]		Thrown	Final
$\Lambda_c^+ \rightarrow$	$e^+ \nu_e$ + anything	4.5%	$\pm 1.7\%$	-	
	$[s, du0]\ \mu^+ \nu_\mu$	-		4.5%	4.5%

Table 3.3: D* Meson Branching Ratios

Branching Mode	PDG value [6]		Thrown	Final
$D^{*0} \rightarrow\ D^0 \pi^0$	55%	$\pm\ 6\%$	51.5%	51.5%
$D^0 \gamma$	45%	$\pm\ 6\%$	48.5%	48.5%
$D^{*+} \rightarrow\ D^0 \pi^+$	55%	$\pm\ 4\%$	49%	55%
$D^+ \pi^0$	27.2%	$\pm 2.6\%$	34%	30%
$D^+ \gamma$	18%	$\pm\ 4\%$	17%	15%
$D_s^{*+} \rightarrow\ D_s^+ \gamma$	dominant		100%	100%

approximately 4.5%. Thus the Λ_c contributes no more than 5% of the total prompt muon signal. Modelling the decay kinematics of the three-body decays of D mesons correctly was of more import.

The kinematics of D meson decay were based on studies done by the Mark III collaboration[48]. The pseudoscalar D can semileptonically decay to either another pseudoscalar meson, a vector meson, or a non-resonant system of two pseudoscalar mesons (in either a P or S wave state). The branching fractions as previously measured by other groups and as used in this analysis are shown in Tables 3.3, 3.4.

Unfortunately the branching fractions are *not* well known for the decays into muons and that ignorance is reflected in the missing entries or large errors. It is important to note that even for the measured subprocesses involving muons that are measured there is disagreement with the equivalent electron subprocess. This can arise from

Table 3.4: D Semileptonic Branching Ratios

Branching Mode		PDG value [6]		Thrown	Final
$D^0 \to$ $e^+ \nu_e$	+ anything	7.7%	$\pm 1.2\%$	-	
$\mu^+ \nu_\mu$	+ anything	8.8%	$\pm 2.5\%$	-	8.8%
$K^- \pi^0 e^+ \nu_e$		1.6%	$^{+1.3}_{-0.5}\%$	-	
$\overline{K^0} \pi^- e^+ \nu_e$		2.8%	$^{+1.7}_{-0.9}\%$	-	
$K^{*-} e^+ \nu_e$		1.7%	$\pm 0.6\%$	3%	
$K^- e^+ \nu_e$		3.3%	$\pm 0.3\%$	4%	
$K \pi \mu^+ \nu_\mu$		-		1%	1.408%
$K^{*-} \mu^+ \nu_\mu$		-		3%	1.848%
$K^- \mu^+ \nu_\mu$		2.9%	$\pm 0.5\%$	4%	5.016%
$\pi^- \mu^+ \nu_\mu$		0.39%	$^{+0.23}_{-0.12}\%$	1%	0.528%
$\rho^- \mu^+ \nu_\mu$		-		1%	0.0%
$D^+ \to$ $e^+ \nu_e$	+ anything	17.2%	$\pm 1.9\%$	-	
$\mu^+ \nu_\mu$	+ anything	-		-	18.92%
$K^- \pi^+ e^+ \nu_e$		3.8%	$^{+0.9}_{-0.7}\%$	1%	
$\overline{K^{*0}} e^+ \nu_e$		4.1%	$\pm 0.6\%$	8%	
$\overline{K^0} e^+ \nu_e$		5.5%	$^{+1.2}_{-1.1}\%$	8%	
$\rho^0 e^+ \nu_e$		<0.37%		2%	
$K \pi \mu^+ \nu_\mu$		-		1%	3.028%
$\overline{K^{*0}} \mu^+ \nu_\mu$		-		8%	3.973%
$\overline{K^0} \mu^+ \nu_\mu$		7.0%	$^{+3.0}_{-2.0}\%$	8%	10.784%
$\pi^0 \mu^+ \nu_\mu$		-		1%	1.135%
$\rho^0 \mu^+ \nu_\mu$		-		2%	0.0%
$D_s^+ \to$ $e^+ \nu_e$	+ anything	< 20%		-	
$\{\phi, K^*, \eta, \omega, \eta', f^0\} + e^+ \nu_e$		1.6%	$\pm 0.7\%$	-	
$\{\phi, K^*, \eta, \omega, \eta', f^0\} + l^+ \nu_e$		1.4%	$\pm 0.5\%$	-	1.4%
$K \pi \mu^+ \nu_\mu$		-		1%	0.224%
$\phi^0 \mu^+ \nu_\mu$		-		3%	0.294%
$\eta \mu^+ \nu_\mu$		-		3%	0.798%
$\eta' \mu^+ \nu_\mu$		-		1%	0.084%
$\omega \mu^+ \nu_\mu$		-		1%	0.0%

three causes. Two causes that are not important here are that the discrepancy is due to either experimental systematic errors in the measurements or simple statistics. The third component is the inherent difference due to the factor of 200 difference in masses between the two leptons. In the Coffman formulation of the matrix element form factor the term related to the 4-vector difference of the D and resultant hadron state can not be ignored for the muon case.

The columns in Tables 3.2, 3.3, 3.4 labelled *thrown* and *final* refer to the branching fraction when the MC was generated and the final relative weights (Section 3.5). From the given numbers we can estimate the overall branching fraction of charmed quarks into muons by multiplying out all the subprocess fractions. In the fitting procedure Br_c (this overall branching fraction) was allowed to float while keeping the same relative sub-rates. Using the chosen values the adjusted total branching fraction is 9.303%. Explicitly, the possible decay paths are:

$$
\begin{aligned}
Br(c \to \mu) = \ & Br(c \to \Lambda_c) \cdot Br(\Lambda_c \to \mu) + \\
& Br(c \to D^{*0}) \cdot Br(D^{*0} \to D^0) \cdot Br(D^0 \to \mu) + \\
& Br(c \to D^{*+}) \cdot Br(D^{*+} \to D^0) \cdot Br(D^0 \to \mu) + \\
& Br(c \to D^{*+}) \cdot Br(D^{*+} \to D^+) \cdot Br(D^+ \to \mu) + \\
& Br(c \to D_s^{*+}) \cdot Br(D_s^{*+} \to D_s^+) \cdot Br(D_s^+ \to \mu) + \\
& Br(c \to D^0) \cdot Br(D^0 \to \mu) + \\
& Br(c \to D^+) \cdot Br(D^+ \to \mu) + \\
& Br(c \to D_s^+) \cdot Br(D_s^+ \to \mu)
\end{aligned}
\tag{3.1}
$$

3.4 Detector Simulation

The last step in the simulation sequence is that of modelling the detector response. This step starts with a list of particles and their energies, momenta and positions. The outcome should be a representation of what the actual detector would measure given such an event. A detector simulation might take the approach of completely modelling the transport of the particles through volumes of matter taking into account their interactions and the active elements individual response functions. Alternatively, the simulation could just represent the average gross overall response based on measured average features of the detector. In this study we have chosen to take take both routes, performing detailed simulations when computationally feasible or necessary for an accurate representation of the data and using a smearing method to facilitate the rest. In particular the simulation of the muon spectrometer system was entirely based on a system of modelling the details of the system. Much of the same code was used to generate the muons hits in simulations was also used to reconstruct the muon momenta of both the data and MC. This reduced the number of biases introduced into the critical muon information.

3.4.1 Hadron Shower Simulation

For the most part the MC modelled the detector effects on the hadron shower by smearing the true value by the experimentally measured resolution. The energy as "measured" in the flash chambers and the prop-tubes were individually smeared

and then combined using the same algorithm as the data. This gives an adequate portrayal for the dimuon data. For detailed studies of the shower development GEANT was used to model the technicalities of the exact sensitivities of the calorimeter.

Geant

The generic detector simulation package GEANT[49] developed at CERN is a system of detector description and simulation tools that help carry out a detailed simulation. There are frameworks for managing the many minutia that are involved with such a task. Different functions include defining materials occupying volumes of space; defining particles, their decay properties and their interaction properties with materials; a system of specifying the geometry and makeup of the simulated detector; a means of manipulating and tracking the list of particles being transported through the model; detailed simulations of a variety of physics processes; a bookkeeping framework for energy losses in active detector elements and another framework for chronicling the digitized representation of these energy losses.

Many of the physics processes involving particle interactions with bulk matter are simulated by GEANT. Hadronic interactions are handled by the GHEISHA[50] package from within GEANT. A list of the possible reactions is given in Table 3.5.

In this experiment GEANT was used in two different modes. For part of the background decay studies (and the hadron shower shape studies) GEANT was used to fully represent all the sub-elements that constitute the calorimeter. This meant

Table 3.5: Physics processes dealt with by GEANT.

Process	Photon	Electron	Muon	Hadrons
e^+e^- pair conversion	●			
Compton collisions	●			
photoelectric effect	●			
photo-fission of high Z	●			
positron annihilation		●		
multiple scattering		●	●	●
ionization		●	●	●
delta ray production		●	●	●
Bremsstrahlung		●	●	
decay in flight			●	●
nuclear interactions			●	
direct e^+e^- pair production			●	
hadronic interactions				●

specifying the geometry down to the smallest flash chamber cell; running in this mode was very computationally expensive and thus very slow. This attention to the subtleties makes it possible to create events that have the exact same structure as real events coming from the data acquisition system. In turn these MC events can then be processed through exactly the same software as real events and are thus subject to the same subtle biases that depend on an individual event's geometry that might otherwise be glossed over in a MC that relies on average resolutions.

In order to get statistically meaningful results the GEANT representation of the calorimeter could be simplified to that of a homogeneous, isotropic block of average material. In this mode the 4-vectors and positions of the muons (and missed neutrinos) were recorded as hadrons propagated through the soup and decayed. At the

conclusion of tracking all particles to their stopping point or where they exit the calorimeter, the non-leptonic part of the shower was then smeared according to the measured resolutions.

3.4.2 Muon Simulation

The handling of the muon simulation neatly subdivides into two components along the same lines as the detector. The calorimeter and the spectrometer have very different characteristics and are handled separately. In both cases VLIB transports a muon in small steps in z, accounting for energy losses and multiple scattering; and, in the case of the spectrometer, the bending of a charged particle in a magnetic field.

The energy loss per unit length traversed depends both on the muon energy and the particular bulk material penetrated. Energy losses less than 1 MeV are treated as a continuous process using the Bethe-Bloch formula[6] which accounts for the statistical average of a profusion of tiny individual losses. Above 1 MeV knock-on electrons (δ rays)[6], nuclear bremsstrahlung, pair productions, and nuclear interactions[51] are accounted for as discrete processes. Delta ray production accounts for the dominant portion of the low energy discrete losses. The effect of the these discrete losses is to create an asymmetric tail to the energy loss spectrum. This non-Gaussian distribution gives rise to a non-trivial muon momentum resolution not easily dealt with using a parameterization (smearing) method. Hence the need for a more detailed simulation.

Operationally this part of the simulation proceeds in the following manner. A step length is calculated using the Δz (or the exit of the material). From this the effect of multiple scattering is calculated and used to modify the muon's direction. If a magnetic field was present, the direction change from this was also included. The continuum contribution to the energy loss is subtracted from the energy. The probability of a discrete loss above 10 MeV is computed for each of the four processes. If an interaction is chosen to occur, then the actual energy loss is chosen from the spectrum above 10 MeV and subtracted from the muon energy. The muon position is then extrapolated in the direction of motion by the step length. This process iterates until the muon leaves the detector or drops below 250 MeV.

Calorimeter Tracking

In general, muons in the calorimeter were treated as passing through a homogeneous, isotropic average medium. No attempt was made to take into account the actual placement of target planes and active elements. The exception to this rule were events generated using the complete GEANT MC where the data acquisition system was simulated for all particles in the entire calorimeter. The muon tracking fit code (MTF) can actually be run in the case of the GEANT counterfeit "data". In the case of the propagation through the uniform block, the effective MTF fit is calculated from the vertex and exit point position and momentum direction, suitably smeared according to the measured resolution.

Spectrometer Simulation

The simulation of the spectrometer proceeded along similar lines with a few modifications. Unlike the calorimeter the toroids can not be modelled as a homogeneous block. A single set of VLIB routines were used consistently throughout the muon processing, independent of whether the calorimeter information was simulated using GEANT or VLIB. These routines accounted for the different possible media: the iron toroids, with an associated magnetic field strength depending on which magnet and the radius from the center; the air gaps between toroids; and the lead shot used to fill the center holes in order to range out hadrons exiting the calorimeter. The almost negligible effect of the sheets of scintillator and the aluminum drift planes between the toroids were not represented in terms of contributing to either energy loss or multiple scattering.

As the tracked muon stepped beyond the z position of the back face of each magnet its trajectory was straight line extrapolated and a record made of the transverse position at the central z position of any drift planes in the gap. If the extrapolation was within the covered area then the appropriate W or V position (and slope) was recorded and it was straight line stepped to the front face of the next magnet. Thus when the procedure was done one was left with a list of true positions at each of the drift planes. This was repeated for each muon entering the spectrometer.

In order to turn the exact hit positions into simulated drift plane hits the relative placement of the wires was needed. The true space positions of individual wires

were not used, instead there was an arbitrary shift corresponding to the RMS due to the wire spacing given to the first wire. Once the shift was established in a plane all other positions in that plane were consistent relative to it. Thereafter, hits are merged and grouped in the same way as the real detector. Exact hits were converted into one of the three possibilities: a single wire hit; a clean drift hit pair with consistent timing information; a cluster of more than two wires signaling a hit. The actual chambers had essentially a 98-99% efficiency for recording some type of hit (single, pair, multiple hit cluster) for every muon passing through it. In generating simulated hits the probability of each type was chosen in accordance with the measured frequency, but there was no correlation of this choice with the process of projecting the muon through the system. Namely there was no coupling of a discrete energy loss in the latter part of an upstream toroid to the increased probability that the hit be classified a cluster in contrast to a clean pair.

In addition to all the hits from muons associated with the event, there also exists the possibility of drift chamber hits from uncorrelated sources. These background hits can arise due to electrical noise in the drift electronics, breakdown in the the gas, cosmic rays, and unvetoed muon generated upstream of the detector[2]. Such additional hits will tend to add to the confusion of hit selection and fitting. To simulate this effect, randomly placed background hits were generated using frequency of each type, uniformly distributed over each plane. The probabilities in each plane was derived from distributions in the data after the fit muon's hits were removed.

---

[2]These muons could be from veto failures, or from muons that bypassed the veto wall and strike an exposed edge of the drift plane.

When complete the combined list of smeared hits and background noise was presented to the analysis software in a form analogous to that of real data. From that point on the analysis continued along the same lines, with the only exception being the fine details of how the clean back-to-back drift pairs were dealt with due to the lack of simulation of hits for the individual wires. The small differences in handling the clean pair hits should not be a source of much error since fewer than 9% of all hits fell into that category and the inherent differences in modelling the effect of clean drift pairs was not too different from reality. These differences arise mostly due to choices in coding the routines to simplify the simulation.

3.5   Adjustments by Reweighting

Often it is necessary to study the sensitivity of the results to the input parameters of the model. This is generally accomplished by event *reweighting*. This method reassigns each MC event a new weight. The weight is the probability of such an event with the new values for the parameters divided by the original probability. An example scenario would be investigating the the effects of adjusting the Peterson parameter (ϵ). The weight for each event, where z_i is the z_E used in that event, would be given by:

$$w_i = \frac{D(z_i; \epsilon)}{D(z_i; 0.19)}.$$

This procedure of reweighting eliminates the need of re-running the entire MC, an otherwise time and resource consuming job.

It was determined that the Atherton model for the neutrino flux needed a correction. A better agreement between the data and MC E_ν distributions could be obtained by adjusting the kaon fraction up 10.5%. The reconstructed numbers of neutrinos to anti-neutrinos could be harmonized by using $w_{\bar\nu} = 1.08$. The overall normalization of the total number of MC events to data events is still just a subject of how many events were thrown, as no attempt was made at flux measurements and therefore no absolute cross section comparisons can be made.

Besides the adjustments to the flux files, studies were made to determine the sensitivity of κ to: the chosen PDFs, the charm quark mass m_c used in slow rescaling, the overall branching ratio $c \rightarrow \mu$, and the Peterson fragmentation parameter ϵ.

3.6   MC Analysis

The simulation starts by generating events based on physics quantities such as a cross section, x, y, E_ν. It proceeds by calculating the physically realized exact quantities such as true kinematics 4-vectors; then generates some combination of either a simulation of what the data acquisition system would record or a representation of the smeared reconstructed values. It ends with the final reconstruction of the original physics quantities. In the case of this analysis, once the basic reconstructed quantities are present, such as the hadron and muon energies and angles, the event reconstruction proceeds along the exact same analysis path as true data using the same code.

Chapter 4

Event Selection and Reconstruction

> *... when you can measure what you are speaking*
> *about, and express it in numbers, you know*
> *something about it; but when you cannot measure*
> *it, when you cannot express it in numbers, your*
> *knowledge is of a meagre and unsatisfactory*
> *kind.*
>
> – William Thomson, Lord Kelvin

In order to be useful, the data from this experiment must be collected, sorted and classified in a manner that enables one to test predictions or otherwise allows one to extract information that can be further used to make new predictions. But before a comparison between the data and the model can be made, one must first determine the characteristics of the data that correspond to quantities in the model. Desirable qualities of this processing stage are an efficient and unbiased event selection and re-creation of the event topology and an accurate and precise reconstruction of the underlying physical kinematics.

4.1 Triggers

The first step in event selection occurs at the time the experiment is run. It is clear that there exist some class of events that are inherently "uninteresting" and therefore not worth recording; this is part of the job of triggering the detector. Examples of uninteresting events include noise; cosmic ray interactions; overlay or pileup events, where the effect of having two events makes reconstruction of either impossible; and events too puny to be reliably reconstructed. This selection was exceptionally important for the Lab C detector because once the flash chambers were triggered they were unable to be retriggered during the same neutrino spill and so possible interesting events could be lost. Thus, it behooved us to chose wisely.

In this experiment an almost unbiased selection of events was recorded using a minimum bias trigger. This required the hardware to record events that contained a minimum ionization trail in the proportional chambers. This corresponded to approximately 5 GeV of energy in the calorimeter. Further it was required that a common low threshold be exceeded simultaneously in at least two chambers. This coincidence condition was required to avoid spurious triggers due to noise. Higher bias triggers generally required more restrictive conditions. These make it more likely that one would trigger on interesting topologies, but were not used in this analysis.

In addition to the requirements of event structure, triggers were required to occur during the *dynamic beam gate* (DBG), the time when neutrinos were expected to be passing through the detector (Figure 2.5). This synchronicity between the neutrino

spill and the DBG generally excludes cosmic ray events which are uncorrelated with the accelerator cycle and thus are relatively unlikely to occur during the short (5–10 ms) DBG. The other requirement on all event triggers was the absence of a signal from the upstream veto counters. This rules out triggering on the muon of events that occur outside of the detector or the tail end of such events. It also excludes the cases where such a muon might confuse the reconstruction of an event by making a single muon event look like a dimuon event.

4.2   Flash Chamber Processing

The majority of the reconstructed quantities are derived from pattern recognition or other filtering of hits in the flash chambers. In order to eliminate biases generated by noise, an attempt was made to systematically remove hits from regions that repetitively generated hits independently of event structure. There were three sources of such pedestal or hot spot hits:

1. *overlap hits:* These extra hits are an artifact of the chamber readout system (Section 2.4.2). Amplifier-digitizer systems were attached to each end of the magneto-constrictive wire and "looked" towards the center. Hits near the chamber center would be recorded by both ends of the wire and some survived the simplistic reduction made during data acquisition. During the event processing stage, more complete information was available concerning the matching of the two ends and thus the remaining duplicate hits could be

eliminated.

2. *fiducial marks:* These extra hits are also a result of the details of the flash chamber construction. Each chamber had three small signal wires imbedded along the readout wire. These wires forced that cell to register a "hit" each and every time the chamber was read out. These are a necessary component of determining the alignment of the chambers. Since they are extremely regular, their removal posed no serious problem.

3. *hot spots:* Some regions of some chambers were either damaged or otherwise susceptible to noise. Locations that repeatedly registered hits when the detector was randomly triggered were candidates for hot spot removal. By triggering the detector outside the time window where neutrinos and the test beam were passing through it, any hits recorded constitute general background noise. Noise tables were generated listing locations that had a significantly higher than average probability of containing a hit. In actual events, hits in these hot spot regions were eliminated unless significant nearby activity was also seen in the same chamber.

4.3   Vertex

Given a set of recorded events the next stage was to determine where in the detector the interaction occurred. This was important for two reasons. Foremost, it is desirable that the event be fully contained within the detector in order to ensure

that the reconstructed quantities represent the true values. Obviously, containment of the muon is not generally possible; but this restriction of its origin enhances the probability that it enter the spectrometer. Secondly, finding the vertex was a pre-requisite for many of the other reconstruction steps that use this information as a starting point.

Vertex reconstruction was performed by a software package called VRTDRV. This multi-step procedure begins by determining a crude approximate position for the beginning of the interaction based on proportional chamber HITBITS and latches in two adjacent planes. The flash chamber portion then proceeds as follows:

- *initial longitudinal position:* Starting 32 flash chambers upstream from this rough position, the next step proceeds to look for a sequence of chambers that matches a pattern of hits (a series of 12 chambers where 9 of them contain greater than 5 hits); the first hit flash chamber was declared the new z vertex. This constitutes the first estimate of the flash chamber longitudinal position.

- *rough transverse position:* The transverse position in each view was calculated independently without requiring a three-view match. The hits in the first 64 downstream chambers are used to fill a 20 bin histograms for each view. The first-guess position was the center between the pair of adjacent histogram bins with the maximum for that view.

- *refined transverse position:* These are further refined by fitting the centroids (as a function of transverse position in the view and z position) of the hits

within 250 clock counts ($\approx$ 60 cm) of the initial guess. The next step was to walk along this fit, looking in a road 250 cc wide, to find a series that matches the criteria for shower end (first of a group of 16 chambers where 8 have fewer than 6 hits) or the until the 64 chamber limit was reached.

- *final longitudinal position:* Starting at the shower end or the 64 chamber limit, the final vertex finder steps upstream through chambers looking in the road surrounding the initial fits for appropriate sequences of chambers (4 of 6 chambers with no hits in the window after seeing 5 or 10 hits in that view). Proceeding from this point, heading downstream again, it looks for the first chamber with 3 or more hits. This becomes the final longitudinal vertex (LVEST).

- *final transverse position:* An iterative procedure was applied using the centroids of the downstream hits weighted equally in the initial pass, and by the deviates from previous fit for the second and third passes. The position where the fits pass through the LVEST chamber defines the transverse positions in each view.

- *physical space constraint:* In the final step the three transverse positions in UXV space are constrained to a single point in XY space.

If during at any point appropriate patterns were not found in each flash chamber view then vertex-finding failure was declared. In such as case, if the hadron energy was small then an additional attempt was made to find a flash chamber vertex by adjusting the criteria and re-attempting the procedure. A second failure, or a failure in a large shower, relegated the event to the proverbial dust-bin. Studies show that

VRTDRV has a greater than 99% efficiency for finding a vertex for neutrino events with greater than 10 GeV hadron showers. The efficiency for finding so-called quasi-elastic events that consist of a muon and a very low energy nucleon was smaller, but unimportant to this analysis.

4.4 Muon Energy and Angle

The important kinematic quantities that describe muons in an event are the energy and direction. For the primary muon of a charged–current neutrino interaction the muon angle with respect to the neutrino direction was important for calculating Q^2 and x. The direction with respect to the hadron shower direction was used to discriminate between the primary and secondary muon. The measurement of the muon energy also requires that the muon direction be determined in the calorimeter in order to get a good fit in the spectrometer.

4.4.1 Calorimeter Track Fitting

Muons travelling through a medium interact only via the electroweak forces and have a relatively small cross section. Thus, in comparison to the hadronic shower, they travel an extremely long distance. The effects of multiple scattering in the calorimeter are also minor. Muon tracking in the calorimeter was done using a software package called MTF. This package relies on the characteristic signature of

a muon: a long straight track. An additional constraint was placed on candidate muons that they must originate from or near the vertex, thus the efficiency for finding muons from K or π decays in the hadronic shower was reduced. This does not have much affect on the ability to find secondaries from charmed mesons as they decay relatively quickly; that is to say that the mean distance they travel is $\gamma\beta c\tau \simeq 2.8\text{mm}$, so there is essentially no distinguishing between the neutrino interaction vertex and the charm decay vertex in this calorimeter.

Determining the muon track direction is an area where the flash chambers excel. The fine granularity in both the transverse and longitudinal directions allow multiple measurements of the spatial positions. Because these positions are recorded electronically there is no need to re-digitize as in the case of bubble chamber detectors. The projections of the muon path onto the three flash chamber orientations preserves the essentially straight line characteristic of muons and thus is suitable for line-fitting procedures. The MTF software makes preliminary coarse fits using the Muon Hit Binning (MHB) phase and then refines these fits using the Muon Pattern Recognition (MPR) pass.

Muon Hit Binning (MHB)

The essence of this procedure is a searchlight sweep from the vertex in each of the three projective views. Any muons originating close to the vertex will show up as a relatively large number of hits at a given angle with hits at all distances out to the edge of the detector. The calorimeter downstream of the vertex was divided into 40

angular bins, each with a sweep of 0.05 radians, in the range -1 radian to $+1$ radian relative to z. An example of this is shown in Figure 4.1.

The bins are then examined in adjacent pairs to allow for skewing due to multiple scattering or offset vertices. Two loops over the hits within the combined bin are performed.

- The first loop starts at the vertex and "walks" downstream counting hits (N_{ntot}) until the edge of the detector is reached. The expected number of hits and its associated error is calculated from the flash chamber efficiencies by:

$$\langle N_{ntot} \rangle = \sum_{i=1}^{ntot} \epsilon_i \qquad \sigma_{ntot}^2 = \sum_{i=1}^{ntot} \epsilon_i(1 - \epsilon_i)$$

where $ntot$ is the total number of chambers from the vertex.

- The second loop starts at the detector edge and works towards the vertex. At each chamber the quantity

$$Y_{ntot} = \frac{N_{ntot} - \langle N_{ntot} \rangle}{\sigma_{ntot}}$$

is computed. This quantity represents the number of standard deviations from the expected number of hits upstream of the current chamber. The end of the track is declared when Y exceeds -3.1

A trifling adjustment had to be made in the case of long gaps of missing hits. These were duly accounted for by restarting the algorithm, up to five times, at
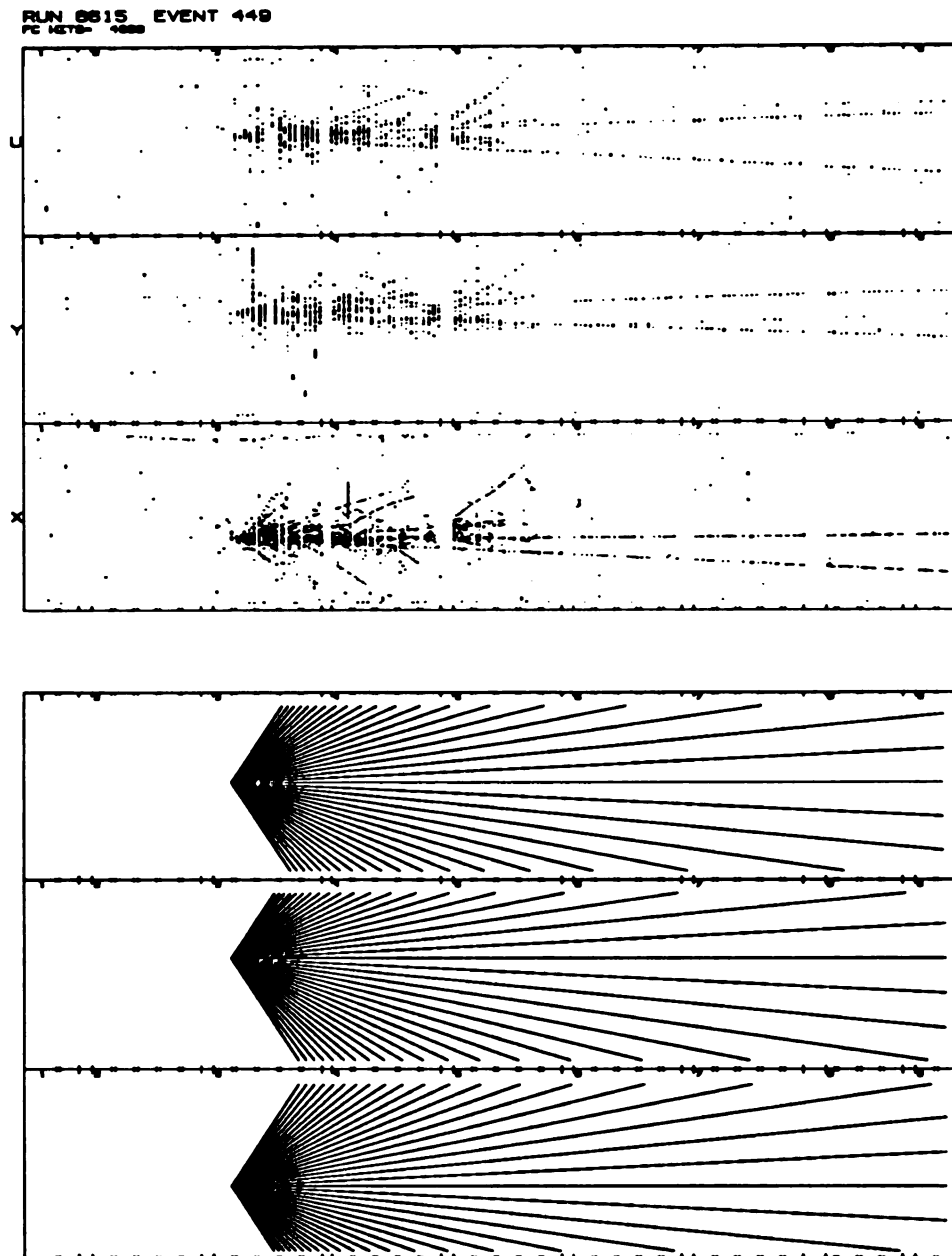
Figure 4.1: Angular binning of calorimeter by MHB

Searchlight division of calorimeter relative to the vertex. The region −1 radians to +1 radians divided into 40 angular bins.

the other end of the gap. A track length of 500 cm (DZMIN) in the longitudinal direction was required from each potential track to remain a candidate. This length corresponds to approximately 5.9 hadronic interaction lengths; thus fewer than 0.3% for the primary shower hadrons were expected to transverse this distance without interacting, though low energy or very high angle muons also fail this cut.

The last stage of MHB is to 3-view match potential tracks from each of the flash chamber orientations. All candidates passing the DZMIN criteria were further required to form at least one consistent 3-view (U,X,Y) combination. All possible combinations were tested for this preliminary match. Such a combination was required to be a solution to the constraint equation on slopes:

$$m_y - m_u + 2\tan 10^\circ m_x \le \delta m_y + \delta m_u + 2\tan 10^\circ \delta m_x$$

where the δm's are the half-width of the bin slope. Those triplets passing this constraint were also required to reach the detector edge in at least one view or travel a minimum 1000 cm (DZSUF) in all views.

Muon Pattern Recognition (MPR)

The second stage of the MTF software further subdivided the angular bins. A least squares fit was performed on the track segments within the sub-bins. The bins were chosen to maximize the resolving power of narrowly separated tracks in the forward direction, while minimizing wasted processing overhead.

Table 4.1: MPR segment bins

Projected Angle		MHB $\delta\theta$	MPR $\delta\theta$
0 – 0.1		0.05	0.00625
0.1 – 0.4		0.05	0.0125
0.4 – 0.7		0.05	0.025
0.7 – 1.0		0.05	0.05

- Within each sub-bin a least-squares fit was performed on hits starting from the initial central slope and intercept. Moving from the exit chamber of the initial fit towards the vertex, chambers were skipped until hits were found in the sub-bin.

- After a minimum of 10 chambers with acceptable hits, the running fit was followed – selecting hits nearest the projected local direction. Hits were used in the fit only if they contributed a negligible amount (< 25) to the χ^2. Hits from chambers with greater than four hits within 24 cm of the fit contribute nothing; this alleviates the problem of skewing the fit due to hits from the hadronic shower. By following a running fit, even outside the initial angular sub-bin, curvature in the track due to scattering does not imperil the fit.

- This procedure was iterated twice. For each iteration a fit was generated for each of three conditions: all hits evenly weighted, weighted towards the upstream and weighted downstream. The weighting schemes enhance the ability to follow curvatures in the track due to scattering.

The construction of the algorithm for track fitting essentially guaranteed that duplicate version of tracks would be found in the case of tracks that crossed sub-bin boundaries. Tracks found separated by two MHB bins were always considered distinct. The tracks were considered different if any of the following criteria were satisfied:

1. one fit used at least 40 hits not used by the other.

2. the average distance between hits in the same chamber was > 2.4 cm

3. no more than 14 hits were shared and the average difference was > 1.2 cm.

When two tracks were declared the "same" the newly found track superceded the old if the new one used either a flash chamber further downstream or more independent hits. Here an independent hit is one that is used by the track in question but not used by the alternative track. In either case, only one of the two was kept in the final list.

The MPR phase of calorimeter track fitting concludes, just as in the MHB phase, with a check on minimum track lengths and a three-view constraint on a triplet of (U,X,Y) tracks. Again all possible triplets were tested and any given fit in one view was allowed to be used in multiple three-space fits. Once accepted, the triplet remain linked as a unit and further processing is always done with all views in conjunction. The constraint applied in this step is more sophisticated than that used earlier. It accounts for the small chamber rotations as well as their lateral shifts. The average deviation and the variance on the deviation are required to be less than 2.4 cm and

11.5 cm^2, respectively. This is required for both the cases where all hits are equally weighted and for the case where hits are weighted by their distance from the vertex. Triplets are added to a list, which has a maximum of length of 10, sorted by length and number of hits.

Final Three-View MTF Track Fitting

The final phase of the MTF package is a simultaneous three-view fit of the matched track triplets. This also incorporates the rotation corrections in the process. At this stage three distinct fits are actually produced: using all hits; using only the hits within 400 cm of the vertex; using only the hits within 200 cm of the exit point of the track. Each fit has an associated correlation matrix, which when inverted gives the covariance matrix as well as the fit. Finally a χ^2 is computed for fit.

The downstream fit is important in its use in providing the input trajectory for the spectrometer fitting. In principle the upstream weighted fit should provide the best measure of the original muon angle, but due to average overlap with the shower it proved to be unreliable and the evenly weighted track fit was used for this purpose.

The calculation of the muon angle is derived directly from the calorimeter fit and the assumption that the neutrino was moving parallel to the z direction. The polar angle of the lepton scattering (θ_μ) is the important quantity in calculating the kinematics. From Monte Carlo studies the angular resolution from the MTF package is estimated to be $\sigma_{\theta_\mu} \approx 74$ mrad/E_μ where the energy is given in GeV.

4.4.2 Spectrometer Track Fitting

The purpose of the Spectrometer is to measure the momenta of muons. A charged particle moving in a magnetic field changes its trajectory according to the simple relationship:

$$R_c = \frac{m_\mu v_\perp}{qB}$$

where R_c is the radius of curvature and $v_\perp$ is the velocity perpendicular to the magnetic field B. Thus, by knowing the magnetic field and measuring the curvature of the track, we can determine the muon's velocity or equivalently momentum and energy. In particular this experiment used a configuration of toroidal magnets with drift chambers interspersed between them. In toroidal iron magnets the magnetic field is generally fully contained within the iron and the field lines form loops at constant radii. Because such a field is perpendicular to the axis of symmetry, which corresponds to the z axis of the detector, muons of one sign are focussed towards the axis and the other muons carrying the other charge are defocussed. To ensure the containment and optimize the measurement of muons resulting from neutrino interactions, the currents that generated the magnetic field where chosen to flow in the direction to focus μ^- in all the magnets. As a corollary it is evident that a μ^+ resulting from a anti-neutrino (or a dimuon event) will be defocussed.

Complications ensue from the processes that occur when traversing through a dense medium. The most important of these are: multiple scattering and energy loss. These non-linear, non-deterministic, asymmetric processes conspire to make

attempts at simple least-squares fits futile. Rather, this analysis takes the approach of propagating trial muons along test trajectories based on the known properties of the magnets. The input for such a procedure is the initial position and direction of the muon; the calorimeter tracking package MTF (Section 4.4.1) supplies up to ten potential muon tracks. The muon fitting package uses the same code as the Monte Carlo, described in Section 3.4.2., to predict the positions of the trial tracks in the spectrometer drift chambers. Multiple scattering of the trial trajectories is "turned off" to allow for "average" behaviour of the trial muons.

Once again, like so many of the analysis packages, the muon momentum package divides up into two distinct sets of routines. The Muon Hit Selection (MHS) package is used to associate hits with calorimeter tracks and make a preliminary determination of the muon momentum. The Muon Momentum (MM) package refines these fits and calculates associated errors. Every event had both the list of "full" and "downstream" MTF tracks processed as input to the spectrometer fitting package. In the general case of single muon events the spectrometer fit associated with the "full" calorimeter fit was used. In the event that that no such spectrometer fit was found, then the analysis reverted to using the energy accompanying the "downstream" MTF calorimeter fit. The description of how dimuon events were dealt with is more complicated and details may be found in Section 4.10.

Hit Clustering and Drift Corrections

All spectrometer fitting was done on drift plane (Section 2.5.3) hits that had been grouped into clusters. Hits in a two staggered layer drift chamber that are separated by less than 5 cm (3 wires) are grouped into a single *cluster*. Single hits have a resolution which corresponds to the width a cell (1 inch). Clusters consisting of exactly two hits in opposite layers (*back-to-back pairs*) are the only configuration where drift corrections can be applied; these give the maximum possible spatial resolution ($\sim$ 2 mm). Two hits in the same layer or groups of greater than two hits are combined to a single cluster at the average position with a concomitant error.

For the few ($\approx$ 8.3%) cases where a clean back-to-back pair with sensible drift times was registered, the position of the track can be substantially narrowed and the associated error reduced. This process relies on the drift time corresponding to a circle of possible minimum approaches centered on the wire. Two such circles define four possible trajectories that are tangential to the circles and thus potentially four points where the track would have crossed the centerline of the two-layer chamber, as shown in Figure 4.2. The four possible slopes that are solutions to the constraint on the closest approach to each of the wires is given by:

$$\tan\theta = \frac{wh + \Delta\sqrt{w^2 + h^2 - \Delta^2}}{w^2 - \Delta^2}$$

where w is the z separation of the wire layers, and h is the transverse offset stagger.
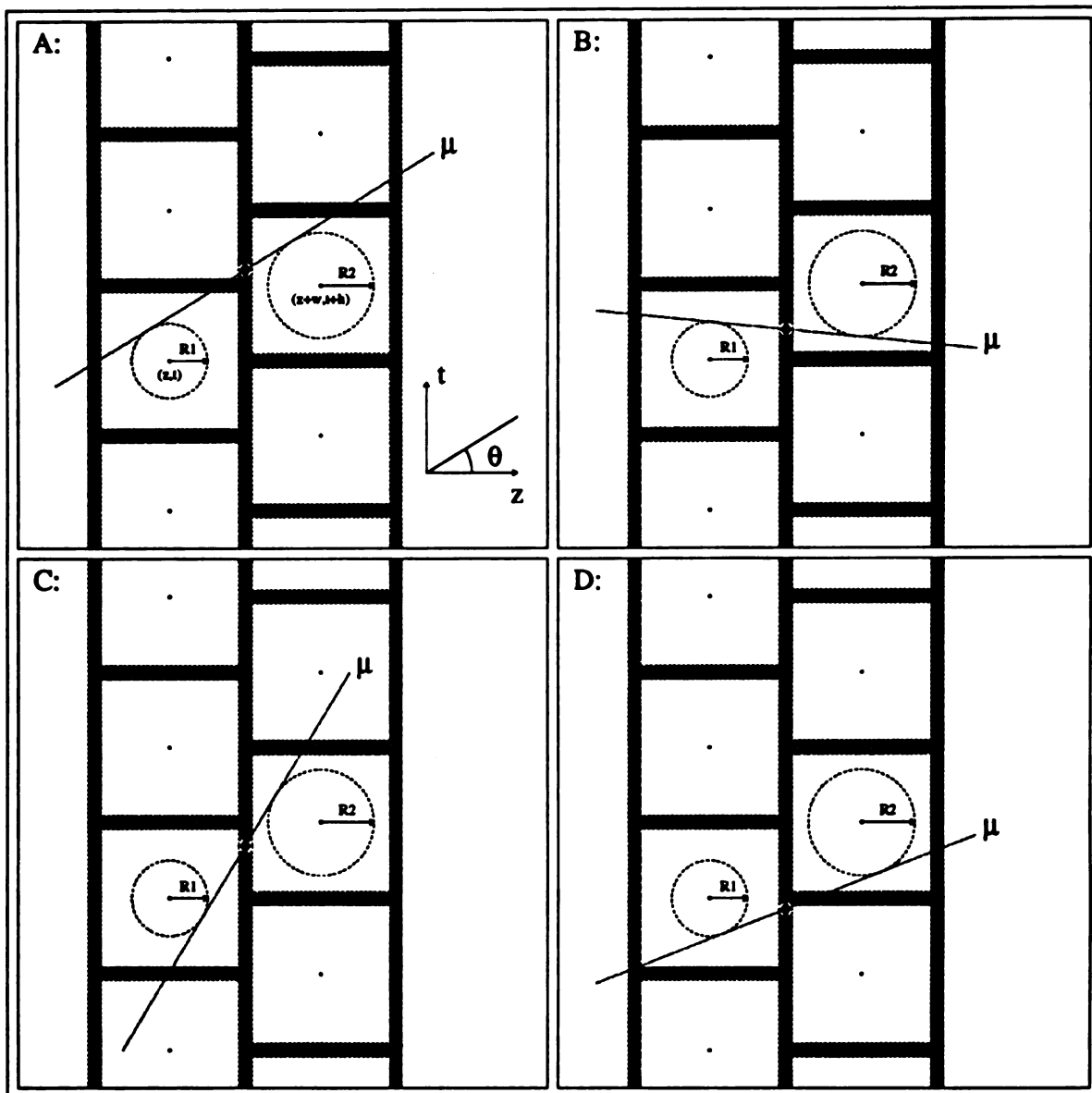
Figure 4.2: Drift Corrections Ambiguity

Examples are shown of the four possible slopes for a representative pair of back-to-back drift hits

The four slopes then correspond to the cases:

$$A: \Delta = -R_1 + R_2 \quad B: \Delta = -R_1 - R_2$$
$$C: \Delta = +R_1 + R_2 \quad D: \Delta = +R_1 - R_2$$

Given the slopes, the actual intercepts can be trivially determined from the geometry and a smattering of trigonometry.

This ambiguity can be further resolved by using the current fit trajectory to exclude unrealistic slopes. The intercept positions from the remaining slopes were averaged if more then one remained. Because a fit is required to make this distinction, the drift corrections are not applied until the MM phase.

Muon Hit Selection and Initial Fit

The purpose of the MHS package is to select which hits are associated with which tracks and reject hits due to noise. Such an association can not be made without, in the process, producing a rough momentum estimation. At this stage no drift timing information is used; this breaks the circularity of needing to know the trajectory to determine the position and needing the position to determine the trajectory. It also reduces the amount of processing necessary at this preliminary stage.

In the first part of the processing the calorimeter tracks are considered to be wholly independent and any particular hit may be used in the fit of numerous calorimeter tracks.
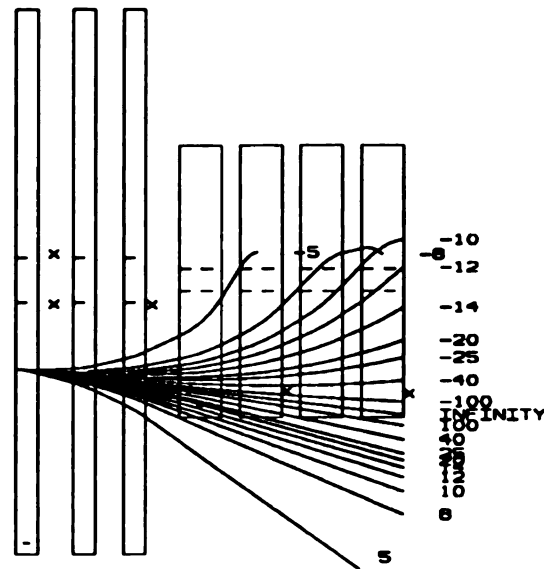
Figure 4.3: Muon trajectories in the spectrometer

Trajectories of 19 combinations of muon momenta and charge, tracked through the spectrometer system. Bending due to the magnetic field and continuous energy (dE/dx) loss are included in the simulation.

- For each incoming calorimeter track, 19 trial momenta are projected through the spectrometer system. For simplified notation, muon "momentum" magnitude (and "energy") were dealt with as signed quantities where the sign corresponded to the charge of the muon. Thus the 19 trial "momenta" were: ± 5, ± 8, ± 10, ± 12, ± 15, ± 20, ± 25, ± 40, ± 100, ∞. The infinite momentum case corresponds to a muon, of either sign, undergoing no bending in the magnetic field. It is the deflection that is actually measured, and thus it is more appropriate to speak in terms of the reciprocal of the momentum which will be denoted as ω throughout this section. A representative family of trajectories can be seen in Figure 4.3.

- Starting from the chamber furthest downstream, each hit was examined relative to the predicted hit positions of the trial momenta to find a consecutive pair of momenta that resulted in positions straddling the real hit. A new potential fit momentum was then generated by doing a simple linear interpolation of the reciprocal momenta. Alternatively, upon failing to find a pair that straddled the real hit, an extrapolation was done using a "close" pair; a hit was considered close if it fell within a road of 10 cm $+ 2\sigma_{scattering}$. The newly predicted reciprocal momenta (ω_{pred}) should then, in first order, produce a trajectory that passes exactly through the hit under examination.

- Given an initial trial momentum the routine enters a loop that iterates up to five times. The process begins by choosing a trial value $\omega_{trial} = \omega_{pred}$ and proceeds as follows:

  - Starting with an initial reciprocal momentum, ω_{trial}, and the closest two of original 19 momenta, predictions are made of where hits would lie in all 8 chambers.

  - The list of actual hits is then searched for the hit closest to the predicted position that lies in that chamber within a road of half width 10 cm $+2\sigma_{scattering}$. A count was made of wire layers (2 per chamber) that were passed in an active region and the number without hits where hits were possible. Counts were also kept of the number of hits in a plane outside the road; a separate account was kept of each type of hit: single hits, back-to-back pairs, and larger clusters.

— From the two lists, predicted hit positions and actual hit positions, the residuals and the slopes of the residuals, a prediction of a new ω_{trial} is made using a rather clever method.

We can begin by defining some terms: ω_0 represents the initial reciprocal momentum, while ω' signifies the improved prediction. The measured position in the i-th plane is denoted by y_i; while the predicted position, using interpolation or extrapolation, is given by $f_i(\omega)$. The residuals are weighted by $w_i = 1/\sigma_i$; σ_i represents the sum of the errors due scattering effects and the intrinsic measurement limitations.

The χ^2 of the yet undetermined ω' (which hopefully is close to the minimum in χ^2) is then given by:

$$\chi^2(\omega') = \sum_i w_i(y_i - f_i(\omega'))^2.$$

If one further assumes both $\omega' = \omega_0 + \delta\omega$ and the linear relationship

$$f_i(\omega') = f_i(\omega_0) + \delta\omega\frac{\partial f_i}{\partial \omega}$$

hold in the region of interest. Then one can minimize the χ^2 by choosing

$$\delta\omega = \frac{\sum_i w_i(y_i - f_i(\omega_0))\frac{\partial f_i}{\partial \omega}}{\sum_i w_i\frac{\partial f_i}{\partial \omega}\frac{\partial f_i}{\partial \omega}} \equiv \frac{S_{num}}{S_{den}}$$

It then becomes apparent that $\omega' = \omega_0 + S_{num}/S_{den}$ and $\chi^2(\omega') = \chi^2(\omega_0) - S_{num}^2/S_{den}$. Note that the new χ^2 is the original value minus a positive

quantity and thus always smaller. The estimated error in ω' is $1/\sqrt{S_{den}}$. The only remaining difficulty lies in calculating the terms $\frac{\partial f_i}{\partial \omega}$. One can approximate these by using the difference in position, in any given plane, from the closest pair of reciprocal momenta divided by the difference of the same two reciprocal momenta.

— Having calculated an estimate for the minimum χ^2 using all the real hits, the procedure may then choose to eliminate some fraction (15%) of the hits from the fit. The criteria for eliminating a hit is the requirement that the probability of getting a worse χ^2 when the hit is removed from consideration must be six times greater than the confidence level using the hit. If a hit is eliminated the new χ^2 and ω' are calculated.

— This process iterates until $|\omega_0 - \omega'| < 0.01 S_{den}$ or until the maximum iteration limit is reached.

• The final value of ω is then projected through the spectrometer system and the more precisely determined predicted positions are noted. The correlated χ^2 is calculated using these positions and the previously selected hits. This calculation includes the errors due to the uncertainties in calorimeter fit and their correlations.

• Simply minimizing the χ^2 is not a sufficiently powerful criteria for selecting hits; it is far too easy to get a low χ^2 simply by fitting one point exactly (e.g. a single random hit, using a soft trajectory). To discourage this type of errant behaviour the algorithm minimizes a quantity called the Q-factor. This quality

factor is the negative log-likelihood as derived from three probability factors.

$$Q = -log\left(P_{\chi^2} \cdot P_{miss}(m,l) \cdot \prod_{i=1}^{3} P_{noise}^i(n)\right)$$

The P_{χ^2} factor is just a straight forward application of the definition of χ^2. The factor $P_{miss}(m,l)$ represents the binomial probability that there were m or more wire layers (two to a chamber) in the road that did not register hits when the predicted trajectory passed through l layers. This discourages fits using downstream points without intervening hits; for example, it lowers the probability of accepting a fit that only uses a possibly random noise hit in the last chamber, even if it can extract a terrific χ^2. For this calculation a single average wire-layer efficiency of 88% was assumed.

The $P_{noise}^i(n)$ factors accounted for the increased probability that hits in the chamber are normally associated with a track. Hits outside the nominal road are considered noise. By assuming a Poisson-like distribution for this noise one can calculate the probability of having n or more noise hits of each type (single, back-to-back pair, cluster) outside the road. Thus this factor penalizes fits that do not include all the available hits. Unfortunately this ultimately relies on the assumption that there is really only one true track and all other hits strictly represent noise. In the case of dimuons the importance of this factor is decreased due to the "noise" of the alternative track which drives the overall importance of P_{noise} down.

- Once the Q factor is computed it can be compared to the current best fit for

this calorimeter track. An additional bias is added against very soft (< 3 GeV) fits. Another penalty factor is applied against fits where the number of hits in the road increases, as this is can be considered an increase in the noise in a small fraction of the toroid system. A fit with a lower Q factor replaces the current best fit for that given calorimeter track.

- The process then continues on to the next hit in the drift plane, and when those are exhausted, to the next upstream drift plane. Hits already used in the current "best fit" for that track are skipped.

When complete, the algorithm is left with at most one fit for each calorimeter track, each with the lowest possible Q factor for that incoming track. It is possible that there is no momentum that will allow a calorimeter track to bend sufficiently to meet any of the actual hits and thus such a track is eliminated from further consideration. The fit with the overall lowest Q factor is designated the "best" fit and all the remaining tracks are re-processed through the whole gamut with the requirement that they ignore any hits used in the "best" fit. This is *not* to be confused with excluding all hits within the *road* of the "best" fit. By re-processing the fits, dimuon events are less likely to be confused by hits from two narrowly separated muons. While it is entirely possible that two distinct tracks overlap in a particular view in a particular chamber, it is very unlikely that this will occur more than once and thus this algorithm eliminates a number of spurious duplicate fits arising from multiple calorimeter fits of the same track that were otherwise considered distinct.

Muon Momentum Determination

This phase of the spectrometer fitting loops over the set of calorimeter tracks that pass the MHS package and their associated drift chamber hits and initial momentum determinations. At this stage corrections to the transverse positions can be made to any back-to-back pairs selected for use in a particular fit after the reciprocal momentum determined by the MHS package is re-projected through the spectrometer system and the slopes at each drift plane location are recorded.

Starting with the rough determination of $1/p$ and $\delta(1/p)$ as determined by MHS a search is done for the minimum of χ^2 as a function of reciprocal momentum.

- Seven reciprocal momenta are projected through the system. These seven are centered at the current best prediction and distributed equally within the error range. Those which predict a hit for each plane that has a hit selected are considered acceptable. If no acceptable projections are found the range is expanded by a factor of two. If less than five are found then the road is narrowed by a factor of two. In either case the process restarts.

- For each of the acceptable momenta the correlated χ^2 is calculated. A least-squares fit to a parabola, $\chi^2 = a + b\omega + c\omega^2$, is performed. Finding a maximum, rather than a minimum, results in the process being restarted with the range expanded by a factor of four. Otherwise the reciprocal momentum of the minimum is computed along with the estimated χ^2_{min} and an estimate on the inverse momentum's error $(1/\sqrt{c})$.

- If the new minimum is predicted to be outside the current fit region, then the region size is widened by a factor of two and the starting value moved such that the old starting value constitutes one of the extrema of the range. Again the process starts over for this case.

- Once a χ^2 fit passes all the above criteria it is proclaimed a success. Another attempt at a parabolic fit is performed using twice the range. This whole process iterates until either the maximum number of iterations (10) is reached or there are two successful parabolic fits in a row.

The processing of a calorimeter track ends with a final projection of the final momentum and re-calculation of both χ^2 and the Q-factor. A summary of other information is also recorded: the total amount of iron traversed; the distance travelled through the holes in the centers of the toroids; and the total integrated magnetic field seen by the track (i.e. $\int B \cdot dl$). Later cuts are applied to some of these quantities in order to eliminate events where the measurement quality is low (e.g. low amounts of iron or high amounts of hole traversed).

The very final requirement of a fit, at this stage, is that the fit must use at least two hits in one view (X or Y) and the other view must use at least one hit. This restriction ensures that there is a reasonable expectation of a real measurement of the three-dimensional character of the track. It also excludes mis-matched calorimeter fits that do not represent true muon trajectories. By requiring two hits in at least one view an effective minimum distance through the iron is set on the muon; this

helps ensure that sufficient $\int B \cdot dl$ was available to see a substantial deviation.

Total Muon Energy Determination

All determinations of muon energy to this point have been relative to the beginning of the spectrometer system. Corrections must then be made for the $\frac{dE}{dx}$ energy loss in the calorimeter. Because the rate of loss at any point depends on the current energy this problem becomes a partial differential equation for which there is no simple analytic solution. Lacking such a solution, the problem is solved by running the original physics "backwards": stepping the muon in reverse from the spectrometer, where the energy is known, towards the vertex. As the muon is moved backwards it "gains" energy as determined by the mean energy loss equation and an average calorimeter medium. These gains are integrated over the track length to determine the mean energy loss. This energy when added to the spectrometer energy will approximate the actual original muon energy. This correction ranges from approximately 1.8 GeV to 4.8 GeV, with a mean value of 3.1 GeV. The sharp cutoffs at the two endpoints are a direct result of restricting the vertex to a fiducial volume (Section 4.9).

4.5 Muon Elimination in the Calorimeter

Events containing muons must have those muons "removed", in some fashion, from the calorimeter before properties related to the hadron shower can be established. The package MCH, working in close harmony with MTF, was designed to do that job.

It is important to note that the actual hits chosen for use in a fit were stored away while the MPR portion of MTF was processing the calorimeter fit.

- *initial processing:* A calorimeter MTF track is chosen to be eliminated. A count was made of the number of hits within four roads centered on the actual hit used in that view. If no hit was used, then the roads were centered on the fit. The roads had half-widths of 12, 24, 48, 96 clock counts (or ≈ 2.9, 5.7, 11.5, 23.1 cm, respectively). These values were stored away for every chamber.

- *shower-muon separation:* Different algorithms were used in the decision to eliminate hits depending on whether the muon overlapped the shower. Moving from the vertex, considering only chambers that have hits within the widest of the roads, a sliding window of 8 chambers (or 16 chambers in the case of the X view) was examined. If the average difference in occupancy between the outer road and the inner most road fell below a threshold of two hits, then the separation point was declared for that view. A global separation point was set to the maximum of the three views, and all further processing was in respect to the global point. In each of next three steps, the number of hits "associated" (n_{assoc}) with the muon was determined by excluding those in roads wider than the narrowest road that contains no additional hits.

- *hit selection within the shower:* In this section each chamber from the vertex to the muon separation point was examined, looking in particular at the difference in the number of hits in the 12 and 24 clock count roads. By assuming an approximate uniform shower background, the excess number of hits due to the

muon can be estimated as $n_\mu = 2n_{12} - n_{24}$. Chambers where this number was positive would later have n_μ hits removed.

- *hit selection beyond the shower:* Starting from the exit point and working backwards towards the vertex, a running weighted fit of cumulative associated hits as a function of chambers from the exit was calculated. From the local slope of this fit, an average number of associated hits per chamber was determined consistent with all three views. This formed the essence of the number of hits to delete in a particular chamber.

- *hit deletion:* This stage of processing determined exactly which particular hits were removed. The number of hits to remove (n_{del}) from each chamber was determined in one of the two previous steps. In no case were more than n_{assoc} hits removed. If $n_{del} = 1$ and a hit was used in the fit, then that hit was removed. Otherwise the n_{del} hits closest to, and including, the hit used in the fit. If no hit was used in the fit, then the hits closest to the interpolation of the fit were eliminated.

4.6 Hadron Shower Length Determination

Determination of the extent of the shower was important in order to restrict the z range that was summed over in the calculation of the shower energy. Allowing the sum to extend from the vertex to the end of the calorimeter adds unnecessary bias by the inclusion of additional sources of noise. Such noise could arise from a variety of

sources: instrumental, such as spurious electronic discharges, or random fluctuations above the quiescent state; or possibly actual additional sources of energy deposition in the calorimeter from cosmic rays or another neutrino interaction, either in or out of time. In either case, restricting the sum to the volume just sufficient to contain the shower associated with the interaction under study was obviously a prudent goal. The software package SHRLEN implemented an algorithm for estimating the end of the hadron shower

The basic concept underlying the algorithm is the assumption that the shower is inherently a contiguous "blob" of energy deposition. Adjustments must be made for the actuality that such a "blob" consists of a multitude of individual particles, but the overall characterization was still representative. The shower particles all under go interactions with the detector; in particular the charged particles leave a continuous track of ionization with no noticeable discontinuities.

As with all procedural algorithms, the method can be broken down into steps. The important points can be summarized by:

- *rough estimate:* A very crude approximation of the end of the shower comes from simply declaring it to be upstream of the last flash chamber in the sixth module beyond the last proportional chamber with an AM (analog multiplicity) latch (see Section 2.4.3).

- *general flash chamber criteria:* Flash chambers are examined within the range given by this upper limit (or the end of the detector) and the vertex. Groups

of 16 at a time were scrutinized, until a group is found that contains 6 or more chambers that failed to exceed a minimal threshold of hits. The threshold was, in general, set to 4 for events classified as neutral currents and 5 for charge current event. The higher threshold accounts for the extra energy deposition caused by the muon.

- *low density shower exception:* If there the sum of hits in threshold-exceeding chambers was fewer than 2000, the threshold was reduced by one in order to account for the lower hit density of less energetic showers.

- *final shower end:* The shower end, JEND, was then conservatively placed 16 chambers beyond the end of the group failing to exceed 6 chambers over threshold. The value of JEND roughly corresponded to what a visual scan would identify as the shower end.

4.7 Hadron Shower Energy

In determining the kinematics, strictly speaking, the quantity of import is $\nu \equiv E_\nu - E_\mu$. Often this falls victim to sloppy notation and an attempt to avoid the "too many variables, too few Greek letters" syndrome (ν appearing numerous other places to represent neutrinos); the misnomer E_h, for E_{hadron}, is often (wrongly) used as a synonym. The quantity the detector actually measures is directly related to kinematic energy of the hadron shower. Overall the difference in definitions tends to get washed out by the resolution of the measurement in the regions where it might

be of importance.

The FMMF detector has the auspicious characteristic of having two independent calorimetric systems: the flash chambers and the proportional chambers. Measurements of energy loss can only be made in these active detectors; the passive target material simply provides an additional energy loss mechanism in order to contain the event in a reasonably sized detector. Each of the systems has strengths and faults; in practice the two tend to complement each other. Hadron showers involve strongly interacting particles and it is well known that number of particles in a shower is roughly proportional to the logarithm of the energy. The flash chambers have little intervening material and thus finely sample the longitudinal shower development. This makes them ideal for the lower energy showers that are not too densely populated with particles, as these lower energy particles tend not to travel far. As the shower energy (and the number of particles) increases, the flash chambers saturate and the signal becomes very non-linear relative to the true deposited energy. At approximately 150 GeV the proportional chambers have an equal energy resolution. Above this energy the showers are well sampled by the more coarsely separated proportional chambers and the central regions of the showers tend to have multiple particles traversing the nominal flash chamber cell size.

There must be some means of calibrating any detector in order to accurately convert the measured response into a true energy. In this experiment, this was accomplished in large part via a "test" or calibration beam (Section 2.1.3). Hadrons of a known energy were injected into the calorimeter and the response measured. The

gory details of this operation can be found in the PhD thesis by William Cobau [23] with extra attention to Appendix B. Additional details concerning shower energy calculations can also be found in the PhD thesis by George Perkins [22]. Test beam data, along with cosmic ray muons, taken throughout the entire run allowed a calibration scale and time dependent corrections to be applied.

4.7.1   Proportional Chamber Energy

The proportional chamber system is the simpler of the two systems. The charge collected on each wire is proportional to energy loss of all particles traversing the cell. The collected charge was amplified and digitized for each channel. The amplifier hardware was modified before the start of the run to ensure that saturation would not occur in these chambers in energy range accessible to this experiment.

Corrections to the Pulse Heights

The output of each amplifier was corrected to remove the quiescent pedestal value and to normalize the relative gains. At the start of every data tape (approximately every 4 hours), a series of triggers were taken when no beam was entering the detector. The pedestals were derived from the average noise for each channel. The individual channel gains emerges from the analysis of the peaks in the pedestal triggers generated by the 22 KeV photon from the Cd^{109} source attach to each channel. Corrections were applied to remove environmental effects due to fluctuations in the

gas density ρ. The temperature and pressure were monitored and the variation in the gain G follows the relationship

$$\frac{dG}{G} = -7.4\frac{d\rho}{\rho}$$

A small correction was also applied to account for the minor differences in the composition of the P-10 (90% Argon, 10% Methane) gas in the four tankers used during the run. Further details on the operation of the proportional chambers and their calibration can be found in references [52] and [53].

Calculation of E_h from Pulse Heights

The shower energy was simply given by a linear relationship connecting E_h and the sum of the corrected pulse heights. The sum was to the chamber immediately upstream of the vertex through the fifth chamber beyond the shower end (JEND), or through the last chamber in the detector. Within each plane, only the channels between the outlying cell with HITBITs were used.

The proportional chambers are a form of a traditional sampling analog device and thus its resolution could be parameterized by the characteristic functional form

$$\frac{\sigma(E_h)}{E_h} = 0.001738 + \frac{1.3995}{\sqrt{E_h}}$$

where, for these constants, E_h is given in GeV.

Removal of Muon Contribution to E_h

Up to this point the proportional chamber shower energy calculation still involved contributions from any muons in the event. In processing the flash chambers, hits relating to the muon were externally removed early in the shower reconstruction process. The proportional chambers are too coarsely segmented to simply eliminate any channel that might involve the muon. Rather, the algorithm took advantage of the analog and linear behaviour of the chambers. An energy was subtracted from the calculated value that corresponded to the *expected* energy that would have been deposited by an *average* muon in the shower region.

The average energy loss of the muons in the calorimeter had previously been determined (Section 4.4.2) in order to evaluate the muon energy at its origin. The amount subtracted was then simply the fraction of the muon's path contained within the summation region. Obviously this statistically based subtraction could not account for any large energy loss interactions, but such occurrences are relatively rare.

4.7.2   Flash Chamber Energy

In contrast to the linear and analog proportional chambers, the flash chamber system has an intrinsic binary nature. Each cell either contained sufficient deposited energy to cause a hit to be registered or it did not. The threshold was sufficiently low that a single ionizing particle traversing the cell had a high efficiency. This property, on the other hand, precludes the ability of distinguishing whether a cell was crossed by

more than one track. Additional corrections for efficiencies, multiplicities and gas conditions were necessary.

The advantage of the flash chambers over the proportional chambers is the distinctly fine sampling available. They longitudinally sample the shower 16 times more frequently than the proportional chambers; the fine transverse segmentation (5.8 mm) helps reduce the problem of multiple hits in a single cell. The transverse segmentation was crucial for the excellent muon tracking capabilities.

Efficiency and Multiplicity Factors

Each of the 592 flash chambers was divided up into regions of ten cells, approximately 60 per chamber. Using nearly horizontal cosmic ray muon events taken between beam spills, tables of efficiencies and multiplicities were constructed for each region. Global tables were constructed using all events taken throughout the run; a refinement was made by modifying these tables to account for time dependent fluctuations. These tables covered limited time span and allowed for

1. flash chamber damage, repairs or adjustments.

2. gas quality variations, including H_2O contamination.

By tracking and fitting the cosmic ray muons through the whole detector a predicted number of traversals N in any given region could be calculated. If H_1 represents the number of cases where at least one hit was recorded in the region, and H_n represents

the total number of hits recorded, then the efficiency and multiplicity are defined by

$$\epsilon \equiv \frac{H_1}{N} \quad \text{and} \quad \mu \equiv \frac{H_n}{N}$$

An incomplete list of possibilities are described below (reference Figure 4.4).

- *A,C,G,J:* Fit passes through cell traversed by muon; cell registered response.

- *B,H:* Insufficient ionization was left in cell's gas to register a hit, or the energy was deposited in plastic cell walls.

- *D:* Various inefficiencies could cause a cell not register a hit. The potential list of equipment failures include: high voltage, readout electronics, and gas composition problems. All of these could be localized effects confined to limited regions of the chamber. Physics effects included: statistical fluctuations of charges left by ionization mechanisms and the recombination of ions.

- *E,F:* Bremsstrahlung and delta ray production increased multiplicity by adding to the hit associated with the muon itself.

- *I:* Random noise unassociated with the track in question could add to the apparent multiplicity. Alternatively, spurious associated ghost "hits" could be generated by the mechanical properties of the magneto-constrictive wire.

- *K,L:* The fit of the muon track could be sufficiently displaced from the actual trajectory to contribute to the measured inefficiency. Effects such as this were controlled by restrictions on the quality of the muon fits.
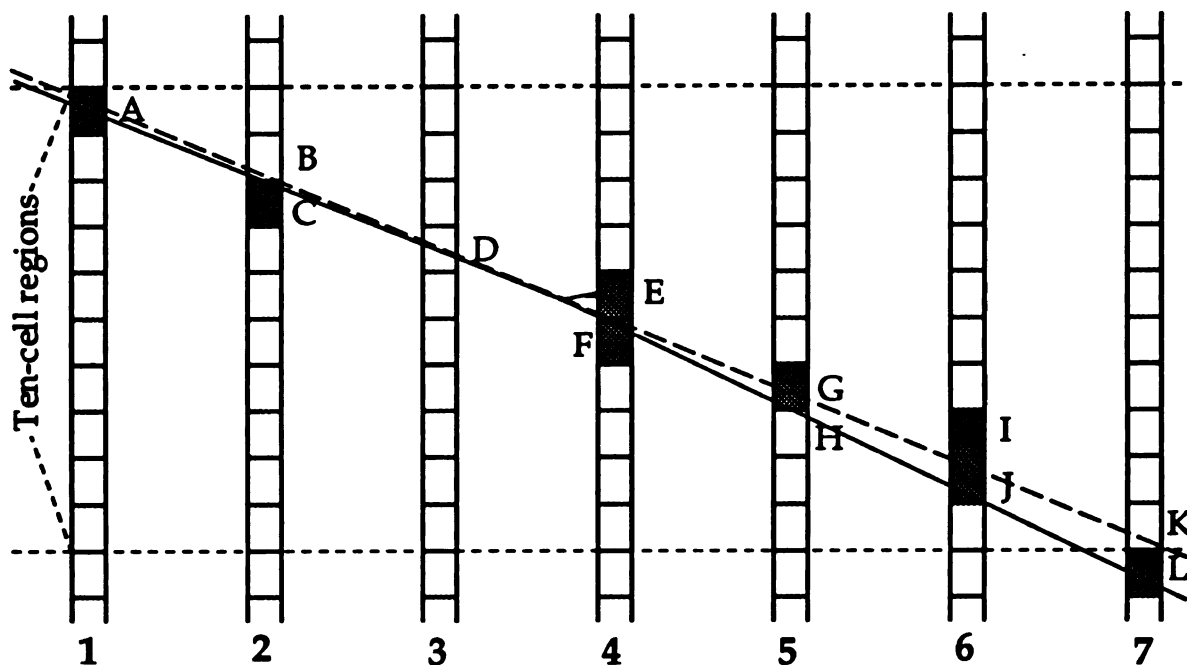
Figure 4.4: Potential sources of efficiency and multiplicity.
This illustration and associated text *illuminate some of the contributions to ϵ and μ. [22]*

- *not shown:* A large angle muon could traverse sufficient amount of two adjacent

  cells to exceed threshold for both and add to the multiplicity.

The median efficiency was $\epsilon = 0.75$ and the median multiplicity was $\mu = 1.38$. The distributions can be seen in Figure 4.5. A representative example of the efficiencies and multiplicities of the regions of one individual chamber is shown in Figure 4.6. The bins of significantly low ϵ and μ are a consequence of the construction of the flash chamber out of three panels and the configuration of the aluminum foil applied to the large surfaces. The effect of fluctuations of ϵ and μ as a function of time are shown in Figure 4.7; bins including *dead* regions ($\epsilon < 0.05$) were excluded. In general the detector was relatively stable in this time period with no major overall shift. The r.m.s of the change in individual regions was 4% and 6.5% for ϵ and μ.
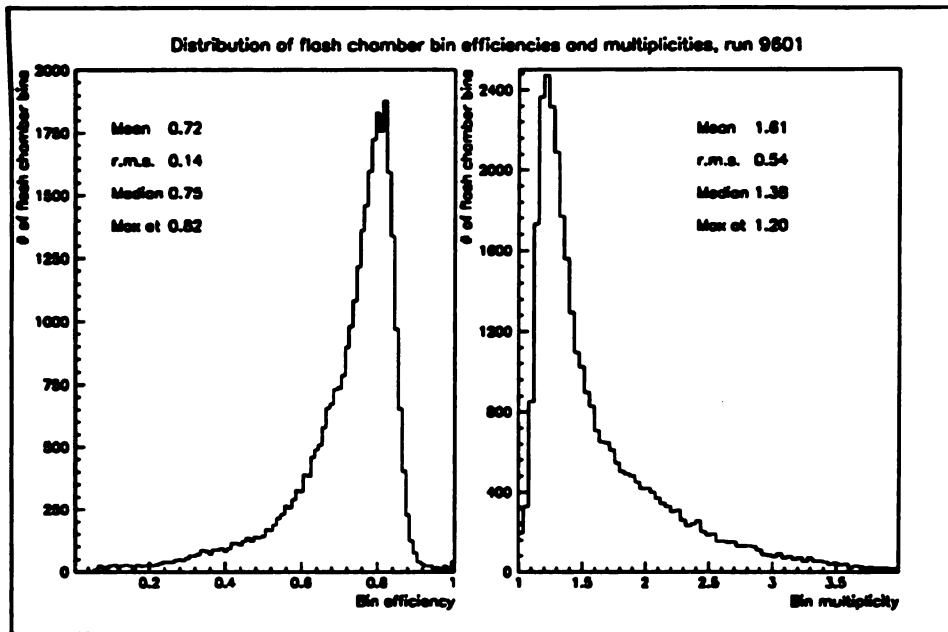
Figure 4.5: Flash chamber ϵ and μ distributions

Example aggregate distribution of ϵ and μ throughout the detector (all chambers, all 10-cell regions) for a given run. Regions declared dead ($\epsilon < 0.05$) excluded. [22]

Figure 4.6: Single flash chamber ϵ and μ

Efficiency and multiplicity of all 10-cell regions of a single flash chamber. The two runs shown are approximately one month apart. The multiplicity of this chamber is noticeably above the median. [22]
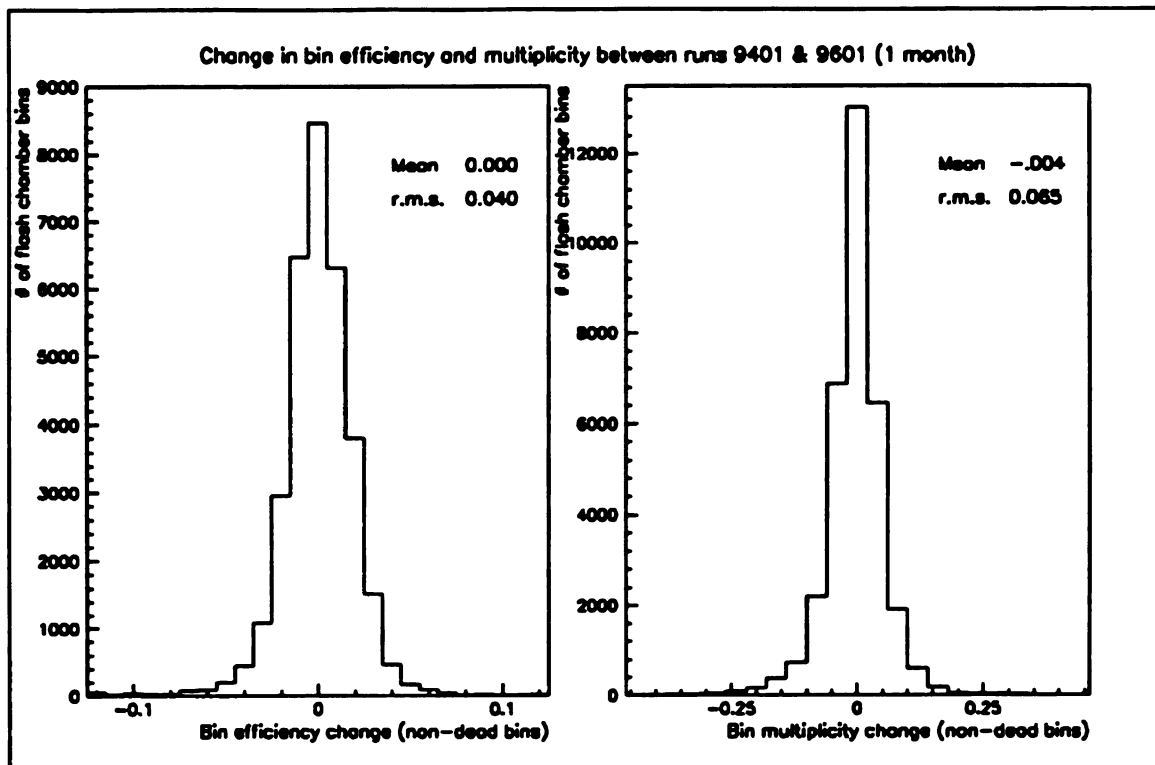
Figure 4.7: One month change in ϵ and μ

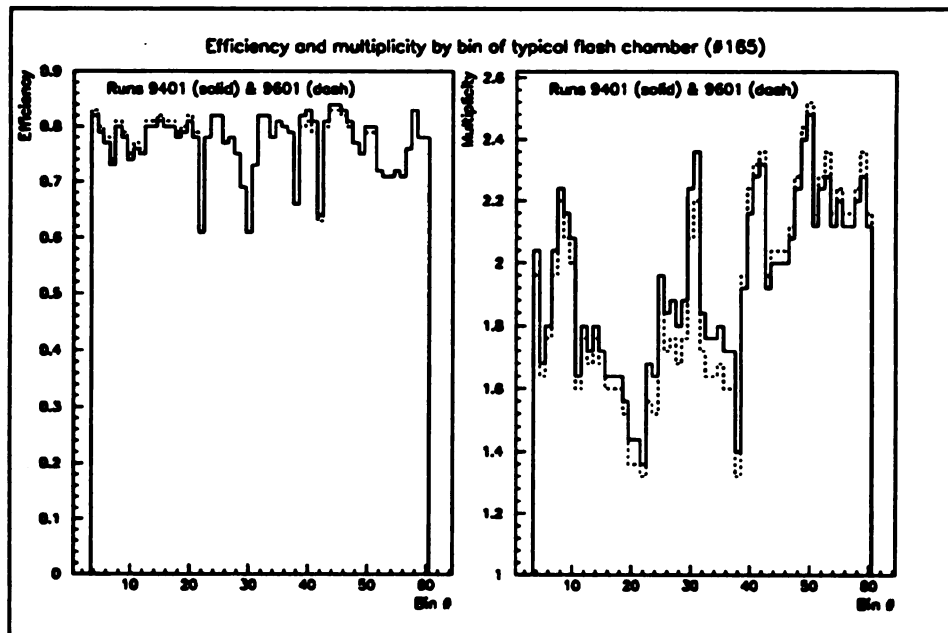The efficiencies are sensitive to the presence of H_2O in the gas, which acts to quench the plasma. The overall detector's ϵ would tend to track the humidity inside the laboratory with a time delay as the moisture diffused through the flash chamber plastic. Sufficient air conditioning during the summer, which acted to de-humidify the air, curbed this effect.

Saturation Correction

The effects of saturation, where additional energy deposition leads to no increase in the signal, becomes most important in the cores of high energy showers. Two rival schemes were derived for dealing with this problem. This analysis used an algorithm

Figure 4.8: Multiplicity and efficiency/enhancement functions

Shower hits in a 10 cell region are enhanced via a two step process. First they are corrected for the local multiplicity. Then they are simultaneously corrected for both the local efficiency and the saturation effects.
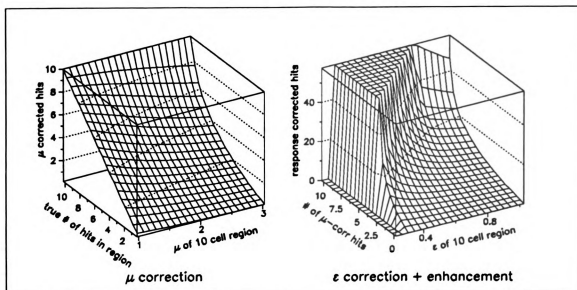
referred to as the DOOM/SHOWER method; the competing scheme's gritty details can be found in [23]. The fundamental strategy in the DOOM[1] method was to make statistical corrections based on local hit density to account for overlapping tracks.

A *response-corrected* number of hits was generated by first removing the effects of the local multiplicity; this was followed by an unfolding of the local density to account for the efficiency and the effective number of particles. The effective hit density comes from approximately inverting the binomial distribution. The combined enhancement is restricted to giving hits weights of no more than approximately 5.75. The functional form of these corrections is displayed in Figure 4.8.

---

[1]The moniker "Dr. Doom" was a self-applied nickname of a previous collaborator; it expressed the "doom and gloom" approach to data analysis that characterized his strong faith in Murphy's Law. This energy calculation method was the end result of much work on his part.

Response corrected hits are summed from the eighth chamber upstream of the vertex (LVEST), through 80 chambers beyond the shower end (JEND). Additional adjustments were made to deal with "dead" regions ($\epsilon < 30\%$) using a smoothing algorithm involving neighboring regions and chambers of the same orientation up- and downstream of the dead region. Lastly, enhancements were applied to the chambers surrounding the bay boundaries in order to accommodate the unseen energy lost in the scintillator tanks or the WIMP counters.

Obviously the enhancement algorithm does not always correctly deal with two widely separated, unassociated tracks that happen to "shadow" each other in a given projection. This and other factors presumably contribute to the final non-linearity of quadratic formula relating E_h to the response-corrected number of hits (h_{rc}):

$$E_h = 0.939 + (0.013612)\ h_{rc} + (1.788 \cdot 10^{-7})\ h_{rc}^2$$

Overall the resolution was determined to best be given by:

$$\frac{\sigma(E_h)}{E_h} = \max\left[0.10, \left(0.04 + \frac{0.8}{\sqrt{E_h}}\right)\right]$$

4.7.3   Rescaled and Weighted Average Energy

At this point the energy scale has been determined almost exclusively by the test beam calibration. This method of setting the scale retained some inherent flaws. For example, the calibration beam "energy" was calculated quantity based on magnet

currents and positions[2]; the test beam also had a finite width to the distribution in energy and a random makeup of hadronic particles (π, K, p ...). In addition some consideration must be paid to the effects of the incoming track and its energy loss. Lastly, this method of calibrating the calorimeter made no connection to the energy scale set for the spectrometer.

To counteract these failings, an adjustment of the scale was made based on the charged current y-distribution. This quantity, which is expected to be essentially flat, provides a link between the hadron and muon scales. Using a model of the E_ν spectrum and its radial distribution, the scales of individual flash chamber and proportional chamber E_h were adjusted to minimize the residuals between the measured and predicted distributions. Individual *rescale* factors were determined for each hadron energy method. No adjustment was made to the muon energy scale.

Finally the rescaled proportional and flash chamber energies were combined, weighted by their respective resolutions at the average energy. This process iterated up to ten times or until the weighted-average energy of two sequential iterations differed by less that .1%. At low energies the flash chamber determination dominated. At high energies E_h was determined almost entirely by the proportional chamber measurement. And at intermediate energies an appropriate mixture was used.

---

[2]The nominal test beam energies may have differed by as much as 7% from the true central values. The computation of the nominal energy involves knowing the relationship between the magnet currents and the induced fields, as well as assuming uniform, well understood field shapes created by the magnet poles. The magnets, in conjunction with the geometry of assorted scintillator paddles and miscellaneous collimators, produce a configuration that selects a particular beam momentum. Detailed simulations are required to understand the selection criteria. Such studies with cross checks using the Čerenkov counters, were performed on the 1985 data and form the basis for the 7% figure. Insufficient human resources prevented similar studies of the 1987–88 data.

4.8   Hadron Shower Angle

The hadron shower angle is measured relative to the z axis, which is to all intents and purposes equivalent to the neutrino direction. In neutral current events, where there is no muon, the measurement of θ_h is critical in order to determine the kinematic variable x. For single muon events it is of no import. It gains relevance again in the case of dimuon events.

For opposite sign dimuon events originating from both neutrino and anti-neutrino interactions, the event contains a muon of each sign and thus the progenitor can not be simply determined. Often the muon with the highest energy will be from the $\nu \rightarrow \mu^-$ lepton vertex and not from the decay of the charmed particle. But such a relationship does not strictly hold in all cases. One can enhance the probability of choosing correctly by incorporating additional information into the decision. Studies have shown that a muon arising from a charmed particle decay in a shower is more likely to have a smaller transverse momentum with respect to the shower axis, then that of the primary muon. Thus the need for a shower axis determination.

The need for a superior axis determination, driven by the neutral current analysis, spawned two alternative algorithms: SHWANG and HADFLO. This analysis used the SHWANG package, as described below. For comparison, HADFLO can simplistically be described as a fit to the slope of the centroids of the hits in each chamber. All three flash chamber views were used simultaneously, and the fit was constrained to pass through the vertex. A variety of lateral weighting schemes and road width cuts

make the details too tedious to fully describe here.

The SHWANG algorithm uses an angular histogram, similar but not the same as that used in MHB, centered on the vertex. For the shower determination, the angular extent was from -1.4 to 1.4 radians, in steps of 10 mrad. Ideally the contents of each angular bin should be the total energy flowing into that direction. Because of the binary response of flash chamber cells, one must settle for hits rather than true energy. All hits from the vertex out to the previously determined shower end, JEND, are histogrammed. Then the shower angle in any view is simply given by:

$$\theta_h = \sum_{bins} \frac{n_i \theta_i}{N_{tot}}$$

The situation is slightly more complex due to the possible differences in response of the calorimeter to the purely electromagnetic (electrons, photons, and π^0s) and hadronic components to the shower. The two components will have a different relationship between deposited energy and number of hits. To account for this an enhancement, similar to that applied in the shower energy determination, was applied based on the observed number of hits within ±5 *cells*, not clock counts, of the hit. This enhancement modifying the local hit density was determined not to have a significant effect on the angle determination.

A further refinement involved progressively narrowing the window by excluding bins, until reaching a 90% hit containment level, centered on the original angle. For events with fewer than 1000 hits this concluded the measurement. Otherwise the

window, now centered on the 90% containment angle, was again reduced until only 80% of the hits entered the histogram. No attempt were made to apply rotation corrections, nor were corrections made for chamber inefficiencies or dead spots.

4.9 Event Selection

Events are required to pass a series of cuts designed to eliminate problematic or poorly reconstructed events. Some events are removed because they fall in a region of parameter space that we know *a priori* are unreliably modelled by the theory or where the detector is known to have poor measurement characteristics.

A requisite condition for accepting an event was that the detector was in good working condition when the event was recorded. Certain periods of time coincided with known problems with the detector which would render the data unsuitable. Examples include hardware failures and non-standard operating conditions. Events recorded during such periods were summarily removed from consideration. Since many of the reconstruction efforts depend on the success of finding a proper vertex all events that were marked as failing that process were also ignored.

Fiducial Volume Cut

Because containment of the entire hadronic shower was crucial to correctly determining its energy, an additional cut was made to constrain the event vertex to a volume

that prevents the shower from leaking out the detector sides or running past the end of the detector into the spectrometer system. This also has the property of allowing enough chambers for the muon to separate from the shower so that its calorimeter position can be reliably measured and used as input for the spectrometer fitting. In this analysis the longitudinal vertex was required to lie between flash chambers 33 and 400 inclusive. In the transverse plane the vertex could be no closer than 300 clock counts ($\approx$ 72 cm) to the edge the active area of any flash chamber views. The shape of the volume determined by this constraint can be seen in Figures 4.9 and 4.10.

Trigger and Shower Energy Cuts

Events must also have been accepted under the minimum bias trigger. This alleviates the need for prescale corrections or otherwise accounting for differential trigger biases and their relative normalizations.

The demand that the hadronic shower energy exceed a minimum threshold is closely related to the trigger requirement. The minimum-bias trigger contains an intrinsic energy deposition threshold involving an unknown dependence on the event structure that makes it resistant to simulation. In order not to have to deal with such a problem, a hard cut is made at 10 GeV where the trigger is known to have reached its fully efficient plateau. This also excludes the troublesome region where the energy reconstruction has extremely large uncertainties.

Figure 4.9: Projected Fiducial Volume

The fiducial volume defined as the region greater than 300 clock counts from edge of active area of all flash chambers and restricted to chambers 33 to 400, as shown on standard event display. The vertex must lie within the enclosed region.

Figure 4.10: Transverse Event Distribution
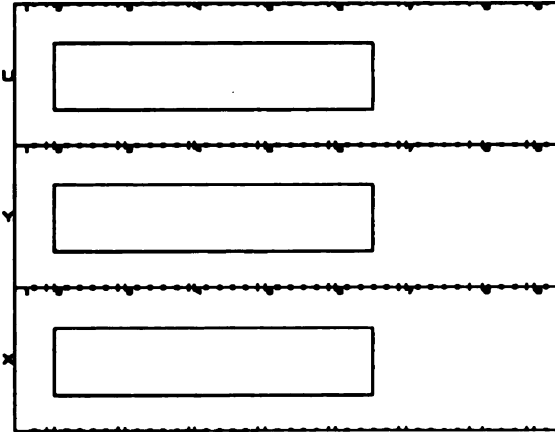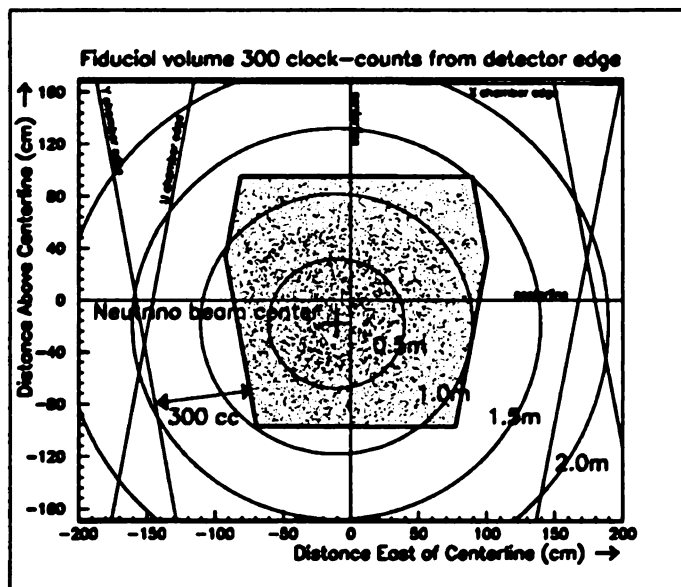
The fiducial volume defined as the region greater than 300 clock counts from edge of active area of all flash chambers. This projection onto the x-y plane also include a sampling of the distribution of neutrino vertices for illustrative purposes. [22]

Cuts on Muon Parameters

To ensure all muons are suitably reconstructed, some minimal restriction are placed on the muons. Any muon that fails such a cut is declared muon *non gratis* and all information concerning it is dropped. This has the effect of discarding single muon events that fail cuts, while dimuon events which have just a single muon fail, fall back into the charged current sample now classified as a single muon event. Most of the cuts are simply designed to ensure that the muon passed through sufficient amounts of magnetic field to allow a detectable, and thus measurable, displacement. Each muon was required to have a total reconstructed energy of 10 GeV, and pass through at least 150 cm of iron. The iron cut is almost equivalent to requiring that muons traverse the entire set of 24' magnets. Muons that travel down the central holes of the toroids, and thus are "rattled around" by the fringe fields, are eliminated by a maximum limit of 20 cm spent in the hole region. The remaining criteria was the loose restriction that the muon trajectory, as found in the calorimeter, pass within 30 cm of the vertex. This eliminates poorly fit prompt (either primary or from charm decay) muons and preferentially discards muons arising from simple π and K decay in the hadron shower.

A visual scan of candidates brought to light a flaw in the fitting algorithm. A common source of unwarranted fits were fits consisting of no selected hits in any of the third through sixth drift plane, but hits (normally classified as noise by a human) used in at least one of the last two planes. With an average wire layer efficiency of 88%, the probability of this occurring is less than .021% of the cases. Since it should

be such a rarity in real events, all muons with such a hit pattern were summarily dismissed from further consideration.

Physicist Scan

Event displays were made of all the potential dimuon events; these were reviewed by a physicist in order to eliminate events that passed all cuts but were somehow "confused". Extraneous sources of fake dimuon events arise from a number of sources:

- *cosmic rays*: secondary muon appears to pierce the detector from the side or above. Few cosmic rays survived the tracking restrictions or other cuts.

- *beam muon*: the additional MTF track arose from the presence of a muon entering the front of the detector. These are essentially veto wall failures, where the secondary muon is a result of either a decay that contributed to the neutrino flux, or from an upstream neutrino interaction.

- *event pile up*: two neutrino events occurred in the same "frame". For this experiment the time resolution (due recombination in the flash chambers) was roughly 1 ms. This is in contrast to other experiments based solely on scintillators or wire chambers which have a time resolution on the order of 1 RF bucket (20 ns). These, by far, are the most insidious of the fake dimuon events. When the two interactions are well separated there is no question of distinctness, but as the showers begin to overlap they merge together. This subtle effect confuses even the human eye-brain combination, despite its excellent pattern

recognition algorithm, and make it impossible to always discern whether there are one or two interactions.

- *single track re-fits*: A few events pass all the restrictions designed to eliminate duplicate fits of the same muon track. This generally arises due to a few spurious noise hits that fool the particular algorithm used. Human intervention becomes necessary in these relatively rare cases.

All events classified under one of the failure modes by the scanner were purged from the sample. The physicist must have some level of confidence that there are indeed two muons in the event; but events believed to unquestionably to have three were also rejected. Any event considered possibly contentious was cross checked by an independent scanner. Disagreements were then discussed until a unanimous decision was reached.

4.10 Selection of Primary Muon

Events purported to contain more then one muon necessitate additional scrutiny. Spurious "dimuon" events arising from multiple re-fits by MTF of the same muon track had to be removed from the sample. Of those candidates that remained, a determination of which muon arose from the primary (anti-) neutrino interaction, and which from the charmed particle decay had to be made. In a sign selected neutrino beam there is no ambiguity; but, in a beam composed of both neutrinos and anti-neutrinos some methodology must be employed.

Care must be taken in determining track uniqueness, in order not to eliminate a real muon track that happens to closely parallel another. Both the MTF "full" and "downstream" fits and their concomitant spectrometer fits were collected; starting with the fit with the lowest Q-factor a list of distinct tracks was generated. Two tracks were considered distinct if the tracks had an opening angle greater than 20 mrad or their mutual impact parameter were greater than 4 cm. The best fit, as determined by the lowest Q-factor, was kept except in the case of a "downstream" fit replacing a "full" fit, where an additional bias of 1.5 of log-likelihood was applied.

Events with two distinct muons, as determined by tracking, could still fail the energy, iron, hole or vertex impact cuts; such an event became a single muon event for sake of this analysis, with the additional second muon ignored. This was done in the same manner for both the real data and Monte Carlo, and does not make a significant contribution to the single muon sample.

Finally, events with two completely acceptable and distinct muons were classified as either originating from a neutrino or anti-neutrino based on the charge of the primary muon. In general, as indicated in Section 4.8, the muon with the lowest momentum component transverse to the shower axis (p_T) was chosen as the secondary muon. The true distributions can be seen in Figures 4.11a and 4.11b. The majority (82%) of the events are classified using this criteria alone.

The addition of background events and resolution effects require a slight modification of this procedure. The symbol b_i represents the closest approach distance between the muon calorimeter track fit and the found vertex.
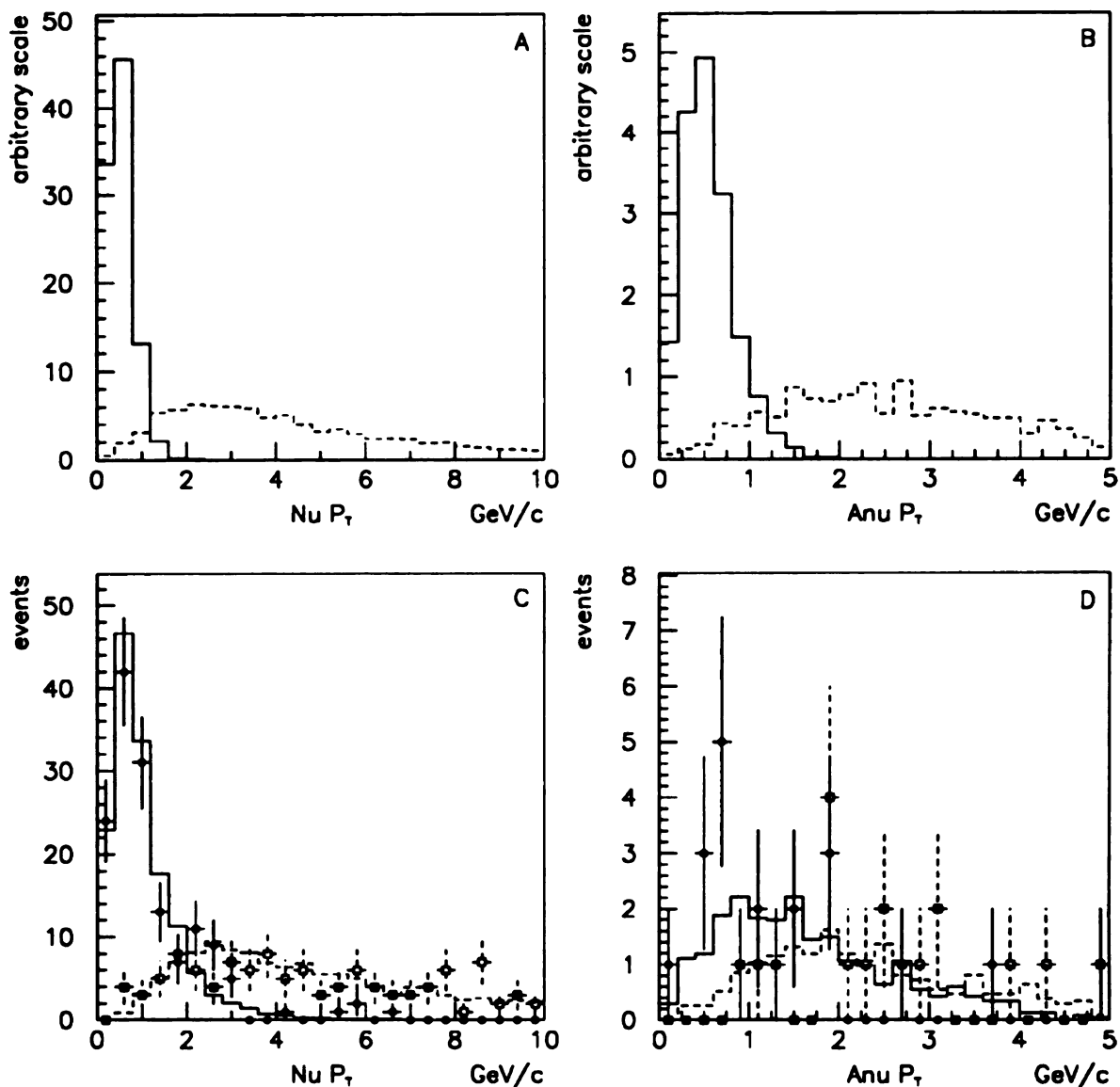
Figure 4.11: Primary and Secondary Muon p_T Distributions

Transverse momentum (with respect to the hadron shower axis) distributions. Dashed lines represent primary muon; solid lines correspond to secondary muon. (a) $\mu^-\mu^+$ (b) $\mu^+\mu^-$ Monte Carlo true distributions. (c) $\mu^-\mu^+$ (d) $\mu^+\mu^-$ reconstructed distributions using methodology described in Section 4.10. Points with markers and error bars correspond to actual data, outlines represent reconstructed Monte Carlo events (renormalized to match data).

- Events where $|b_1 - b_2| > 15$ cm are indicative of the of a muon arising from the mundane decay of π and K mesons in the shower. Such an offset would be unexpected for either the primary muon or any potential charmed particle decay, where $\langle \gamma\beta \rangle c\tau \simeq 2.8$ mm. It is also more than the deviation expected from the resolution of track fitting. By using the difference between the impact parameters, rather than an absolute cutoff, this cut is less sensitive to errors arising from an offset vertex. In cases where the difference exceeds the cutoff, the muon with the smaller impact parameter is chosen as the primary muon. This is the determining factor in 10% of the total dimuon data sample.

- The final sub-categories select the cases where both the relative and absolute p_T differences are small and both impact parameters are small. Breaking this down into components leads to the requirement on p_T's of:

$$|p_{T1} - p_{T2}| < 3.2 \text{ GeV} \quad \cap \quad \frac{|p_{T1} - p_{T2}|}{\max \{p_{T1}, p_{T2}\}} < .5$$

and the restrictions on impact parameters:

$$(b_1 < 5 \text{ cm} \cap b_2 < 5 \text{ cm}) \quad \cup \quad (|b_1 - b_2| < 5 \text{ cm} \cap b_{12} < 5 \text{ cm})$$

where b_{12} is the two line closest approach. The second part of the condition takes care of the case of offset vertices. If these requirements are satisfied then there are two more possible exemptions to the maximum p_T selection algorithm.

1. If the muon with the lowest Q-factor (log-likelihood) was also the most energetic then it was taken as the primary muon. Only 4% of the data sample fell in this category.

2. Otherwise, if the difference in Q-factors is less than 6, then the most energetic muon is taken as the primary muon. A mere 3.5% of the data were classified using this scheme.

The final reconstructed distributions can be seen in Figures 4.11c and 4.11d. There is excellent agreement between the data and the MC, though the antineutrino sample lacks in statistics. This agreement suggests that the effects of sign confusion are well understood. The procedure leads to a 7% misidentification of each true type into the alternative category. In absolute terms this leads to a large contamination of the antineutrinos due to the large disparity in the true number of events. Only 0.5% of events classified $\mu^-\mu^+$ are truly $\mu^+\mu^-$; while only of order 50% of the $\mu^+\mu^-$ sample are of the correct classification. In the reconstruction of the physics parameters, the primary muon is referred to by the label μ_1 and the secondary by μ_2.

4.11   Physics Parameters

At last, all the components necessary for the reconstruction of the kinematics of the event are in place. In the case of dimuon events there is an additional unseen neutrino that arises from the charmed particle decay. That neutrino has the potential to carry away significant amounts of energy and momentum; thus dimuons are generally less

well reconstructed. As a reminder of this extra invisible neutrino, reconstructed quantities for dimuon events generally carry the extra label "*vis*", for visible. The M_N terms in Table 4.2 represent the average nucleon mass. The functional forms are equivalent once the substitution of $E_{shower} \rightarrow E_{shower} + E_{\mu 2}$ for ν.

Table 4.2: Reconstruction of Physics Quantities

Quantity	single μ event	dimuon event
$E_{h\text{-}vis} \approx \nu$	E_{shower}	$E_{shower} + E_{\mu 2}$
$E_{\nu\text{-}vis}$	$E_h + E_{\mu 1}$	$E_{h\text{-}vis} + E_{\mu 1}$
Q^2_{vis}	$4E_\nu E_{\mu 1} \sin^2\left(\frac{\theta_{\mu 1}}{2}\right)$	$4E_{\nu\text{-}vis} E_{\mu 1} \sin^2\left(\frac{\theta_{\mu 1}}{2}\right)$
W^2_{vis}	$2ME_h + M^2 - Q^2$	$2ME_{h\text{-}vis} + M^2 - Q^2_{vis}$
x_{vis}	$Q^2/(2ME_h)$	$Q^2_{vis}/(2ME_{h\text{-}vis})$
y_{vis}	E_h/E_ν	$E_{h\text{-}vis}/E_{\nu\text{-}vis}$
$z_{vis} \approx \frac{E^{hadron}}{E^{quark}}$		$E_{\mu 2}/E_{h\text{-}vis}$

Two final cuts were applied at this stage. Events that reconstructed to energies well above those physically possible ($1000 \gg \approx 600$ GeV) were removed from consideration. In order to apply an overall equivalent total energy cut to both the single muon and dimuon samples a lower limit on $E_{\nu\text{-}vis}$ was set to 30 GeV. This makes no additional cuts on the dimuons since $E_{shower} + E_{\mu 1} + E_{\mu 2}$ is always greater than 30 GeV given previously described cuts; on the other hand, the single muon events would otherwise have a lower limit on $E_{\nu\text{-}vis}$ of only 20 GeV.

Chapter 5

Dimuon Event Background

I began to level the ranks of haughty weeds in my
bean-field and throw dust upon their heads. ...
disturbing their delicate organization so
ruthlessly, and making such invidious distinctions
with [my] hoe, levelling whole ranks of one
species, and sedulously cultivating another.
— Henry David Thoreau

5.1   Background Sources

The dimuon event is an inefficient tag of the relatively rare process of charm production. Overall it accounts for no more than a few percent of the total interaction rate. This relative rarity means that one must also consider the sources of events that mimic the chosen event configuration. These background events are often completely indistinguishable from the prompt dimuon events.

The principle source of the background is the (semi-)leptonic decay of ordinary pions and kaons (and the few exotics) that make up the hadronic showers. It should

170

be noted that this source of non-prompt, non-charm muons characteristically has a softer energy distribution than that of those from charm decay, though background and signal events both populate the available phase space. Making a muon energy cut serves to mitigate the problem since it removes background much more severly than signal events; this is evident in Figure 5.1 which demonstrates the shape differences of the two distributions. A balance must be struck, though, since in both cases one is dealing with distributions of events and not a solid upper limit on the background muon's energy. Requiring too much energy also has negative implications in terms of statistical significance by reducing the number of signal events.

Muons from the long lived π's and K's or their secondary showers will also generally happen further away from the vertex then charmed hadron decays. The impact parameter, b, was defined to be the closest approach to the vertex by the line fit of the muon track. Thus a loose cut (30 cm) on b removes a number of non-prompt, non-charm muons from the sample without greatly impacting on the muons of interest. In Monte Carlo studies this cut removed an additional $6.1 \pm 2.1\%$ of the decay background while only depleting the signal by $0.29 \pm 0.11\%$.

Another source of background comes from the so-called "pile-up" events where two interactions overlay each other enough to confuse the software into considering it a single event. If the events are reasonably separated, the impact parameter cut will often remove them from the sample. The few remaining events were removed by hand when the entire dimuon sample was scanned, in picture form, by physicists trained to recognize such problems. The possibility exists that a minuscule number remain, but
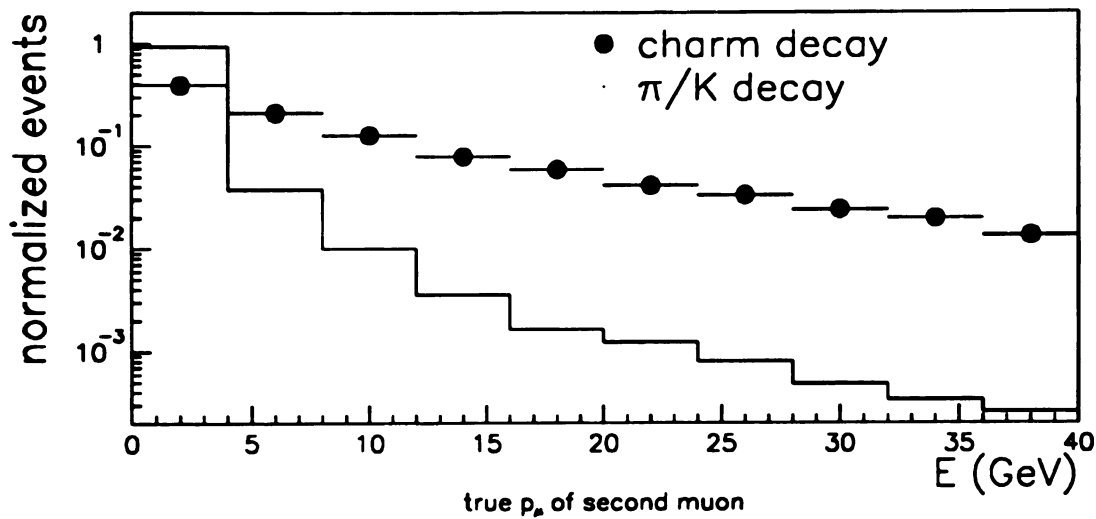
Figure 5.1: Energy spectra of secondary muons

The true E_μ distribution of muons is shown for π/K decay background (solid curve) and charm decay (filled circles). The curves are normalized to have equal areas.

it is estimated to be negligible. In addition to the possibility of having two neutrino events in a frame, there were the occasional straight-through muons that entered the detector through the front, either due to a failure to veto or by occurring after the trigger decision had been made. In either case, these were removed by either the impact parameter cut, or by hand during the physicist visual scan.

Finally, there exists the possibility of dimuon events arising from more exotic physics processes: trimuons, b-quark production, J/ψ production. Estimates of these processes show them to be of little consequence ($< 1\%$ of the dimuon sample).

5.2 Modelling the π/K Background

The spectrum of initial hadrons was generated by a fragmentation Monte Carlo. In this case the ever-popular LUND MC (Section 3.3.3) was used to simulate the interaction and provide to a list of the hadrons in the shower. The sources of the π/K shower background can be divided into two categories:

- Those arising from the decay of the primary hadrons that come out of the fragmentation process

- Those decays produced within the showers that result from the interactions of the primary hadrons and the detector.

In previous analyses of dimuon data, by this and other experiments, these two cases were handled separately. The appropriate numbers of primary hadrons were allowed to decay in the simulation before interacting. The remaining individual showers were simulated by extrapolating the results of test beam studies of the production of muons by individual pions and kaons at various energies.

From other experiments it is known that the average hadron multiplicity, $\langle n \rangle$, shows a logarithmic dependence on the W^2, invariant mass squared, of the event[1]. This can be parameterized as:

$$\langle n \rangle = a + b \ln (W^2).$$

---

[1]The dependence is approximately logarithmic with respect to almost any scale characterizing the shower: W^2, Q^2, E_h. Only the constants change in these other cases, the functional form remains the same.

Figure 5.2 demonstrates this behaviour in the LUND MC neutrino events. The scatterplot in the lower right corner has a dot-density corresponding to the bin contents. A fit to the mean multiplicity for each $\ln(W^2)$ bin is shown in the upper right corner.

5.2.1 Historical Approach

The decay parameters of pions and kaons are well understood and are enumerated, in part, in Table 5.1. The decay length is defined as $\lambda_{dk} = \gamma\beta c\tau$, where τ represents the lifetime. This equation is very nearly equal to $\frac{E_{lab}}{m}c\tau$ for these relativistic particles. This must, in turn, be folded in with the energy distribution of the particles coming out of the fragmentation, such as shown in Figure 5.3. The average energies are $\langle E_\pi \rangle \simeq 5$ GeV and $\langle E_K \rangle \simeq 10$ GeV, which leads to decay lengths of $\lambda_{dk}^{\pi^\pm} \simeq 2.8 \times 10^4$ cm and $\lambda_{dk}^{K^\pm} \simeq 7.5 \times 10^3$ cm. The charged pions that result from the decay of K mesons are treated in a similar manner allowing for the possibility of a cascade $K \to \pi \to \mu$ before any hadronic interaction with the detector occurs. These primary decays generally result in muons of higher energy than those from pions and kaons in a secondary shower and thus are more likely to pass the muon energy cut.

The interaction length is defined as

$$\Lambda_{abs} = \frac{A}{\sigma\rho N_A},$$

where A and ρ are the atomic number and density of the media and σ is the absorption cross section per nuclei. The absorption cross sections of pions and kaons

ν ⟨n⟩ vs. ln(W²)

μ= 4.11436E+00± 9.14132E-03
σ= 1.06597E+00   δ= 8.31496E-01
X PROJECTION

μ= 5.90094E+00± 2.03274E-02
σ= 2.37039E+00   δ= 1.84899E+00
Y PROJECTION

Y= 1.76071E-01± 6.32207E-02
+(1.39144E+00± 1.48748E-02)•X
MEAN Y VS X

X= 2.45385E+00± 1.91297E-02
+(2.81396E-01± 3.00818E-03)•Y
MEAN X VS Y

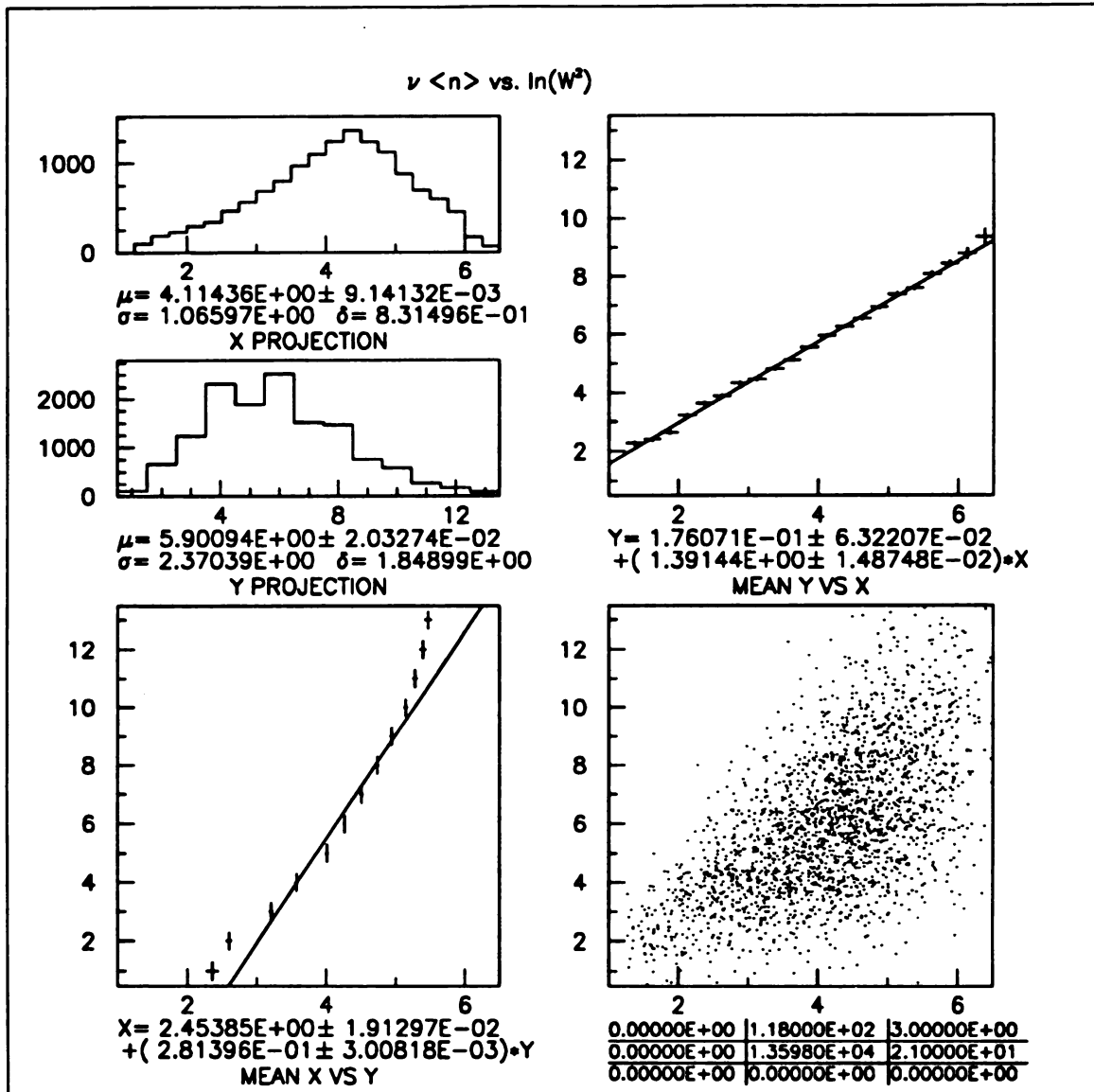| 0.00000E+00 | 1.18000E+02 | 3.00000E+00 |
| 0.00000E+00 | 1.35980E+04 | 2.10000E+01 |
| 0.00000E+00 | 0.00000E+00 | 0.00000E+00 |

Figure 5.2: Hadron Multiplicity vs. $\ln(W^2)$

The lower right plot displays the distribution of multiplicities as a function of $\ln(W^2)$ (events within a multiplicity bin are smeared over the available y axis). The upper right plot demonstrates the statement that $\langle n \rangle = a + b\ln(W^2)$ where the stairstepped lines represent the mean multiplicity for that $\ln(W^2)$ bin, and a fit is overlayed. On the left side, moving from top to bottom, are the projections onto the $\ln(W^2)$ axis and the multiplicity axis, and the (in this case, not very physically meaningful) average $\ln(W^2)$ as a function of multiplicity. The tic-tac-toe box in the lower right corner indicates the numbers of under- and overflow event as well as the number displayed in the scatterplot.
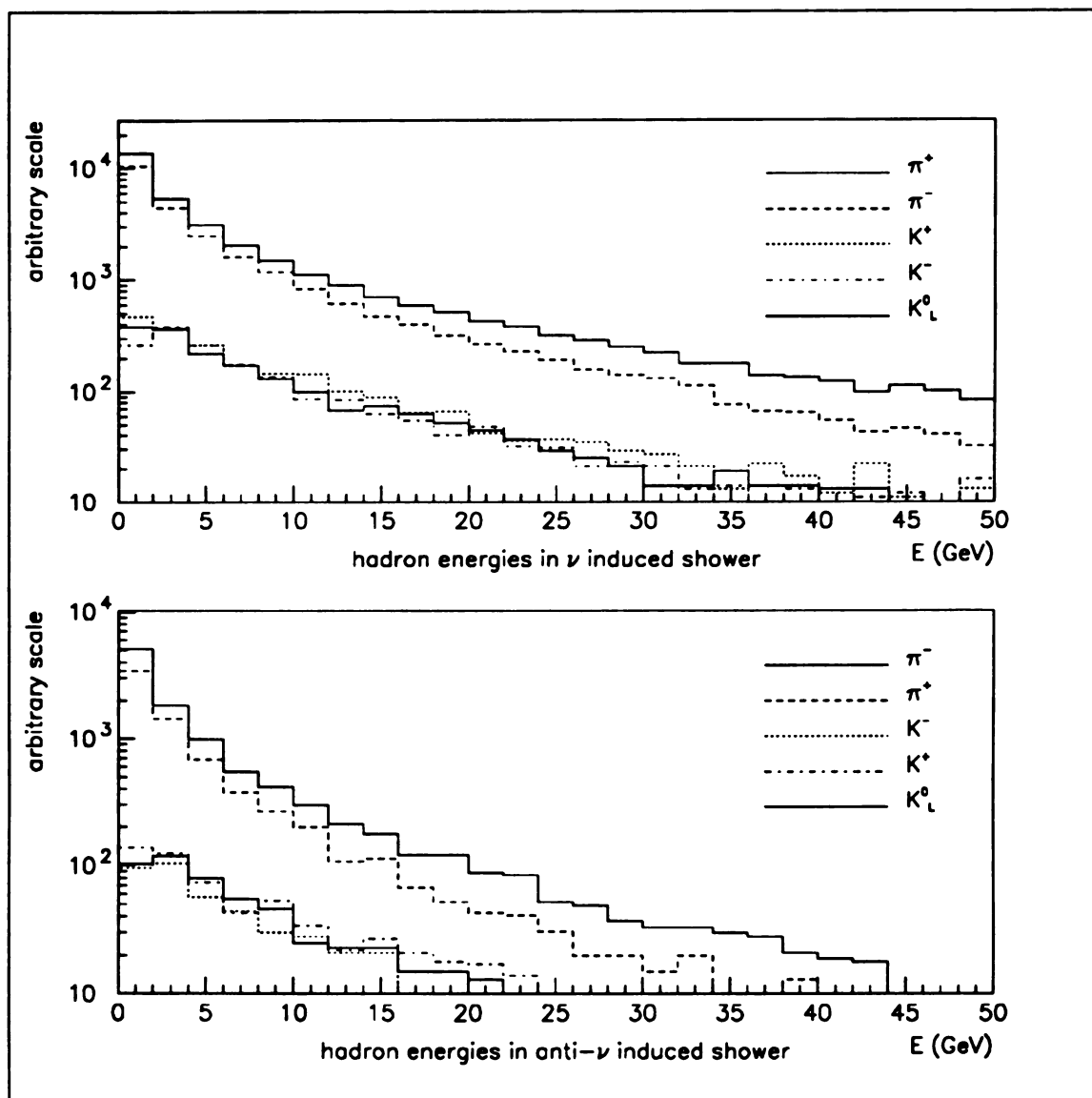
Figure 5.3: Hadron energy spectra

Energy spectra of the various components of the shower induced by a neutrino or antineutrino. The sign asymmetry (most visible in the pion distributions) is a result of the charge of the exchanged W boson.

Table 5.1: Selected properties of π and K mesons

	Branching Fraction	lifetime (τ) ($\times 10^{-8}$ sec)	$c\tau$ (meters)	mass (GeV)
$\pi^{\pm}$		2.603	7.604	0.1396
$\rightarrow \mu^{\pm}(\overline{\nu})_{\mu}$	99.98%			
$K^{\pm}$		1.237	3.709	0.4936
$\rightarrow \mu^{\pm}(\overline{\nu})_{\mu}$	63.5%			
$\rightarrow \mu^{\pm}(\overline{\nu})_{\mu}\pi^{0}$	3.2%			
$\rightarrow \pi^{\pm}X$	28.5%			
K_{L}^{0}		5.17	15.50	0.4977
$\rightarrow \mu^{\pm}(\overline{\nu})_{\mu}\pi^{\mp}$	27.0%			
$\rightarrow \pi^{\pm}X$	13.7%			

is estimated from detailed studies in the literature and includes a very small energy dependence. Such calculations are consistent with the average interaction length $\Lambda_{abs} \simeq 85$ cm[54] measured using the hadron test beam. It is patently obvious that $\Lambda_{abs} \ll \lambda_{dk}$ and as such it is much more likely that the primary hadron interacts with the detector without decaying. One should also note that λ_{dk} rises almost linearly with energy while Λ_{abs} changes negligibly and thus more of the hadrons interact before decaying as the energy of the particle increases.

Studies of the production of muons within showers were conducted by measuring the production rate within showers induced by individual pions and kaons directed into the detector by the test beam. By studying the production at various particle energies, an interpolating curve could be drawn (Figure 5.4). Unfortunately the average energy of hadrons coming from the fragmentation is below those accessible by the test beam, and so there is a reliance on extrapolating the curve into unmeasured regions. By folding the muon production spectrum (with a $E_{\mu} > 10$ GeV cut)
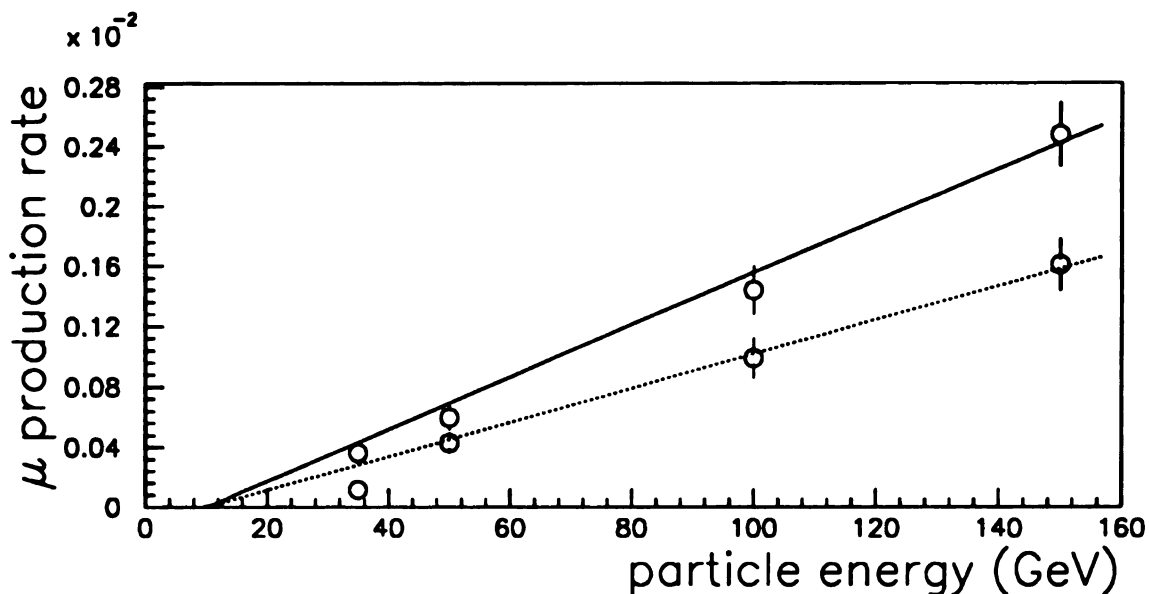
Figure 5.4: Muon production rates within hadron showers

Measured production rates with statistical errors are shown along with an linear parameterization. The solid curve represents the production of μ^+ and the dashed curve is that of μ^- produced by a test beam of π^+, K^+, and protons. Muons must be cleanly fit and pass the cut $p_\mu > 10$ GeV. The curve was required to be exactly zero at the cutoff.

into the hadron energy distribution one finds that the peak production , within the neutrino induced shower, occurs at single hadron energies of roughly 25 GeV with a long, slowly decreasing tail towards higher energies (and a sharp cut off at the low end). Data was available only for a test beam of positively charged hadrons. This charge selection accounts for the asymmetry in the charge of the muons seen in Figure 5.4. The analysis then assumed a charge symmetry where

$$R(h^+ \rightarrow \mu^+) \;=\; R(h^- \rightarrow \mu^-)$$

$$R(h^+ \rightarrow \mu^-) \;=\; R(h^- \rightarrow \mu^+)$$

5.2.2 GEANT Based Approach

Using the test beam for secondaries is fraught with systematic problems. The event vertex position distribution does not match that of neutrino showers and thus is subject to different acceptance factors. Additionally, the test beam and neutrino showers are composed of different mixtures of pions, kaons and protons, with neutrons completely missing from the test beam. Čerenkov counter (Section 2.1.3) tagging inefficiencies and a paucity of data make it impossible to separate out the difference in production rates among the sub-species. These, along with the need to extrapolate the production curve, led us to explore the use of an alternative method for the modelling of the background. Instead of creating a separate and unique Monte Carlo for simulating the decays into muons, the fragmented showers were handed over to GEANT (Section 3.4.1). The GEANT MC then transported the particles through a simulation of the detector, depositing energy, allowing decays and simulating the hadronic interaction of one hadron into a spray of others. In one fell swoop more physics was included than that easily incorporated into a single-experiment oriented simulation, with only the expense of fitting the detector description into the GEANT framework.

The investigation of muon production in a single hadron interaction was performed as a cross check using the GEANT simulation of the test beam. This comparison gave reasonable agreement as indicated in Figure 5.5. Additional corroborating evidence of the simulation's correctness comes from detailed studies of the transverse and longitudinal energy depositions of the simulated test beam showers which are
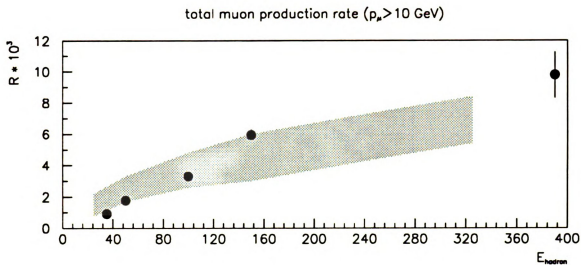
total muon production rate ($p_\mu > 10$ GeV)

Figure 5.5: Comparison of data and GEANT muon production in a hadron beam

The data points represent the measured rate of muon production in the actual test beam, statistical errors only. The band corresponds to an estimate of the GEANT values. The precision of the GEANT numbers were limited by low statistics; failing to simulate the muon contamination in the test beam, some of which escapes the filters meant to remove it; and systematics errors due to not excluding poorly simulated regions of the spectrometer system.

in reasonable agreement with the data (Figure 5.6). While not directly measuring the rare rate, it does give credence to the assertion that details of the shower are well modelled. In any event we shall see that the final fits are not extraordinarily sensitive to the overall decay background scale.
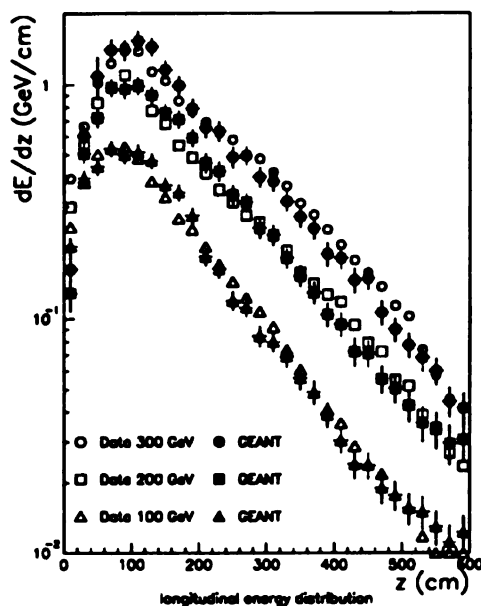
Figure 5.6: Longitudinal energy distribution comparison
A representative comparison between data and GEANT *at various hadron energies.*

5.3 Background Results

5.3.1 Event Processing

A total of 897246 events were processed through GEANT; this was accomplished by running them on the Fermilab Advance Computer Program's (ACP) massively parallel farm of Motorola 68020 based nodes. Input events were directed at any free nodes by a VAX and then processed independently on a node. Upon completion, the event was retrieved by the VAX and written to magnetic tape. The majority of the events were processed on a 30 node system which resulted in a throughput of one event every 1.25–2.2 seconds.

This rapid rate was only made possible by the expedient compromise of trad-

Table 5.2: Raw Signal and Background Rates

	reconstruct anti-neutrino	reconstruct neutrino	Sum
Charged Current	8039	45453	53492
Dimuon Sample	23	146	169
Scaled Background	.81	27.68	28.49
Statistical Error	2.01	2.78	3.43
Signal	22.19	118.32	140.51

ing off detailed simulation against speed. A full 98% of the events were run in the mode where the detector was simulated as a solid block of homogeneous, isotropic "average" material. The *soup* configuration simply recorded the production characteristics of the muons; in contrast to the *tracking* mode, no attempt was made to simulate the detector response at the chamber-by-chamber level. The detailed simulation, including the correct placement of individual detector components and air gaps, took a full 10 to 20 times as long to perform, and was thus infeasible with the available resources. The recorded rate for the generation of *true* muons of energy greater than 1 GeV in the shower was = .10696 ± .00033 (statistical error only) for the soup, and $R_{E_\mu>1GeV}$ = .1155 ± .00356 for the tracking mode. This is suggestive that one must enhance the calculated decay rate by 10% in order to match the full simulation.

5.3.2   Background Rates

The estimated number of background events is shown in Table 5.2. The statistical

error is based on upper bound estimates from the Monte Carlo. An additional systematic error of 9.7% results from the effects of uncertainty in the absorption and radiation lengths entered into GEANT for the "soup", and from variation in the relative production rates of K to π mesons by LUND. The final rate can be qualitatively compared to the results obtained using the classic method. The results of that method did not distinguish between the sign of the primary muon and so only the sum rate can be evaluated. Based on the number of reconstructed charged current events it would predict a total of $39.5\pm.9\pm4.1$ background events in contrast to $28.5\pm3.4\pm2.8$. The numbers are not quite directly comparable due to a difference in the actual cuts made (the previous method lacked the impact parameter cut which would further reduce the rate, as well as other more subtle differences).

Chapter 6

Results and Conclusions

> *There are more questions than answers; and the more I find out, the less I know.*
>
> – Johny Nash

6.1 Same Sign Dimuons

It is apropos to start off this chapter with a topic that further expounds on the π/K decay background discussed in the previous chapter, as well as to pay proper tribute to a phenomena that spawned so much effort on the part of the neutrino physics community in the late-1970's to mid-1980's. The subject of the anomalously large rate of "prompt" same-sign dimuons was investigated by numerous experiments: HPWF [55, 56, 57], CDHS [58, 59], CFNRR [60, 61], CHARM [62].

Obviously one source of same-sign dimuon events comes about from the boring process of π/K decay, which constitutes the non-prompt signal. But once subtracted from the sample what remains, if anything, is "interesting". Estimates made from

184

calculations of the associated charm production ($c\bar{c}$ pairs in the shower) would predict a rate roughly 100 times smaller than the opposite-sign rate. Experiments were reporting rates 10 times higher than such estimates. Thus, if true, this experiment should see on order 10–20 events above background. The validity of the apparent prodigious same-sign muon production was re-evaluated, notably by CDHS [63], and background rates were re-calculated. Much of the discrepancy was accounted for by correcting for the previous drastic underestimates of the π/K decay background. This should serve to underscore the care one must use when dealing with the complexities of this and other "well-understood" processes.

Additional sources of same-sign dimuons are the mis-measurement of one muon of a true opposite-sign dimuon, overlay events and trimuon events that failed to find the third muon. As evidenced by the numbers in Table 6.1 it is clear that there is no need to introduce any "new physics" processes to account for what is seen. This no new physics scenario is consistent with the latest of CCFR [64] results.

Table 6.1: Same-sign Dimuons

	$\mu^-\mu^-$			$\mu^+\mu^+$		
	events	stat	syst	events	stat	syst
π/K decay	7.9	±1.4	±0.8	2.4	±0.6	±0.2
$\mu^-\mu^+$ sign confusion	2.9	±0.9	±0.3	1.4	±0.4	±0.1
overlay, 3μ	0.6		±0.3	0.2		±0.1
$c\bar{c}$ production	0.1		±0.1	0.0		±0.0
Sum	11.5	±2.3	±1.5	3.8	±1.0	±0.4
Data	14.0	±3.7		3.0	±1.7	

6.2 Opposite Sign Dimuons

In contrast to the case of same-sign dimuons, opposite-sign dimuons are a well established phenomena with a universally accepted explanation. Their strength lies in their sensitivity to otherwise inaccessible parameters of the theory. The opposite-sign dimuon cross-section (combining Equations 1.15, 1.16 and 1.18) is:

$$\frac{d^2\sigma(\nu N \to \mu^- \mu^+)}{d\xi dy dz} = \frac{G_F^2 M E_\nu}{\pi(\hbar c)^4} \mathcal{P}(Q^2) T(x,y,E_\nu)\Theta(1-\xi) \times \qquad (6.1)$$

$$\xi\left[(u(\xi,Q)f_n + d(\xi,Q)f_p)|V_{cd}|^2 + s(\xi,Q)|V_{cs}|^2\right] \times$$

$$D_c^h(z) Br_c(H \to \mu^+ \nu X)$$

$$\frac{d^2\sigma(\bar{\nu} N \to \mu^+ \mu^-)}{d\xi dy dz} = \frac{G_F^2 M E_\nu}{\pi(\hbar c)^4} \mathcal{P}(Q^2) T(x,y,E_\nu)\Theta(1-\xi) \times \qquad (6.2)$$

$$\xi\left[(\bar{u}(\xi,Q)f_n + \bar{d}(\xi,Q)f_p)|V_{cd}|^2 + \bar{s}(\xi,Q)|V_{cs}|^2\right] \times$$

$$D_c^H(z) Br_c(H \to \mu^+ \nu X)$$

with

$$T(x,y,E_\nu) = 1 - y + \frac{xy}{\xi} = 1 - \frac{m_c^2}{2ME_\nu\xi}$$

This formulation gives a number of possible parameters of the theory to fit for. This analysis fits for three parameters: the bare charm quark mass (m_c), the relative amount of strange quarks in the nucleon ($\kappa = \frac{2\bar{S}}{U+D}$) and the semileptonic branching fraction of charmed mesons (Br_c). In principle one could also use dimuons to make statements about the Cabibbo-Kobayashi-Maskawa (CKM) matrix elements,

but these are highly coupled to the other parameters and with the current data alternative methods generally put more severe constraints on them.

The chosen parameters do not have a straightforward representation in the data such as a resonant peak might, but are instead found in the general shape and normalization of distributions of kinematic quantities. This analysis takes the approach of constructing a chi-squared relationship between the theory, represented by the Monte Carlo events, and the data. By minimizing this function in the multi-dimensional parameter space, one estimates the best-fit values for the variables of interest. This χ^2 minimization was performed by the MINUIT package [65]. The program serves as a general function minimizer and makes provisions for calculating error estimates and investigating parameter correlations.

6.2.1 Event Selection and Minimized Function

Events were selected with an eye towards excluding regions of the available phase space that are poorly measured by this experiment. The hadron shower energy requirement ensured that the trigger was fully efficient, while the variety of cuts on the muon sought to establish a respectable muon momentum determination. The base charged current event sample consisted of 45453 events identified as originating from neutrinos, and 8039 from antineutrinos. The dimuon events were included as a subset of the charged current sample. The opposite-sign dimuon sample contained 146 $\mu^-\mu^+$ (ν_μ) and 23 $\mu^+\mu^-$ ($\overline{\nu}_\mu$) events before background subtraction.

Table 6.2: Kinematic cuts

Quantity	Cuts		
$E_{\nu\text{-}vis}$	>	30	GeV
$E_{shower\text{-}vis}$	>	10	GeV
E_{μ_i}	>	10	GeV
hole traversed μ_i	<	20	cm
iron traversed μ_i	>	150	cm
impact param b_i	<	30	cm

The χ^2 function to be minimized was defined by a sum over i bins:

$$\chi^2 = \sum_i \frac{(\text{Data}_i - \text{MC}_i - \text{Bkgd}_i)^2}{(\sigma^2_{Data_i} + \sigma^2_{MC_i} + \sigma^2_{Bkgd_i})}. \tag{6.3}$$

This measure of the correctness of the model corresponds to the difference in the prediction and measured values weighted by their significance. The error on the data is simply given by the statistical error, $\sqrt{\text{Data}_i}$. The Monte Carlo and Background statistical errors are significantly smaller contributions, with the different components propagated through the re-weighting scheme.

With each of the three parameters (κ, m_c, Br_c) to be determined, one must ensure that some sensitivity to the variables exists in the distributions chosen for the χ^2 calculation. The following three seemed most suitable:

- The opposite-sign dimuons were binned at 20 GeV intervals in $E_{\nu\text{-}vis}$, combining the ν and $\bar{\nu}$ sources to improve statistical significance. This distribution is sensitive to the overall production rate, and thus a combination of κ and the

branching ratio, as well as m_c in the threshold behaviour at lower energies.

- The dimuons were also separated out into three bins of x $\{0-.1, .1-.25, >.25\}$ for the neutrinos and two bins $\{0-.05, >.05\}$ of antineutrinos. The bin boundaries were chosen in an attempt to equalize the populations. The antineutrinos are mainly due to the strange sea, but the neutrino induced dimuons come from two sources: the strange sea and the down quarks content of the nucleon. Since these two parton x distributions are very different in shape this is especially useful in separating κ from the branching ratio.

- Charged current events (single and dimuon) were binned in E_ν. Neutrinos were grouped in 10 GeV bins; antineutrinos, far less common, were binned in 20 GeV bins. They were included in the χ^2 calculation due to the m_c threshold sensitivity of *all* charm producing interactions, even those that fail to decay semileptonically.

Bins with a data-to-error ratio less than 1.225 were merged with the next bin. The charged current sample (including the dimuon events) also serves to normalize the Monte Carlo to the data. The total number of accepted MC charged current events was forced to equal the data for each iteration.

Events in the Monte Carlo sample are re-weighted as the parameters changed. Modifying the weights to reflect a new branching fraction is an unambiguous procedure as it appears strictly as a overall multiplier. The weights for different values of m_c were computed by a second-order interpolation of calculations of the cross-

section. The interpolation used calculations equally spaced between $m_c = 1$ and 2 GeV/c^2 at 0.1 GeV/c^2 intervals. In principle modifying the charm quark mass effects more than just the cross-section and its attendant turn-on threshold. It also modifies the kinematics of the produced charmed hadron, which in turn affects the kinematics of the second muon. To fully recompute the effects due to this change would be computationally prohibitive. The variation in the final result is assumed to be small for reasonable deviations around the generated value ($m_c = 1.5$).

The adjustment of the strange sea is dependent on the PDF used to generate the events for the general shape. This analysis assumes that the shape (and evolution of the shape with Q^2) is given by the original PDF and only the absolute normalization of $s(x, Q^2)$ is modified. It is important to note that this algorithm leaves the $d(x, Q^2)$ distribution unchanged. It should be acknowledged that this means the sum rules are not preserved, nor are the renormalization group equations (evolution equations) strictly satisfied after such adjustments. In actuality these distributions were never independent and, in fact, were produced in a fitting procedure by assuming some input κ. The effects of this dependence are explored by using two PDFs: HMRS(BCDMS) [36] with $\kappa = 0.52$ and MT-LO-DIS [37] with $\kappa = 1.0$.

6.2.2 Opposite-Sign Dimuon Rates

Cuts imposed on the data reduce the overall numbers of events; these cuts are normally imposed due to limits on the capabilities of the apparatus. This can be
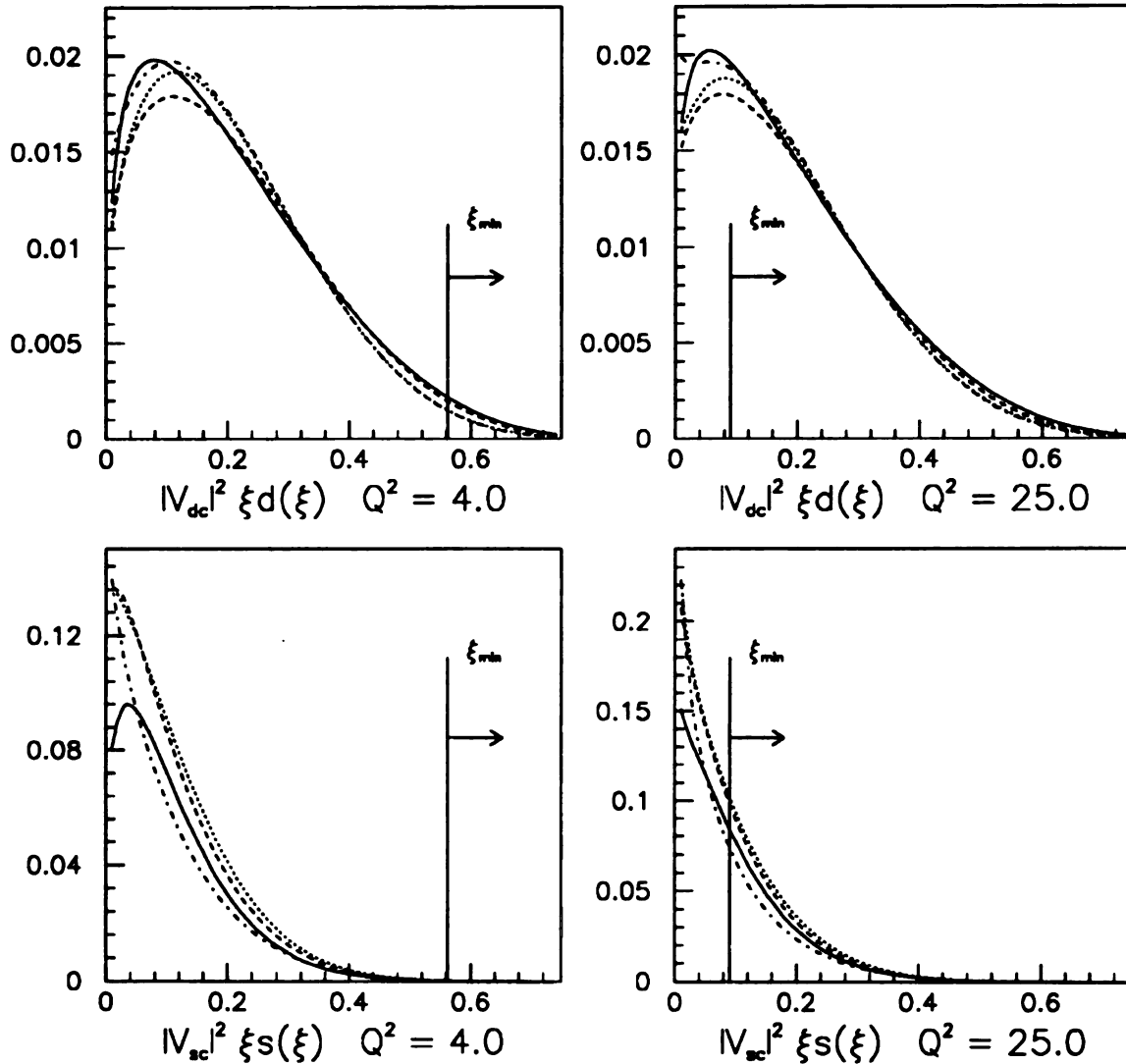
Figure 6.1: Relevant PDFs: $s(x)$ and $d(x)$

The parton distribution functions that contribute to charm production (scaled by their CKM *matrix elements) are shown for two values of* Q^2. *The solid lines represent the* HMRS(BCDMS) *distributions, while the* MT-LO-DIS *are shown as dotted lines. Parton distributions* MT-S1M *and* MT-S2M *are depicted with dashed and dash-dot lines. A representative marker is shown for the minimal* $\xi = x + m_c^2/Q^2$ *attainable under the slow-rescaling model (*$m_c = 1.5$ GeV*).*

corrected for by using the Monte Carlo events to "measure" the experimental acceptances. The corrected rates can then be calculated by the formula:

$$\text{Rate}\left(\frac{2\mu}{1\mu}\right) = \frac{[2\mu \text{ data} - \text{background}]_{\text{std. cuts}}/2\mu \text{ acceptance}}{[1\mu\text{data}]_{\text{std. cuts}}/1\mu \text{ acceptance}} \qquad (6.4)$$

where the acceptance is given by

$$\text{acceptance} = \frac{[\text{MC}]_{\text{std. cuts}}}{[\text{MC}]_{\text{generated}}} \qquad (6.5)$$

This procedures corrects the number of events seen back to the number of events expected in the fiducial volume. Small additional corrections are applied to the acceptance factor to account for minor discrepancies in the muon reconstruction efficiency between the data and the MC.

The effects of the charm quark mass can be removed, in a model dependent way, by following a similar procedure that replaces the "generated" number by the number that would have been generated had the quark mass been set to zero. This removes the majority of the low energy threshold behaviour. Some residual turn-on effects remain due to the so-called "fast rescaling" restriction. This effect is simply the requirement that the invariant mass of the recoil hadron system be sufficiently large to produce a baryon (to conserve baryon number) and a charmed hadron, *e.g.*

$$W^2 > (M_p + M_D)^2 = (2.803)^2 = 7.855 \text{ GeV}^2$$

where the proton and the D meson set the absolute minimum.

Table 6.3: Event Rates

	Neutrino			Antineutrino		
	Uncorrected					
CC Events	45453	±213.2		8039	± 89.7	
$\mu^-\mu^+$ Dimuon Signal	118.32	±15.51	± 2.76	22.19	± 6.80	± 0.08
Rate ($\times 10^3$)	2.60	± 0.34	± 0.06	2.76	± 0.85	± 0.01
	Acceptance Corrected ($m_c = 1.5$)					
CC Events	69049.4	±323.8	± 58.5	12313.5	±137.4	±264.5
$\mu^-\mu^+$ Dimuon Signal	600.94	±78.77	±18.94	166.11	±50.91	±12.97
Rate ($\times 10^3$)	8.70	± 1.14	± 0.28	13.49	± 4.14	± 1.09
	Slow Rescaling Corrected Rate ($\times 10^3$)					
$m_c = 1.3$	10.79	± 1.41	± 0.34	18.97	± 5.82	± 1.54
$m_c = 1.5$	11.08	± 1.46	± 0.35	19.57	± 6.00	± 1.58
$m_c = 1.7$	11.42	± 1.50	± 0.36	20.27	± 6.22	± 1.64
$m_c = 1.9$	11.80	± 1.55	± 0.37	21.09	± 6.47	± 1.70

6.2.3 One parameter fits: κ

The fits reported in this subsection use only the dimuon distributions $E_{\nu-vis}$ and x in the χ^2 calculation. The fits were performed with the branching fraction fixed at the MC value 0.0930, while the dependence on m_c was investigated by performing the fit for range of the charm quark masses. The results are presented in Table 6.4. The χ^2 for the LO HMRS (MT-LO-DIS) fits ranges from 19.14 to 20.44 (19.47 to 20.70) with 23 degrees of freedom. The fits were performed for the two previously discussed PDFs in the lowest order cross-section. They were also run, re-weighting the events according to the next-to-leading order cross-section described in Section B.2. Again, the kinematics of the event were left unchanged as parameters and cross-section formalisms were modified and only the overall event weight adjusted.

The same table demonstrates the remnant dependence on the underlying PDF used in extracting κ. Some of the overall shift when changing from the HMRS PDFs to the MT-LO-DIS PDFs can be attributed to the differences in the down quark distributions (see Figure 6.1). It should thus be apparent that any determination of κ is sensitive to the separation of $d(x, Q^2)$ from $s(x, Q^2)$. Had the data been dominated by antineutrino dimuon events this separation would be far less important.

Table 6.4: One parameter fits: κ

The branching fraction is fixed at the MC value of .0930 and the fits are performed for a variety of charm quark masses.

m_c	Leading Order		NLO Cross Section		
(GeV/c^2)	HMRS	MT-LO-DIS	HMRS	MT-S1M	MT-S2M
1.3	$0.512 \, ^{+0.066}_{-0.064}$	$0.749 \, ^{+0.096}_{-0.096}$	$0.637 \, ^{+0.080}_{-0.077}$	$0.911 \, ^{+0.113}_{-0.110}$	$0.833 \, ^{+0.104}_{-0.100}$
1.4	$0.523 \, ^{+0.067}_{-0.065}$	$0.766 \, ^{+0.101}_{-0.098}$	$0.652 \, ^{+0.082}_{-0.079}$	$0.933 \, ^{+0.116}_{-0.112}$	$0.857 \, ^{+0.107}_{-0.103}$
1.5	$0.534 \, ^{+0.068}_{-0.066}$	$0.785 \, ^{+0.103}_{-0.100}$	$0.666 \, ^{+0.083}_{-0.080}$	$0.957 \, ^{+0.118}_{-0.114}$	$0.882 \, ^{+0.110}_{-0.106}$
1.6	$0.547 \, ^{+0.070}_{-0.068}$	$0.804 \, ^{+0.105}_{-0.102}$	$0.684 \, ^{+0.085}_{-0.082}$	$0.982 \, ^{+0.121}_{-0.117}$	$0.908 \, ^{+0.113}_{-0.109}$
1.7	$0.560 \, ^{+0.071}_{-0.069}$	$0.825 \, ^{+0.108}_{-0.104}$	$0.703 \, ^{+0.087}_{-0.084}$	$1.008 \, ^{+0.124}_{-0.120}$	$0.937 \, ^{+0.116}_{-0.112}$
1.8	$0.575 \, ^{+0.073}_{-0.070}$	$0.848 \, ^{+0.110}_{-0.107}$	$0.722 \, ^{+0.090}_{-0.086}$	$1.037 \, ^{+0.127}_{-0.123}$	$0.967 \, ^{+0.119}_{-0.115}$
1.9	$0.591 \, ^{+0.074}_{-0.072}$	$0.872 \, ^{+0.113}_{-0.110}$	$0.742 \, ^{+0.092}_{-0.089}$	$1.067 \, ^{+0.130}_{-0.126}$	$0.999 \, ^{+0.123}_{-0.118}$

6.2.4 Two parameter fits: κ and Branching Ratio

The two parameters κ and Br_c are expected to be strongly negatively correlated. The fits reported in this subsection again use only the dimuon distributions $E_{\nu-vis}$ and x in the χ^2 calculation. The dependence of these two-parameter fits on m_c is

investigated in Table 6.5 as the charm quark mass is varied from 1.3 to 1.9 GeV. The χ^2 for the HMRS (MT-LO-DIS) fits ranges from 19.12 to 20.31 (19.47 to 20.67) with 22 degrees of freedom.

The quoted errors on the fit values correspond to the extrema of the one χ^2 deviation hypercontour from the minima, taking into account the correlations with all the other parameters. Thus the errors express only the uncertainty in that parameter. The extent of the uncertainties can be seen in Figures 6.2 and 6.3. The departure from a linear correlation between κ and the branching fraction is similarly obvious. This distortion is due to the constraint imposed by the presence of the down quark contributions in the neutrino sample but not the antineutrino sample.

6.2.5   Three Parameter Fits

In this section, the fits were allowed to vary three parameters: κ, Br_c, and m_c. The charged current E_ν distribution was included in the χ^2 calculation to provide an additional handle on m_c as a result of the threshold behaviour   of all charm producing events[1]. The results of these fits are tabulated in Table 6.6. There were 89 degrees of freedom in the problem. Most of the χ^2 comes from discrepancies in the charged current E_ν distribution.

---

[1] Event cross-section weights were pre-calculated for 0.1 GeV steps in m_c between 1.0 and 2.0 GeV. In the process of fitting it was sometimes necessary for MINUIT to go beyond this range in order to determine the χ^2 contour slope. Such extrapolations could have be problematic, but experience showed that the fits converged to reasonable values. This did have the side effect of occasionally act as a catalyst for reporting a failure to correctly calculate the errors on one or more parameters. Generally this failure is attributable to the matrix of second derivatives, including correlations, not being positive definite.

Table 6.5: Two parameter fits: κ and Br_c

m_c (GeV)	Leading Order			
	HMRS PDF		MT-LO-DIS PDF	
	κ	Br_c	κ	Br_c
1.3	$.478^{+.363}_{-.191}$	$.0968^{+.0286}_{-.0281}$	$.758^{+.549}_{-.295}$	$.0924^{+.0263}_{-.0258}$
1.4	$.480^{+.364}_{-.192}$	$.0976^{+.0289}_{-.0284}$	$.764^{+.555}_{-.299}$	$.0932^{+.0266}_{-.0261}$
1.5	$.482^{+.366}_{-.193}$	$.0988^{+.0292}_{-.0287}$	$.771^{+.561}_{-.302}$	$.0940^{+.0269}_{-.0264}$
1.6	$.484^{+.368}_{-.194}$	$.0999^{+.0296}_{-.0290}$	$.777^{+.567}_{-.305}$	$.0949^{+.0272}_{-.0267}$
1.7	$.487^{+.369}_{-.196}$	$.1011^{+.0299}_{-.0293}$	$.783^{+.572}_{-.308}$	$.0959^{+.0276}_{-.0270}$
1.8	$.489^{+.371}_{-.197}$	$.1024^{+.0303}_{-.0297}$	$.788^{+.577}_{-.311}$	$.0970^{+.0279}_{-.0274}$
1.9	$.491^{+.372}_{-.198}$	$.1038^{+.0307}_{-.0301}$	$.794^{+.582}_{-.314}$	$.0983^{+.0283}_{-.0278}$

| m_c (GeV)	Next-to-Leading Order					
	HMRS		MT-S1M		MT-S2M	
	κ	Br_c	κ	Br_c	κ	Br_c
1.3	$.753^{+.568}_{-.283}$	$.0839^{+.0259}_{-.0255}$	$1.116^{+.906}_{-.431}$	$.0820^{+.0266}_{-.0262}$	$.921^{+.702}_{-.349}$	$.0874^{+.0270}_{-.0266}$
1.4	$.776^{+.594}_{-.292}$	$.0835^{+.0261}_{-.0257}$	$1.129^{+.918}_{-.436}$	$.0826^{+.0269}_{-.0265}$	$.938^{+.718}_{-.356}$	$.0879^{+.0273}_{-.0269}$
1.5	$.785^{+.597}_{-.296}$	$.0840^{+.0262}_{-.0258}$	$1.142^{+.928}_{-.441}$	$.0833^{+.0272}_{-.0268}$	$.954^{+.732}_{-.363}$	$.0886^{+.0276}_{-.0272}$
1.6	$.792^{+.600}_{-.298}$	$.0849^{+.0264}_{-.0260}$	$1.153^{+.937}_{-.446}$	$.0841^{+.0274}_{-.0270}$	$.970^{+.745}_{-.370}$	$.0893^{+.0279}_{-.0275}$
1.7	$.798^{+.602}_{-.300}$	$.0859^{+.0267}_{-.0263}$	$1.165^{+.946}_{-.451}$	$.0850^{+.0278}_{-.0274}$	$.986^{+.760}_{-.376}$	$.0901^{+.0283}_{-.0279}$
1.8	$.805^{+.605}_{-.303}$	$.0870^{+.0270}_{-.0266}$	$1.176^{+.955}_{-.456}$	$.0860^{+.0281}_{-.0277}$	$1.001^{+.773}_{-.383}$	$.0910^{+.0286}_{-.0283}$
1.9	$.808^{+.604}_{-.304}$	$.0882^{+.0274}_{-.0269}$	$1.187^{+.962}_{-.460}$	$.0870^{+.0285}_{-.0281}$	$1.017^{+.787}_{-.390}$	$.0920^{+.0291}_{-.0287}$
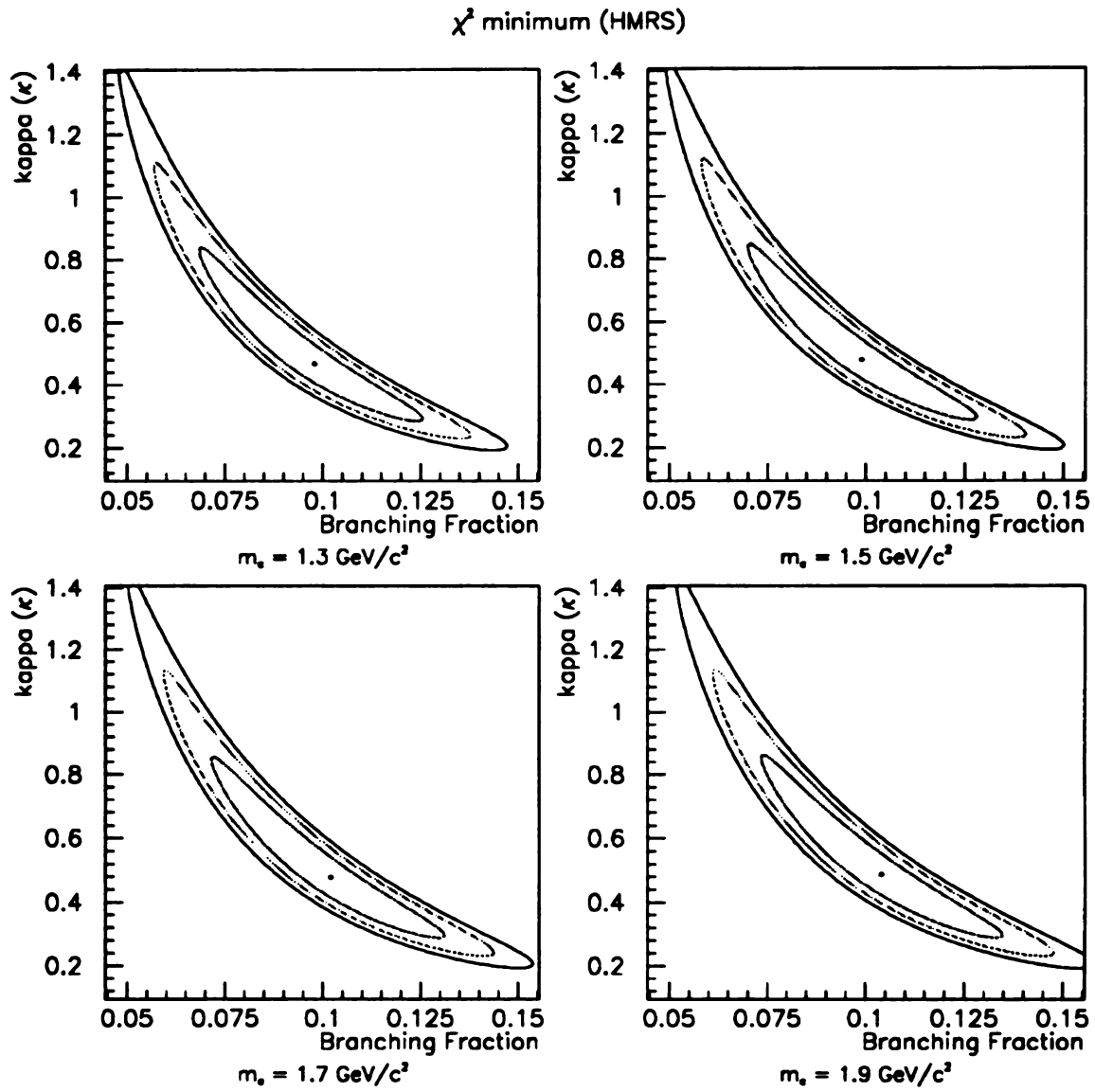
Figure 6.2: Two parameter χ^2 contours (HMRS)
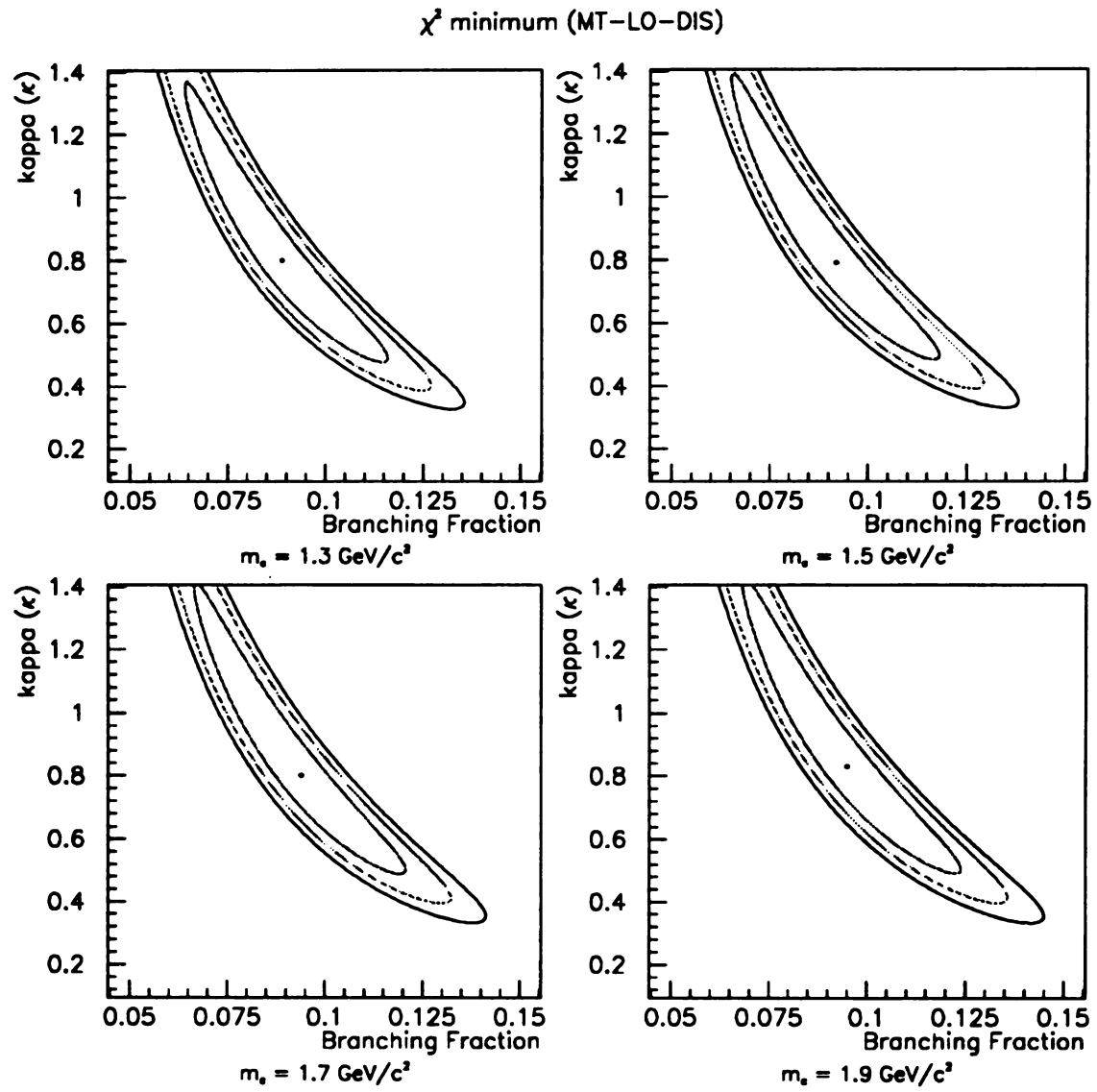
Figure 6.3: Two parameter χ^2 contours (MT-LO-DIS)

Table 6.6: Three Parameter Fits

PDF		κ		Br_c		m_c		χ^2
HMRS	LO	0.797	$^{+0.157}_{-0.147}$	.0776	$^{+.0124}_{-.0100}$	1.811	$^{+.314}_{-.296}$	150.52
MTLO	LO	0.881	$^{+0.203}_{-0.184}$	.0943	$^{+.0150}_{-.0121}$	1.944	$^{+.410}_{-.389}$	154.56
HMRS	NLO	0.745	$^{+0.165}_{-0.145}$	.0919	$^{+.0131}_{-.0129}$	1.802	$^{+.338}_{-.338}$	134.92
MT-S1M NLO		0.907	$^{+0.221}_{-0.179}$	.1032	$^{+.0193}_{-.0122}$	1.940	$^{+.252}_{-.580}$	159.20
MT-S2M NLO		0.930	$^{+0.210}_{-0.182}$	.1017	$^{+.0173}_{-.0135}$	2.080	$^{+.512}_{-.372}$	154.38

Fit Quality

The sensitivity of the fits to the overall decay background scale can be seen in Table 6.7. The relative insensitivity of the final values to this scale is encouraging. The extreme stability of the minima of the fits is demonstrated in Table 6.8 for large variations in the starting values. This provides confidence that MINUIT is not being fooled and is indeed finding the global minimum. Table 6.9 explores the sensitivities to the single adjustable parameter in the Peterson fragmentation function. The χ^2 values suggest a slightly lower value for ϵ but certainly do not rule out the chosen value of .19, nor are the values of κ, Br_c, or m_c particularly sensitive to this choice.

6.3 Conclusions

This thesis has described the analysis of neutrino and antineutrino events recorded during the 1985 and 1987 fixed target runs at Fermilab using the FMMF (Lab

Table 6.7: Scan Overall Decay Background Scale (HMRS,LO)

Scale	κ		Br_c		m_c		χ^2
0.00	.736	$\pm$.148	.0997	$\pm$.0140	1.846	$\pm$.326	150.8
0.25	.753	$\pm$.150	.0937	$\pm$.0132	1.840	$\pm$.322	150.5
0.50	.770	$\pm$.152	.0882	$\pm$.0127	1.835	$\pm$.319	150.3
0.75	.784	$\pm$.152	.0829	$\pm$.0119	1.831	$\pm$.316	150.4
nominal	.798	$\pm$.152	.0778	$\pm$.0111	1.828	$\pm$.314	150.5
1.25	.811	$\pm$.149	.0729	$\pm$.0102	1.825	$\pm$.312	150.9
1.50	.823	$\pm$.152	.0682	$\pm$.0094	1.823	$\pm$.310	151.4
1.75	.834	$\pm$.152	.0638	$\pm$.0089	1.822	$\pm$.308	152.1
2.00	.843	$\pm$.143	.0594	$\pm$.0084	1.820	$\pm$.301	153.0

C) detector. These events have been analysed with an emphasis on multi-muon events. A background due to hadron decay in the showers has been subtracted. A comparison between the kinematics of the data events and the computer simulated events can be found in Appendix B.2. The standard model of opposite-sign dimuon production involves the creation of a charm quark, its subsequent fragmentation into a charmed hadron, and the semileptonic decay of the hadron. The experimentally observable properties of the events are in good agreement with the predictions of the model. A number of parameters of the model are extracted under a variety of different constraints. In closing, a comparison of these results is made to those of other similar experiments.

For overall rates, it is only sensible to compare to same experiments exposed to the (anti)neutrino flux spectrum. This follows from the observation that, even after accounting for slow rescaling behaviour, a threshold due to fast rescaling re-

Table 6.8: Fit Stability

The stability of the fits is explored by using different starting points for leading-order HMRS three parameter fits.

Starting Value			Fit Result		
κ	Br_c	m_c	κ	Br_c	m_c
0.52	.09303	1.5	.797	.0776	1.81
0.1	.03	1.0	.798	.0777	1.82
0.1	.03	2.5	.798	.0777	1.82
0.1	.15	1.0	.798	.0777	1.82
0.1	.15	2.5	.797	.0776	1.81
1.5	.03	1.0	.797	.0776	1.81
1.5	.03	2.5	.797	.0776	1.81
1.5	.15	1.0	.797	.0776	1.81
1.5	.15	2.5	.798	.0777	1.82

Table 6.9: Effects of Peterson parameter (ϵ)

The dependence on ϵ is explored for the case of LO HRMS three parameter fits.

ϵ	κ		Br_c		m_c		χ^2
0.07	.771	$\pm$.153	.0682	$\pm$.0094	1.523	$^{+.806}_{-.114}$	148.98
0.09	.809	$\pm$.154	.0713	$\pm$.0105	1.851	$\pm$.323	148.29
0.13	.804	$\pm$.154	.0742	$\pm$.0108	1.843	$\pm$.313	149.29
0.19	.797	$\pm$.151	.0776	$\pm$.0110	1.806	$\pm$.280	150.52
2.25	.792	$\pm$.151	.0874	$\pm$.0115	1.798	$\pm$.310	151.52

mains. This modifies the rate at low energies and thus the absolute rate is partially

dependent on the distribution of neutrino energies.

Table 6.10: Event Rate Comparisons

	Neutrino $(\times 10^3)$			Antineutrino $(\times 10^3)$		
	Acceptance Corrected ($m_c = 1.5$)					
This Experiment	8.70	±1.14	±0.28	13.49	±4.14	±1.09
CCFR [66, page 178]	7.09	± 0.23		6.86	± 0.45	
CCFRW [67, page 159]	7.5	± 0.11		8.1	± 0.26	

	Neutrino $(\times 10^3)$			Antineutrino $(\times 10^3)$		
	Slow Rescaling Corrected					
	This Experiment					
$m_c = 1.3$	10.79	±1.41	±0.34	18.97	±5.82	±1.54
$m_c = 1.5$	11.08	±1.46	±0.35	19.57	±6.00	±1.58
$m_c = 1.7$	11.42	±1.50	±0.36	20.27	±6.22	±1.64
$m_c = 1.9$	11.80	±1.55	±0.37	21.09	±6.47	±1.70
	CCFR [66, pages 182–183]					
$m_c = 1.3$	9.1	± 0.3		11.7	± 0.8	
$m_c = 1.5$	9.6	± 0.3		11.7	± 0.8	
$m_c = 1.9$	10.4	± 0.3		13.9	± 0.9	
	CCFRW [67, page 162]					
$m_c = 1.5$	9.8	± 0.15		12.5	± 0.39	

A comparison with the results by other experiments to the various fit parameters

can be found in Figure 6.3. The references are CCFRW 93 [16], FMMF 91 [17],

CCFR 90 [18], CCFR 87 [19], CDHS 82 [20]. The values for CDHS 82 assumed

Br_c = .071 ± .013 and fit for $|V_{cd}|^2$ to obtain a value of .0576 ± .0144 which is

entirely consistent with our input value of .0484. Similarly FMMF 91 assumed

Br_c = .113 ± .015 and obtained a value of .0378 ± .0127$^{+.0099}_{-.0082}$ for $|V_{cd}|^2$, again within

errors of the input value.

The remaining values in the figure were the results of fits involving two or more parameters. The CCFR 90 and CCFRW 93 measurements are not entirely independent, either statistically or systematically. While this 20% of the data used in this measurement constituted part of the FMMF 91 data sample, the full CCFR 90 event sample makes up 46% the CCFRW 93 events. These two CCFR analyses also use a somewhat controversial parameterization of PDFs; while the total F_2 and F_3 structure functions are not necessarily in question, the separation into individual quark distributions is possibly under dispute. As previously shown, the extraction of κ retains a sensitivity to the d-quark distribution. The CCFR(W) fits also include a shape parameter for the strange quark distribution which allows deviations in the shape from the up and down sea contributions. The PDFs used in this analysis start with the different shapes for the strange and non-strange sea and which remained unchanged.

The errors on this measurement for κ remain large enough that, while suggestive of a higher value than previously seen in dimuon data, this does not constitute a definitive measurement. For the most part the discrepancy between the dimuon measurements of κ and those of the global structure function analyses remains unresolved[2].

---

[2]A suggestion for a third check on κ has been made by Baur, *et al.*[68] to look for charm production at the Tevatron collider. The overall rate of $sg \rightarrow W^- c$ as a fraction of the inclusive $W + 1$ jet cross section provides a measure of the strange quark distribution function. Current limitations on this method stem from the charm tagging efficiency.
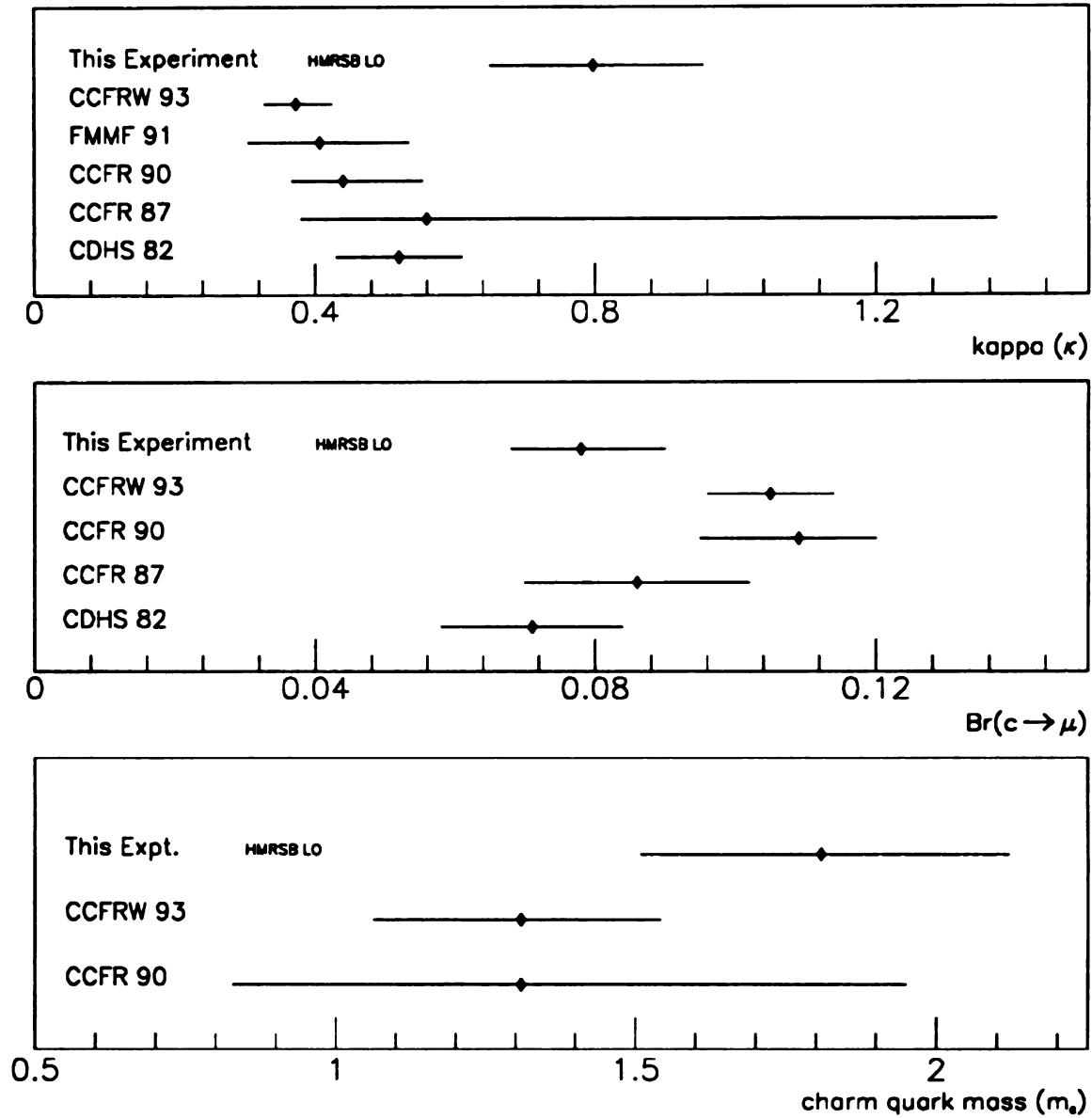
Figure 6.4: Comparison with other large ν detectors

Values for κ, Br_c and m_c with errors are compared to those found in the literature. See text for detailed conditions under which fits were performed.
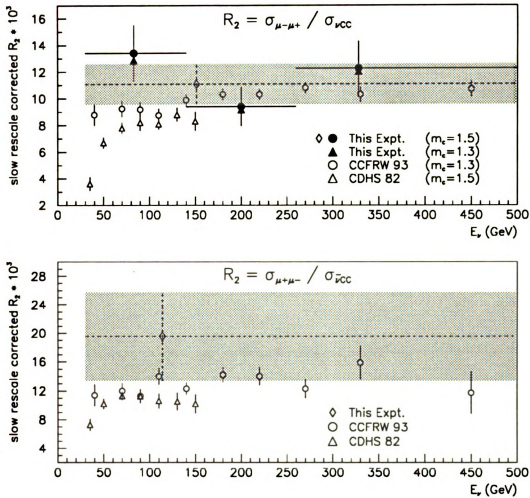
Figure 6.5: Slow-rescaled corrected R_2 and $\overline{R_2}$ vs. E_ν

The broad grey bands (and dotted lines) represent the corrected values for the total E_ν range under the assumption of $m_c = 1.5$ GeV.

APPENDICES

Appendix A

Collaboration List

Fermilab Experiment 733

The FMMF Collaboration

The following physicists worked on Fermilab E733, designing, building, preparing, maintaining, testing, and running the experimental apparatus and beamline devices before and during the 1985 and 1987–88 runs.

Michigan State University, East Lansing, MI

M. Abolins, R. L. Brock, W. G. Cobau, E. Gallas, R. W. Hatcher, B. Johnston,

M. D. Morrow, D. Owen, G. J. Perkins, M. A. Tartaglia, H. Weerts

Fermi National Accelerator Laboratory, Batavia, IL

D. Bogert, S. C. Fuess, G. Koizumi, L. Stutte

Massachusetts Institute of Technology, Cambridge, MA

J. I. Friedman, H. W. Kendall, V. Kistiakowsky, L. S. Osborne, R. E. Pitt,

L. Rosenson, U. Schneekloth, B. Strongin, F. E. Taylor

University of Florida, Gainesville, FL

J. K. Walker, A. White, J. Womersley

Appendix B

Cross Section Formula Enhancements

> *Natural science does not simply describe and explain nature; it is part of the interplay between nature and ourselves; it describes nature as exposed to our method of questioning.*
>
> – Werner Heisenberg

Previously we have described the effects of R_L (Section 1.3.1) and slow rescaling (Section 1.4) on the base cross section of Equation 1.15. In this appendix two further improvements to the cross section are explored. The first deals with the effects of the sudden change of the charge of fermions after the emission or absorption of a $W^{\pm}$ boson. These give rise to electromagnetic radiative effects involving photons.

The second section deals with the replacement of the slow rescale mechanism for dealing with heavy quarks. Additionally, it includes the most important Next-to-Leading-Order (NLO) diagram. The replacement formalism provides a natural means of incorporating the target recoil and longitudinal spin components.
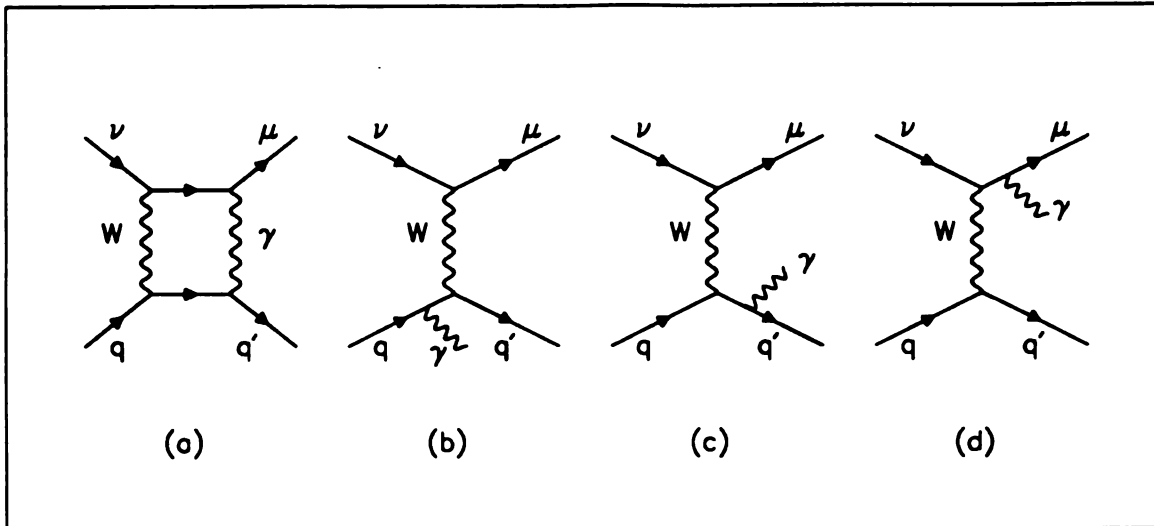
Figure B.1: Radiative correction Feynman diagrams.
(a) box diagram (b) quark initial leg diagram (c) quark final leg and (d) muon leg diagram.

B.1   Radiative Corrections

These corrections to the calculation of the DIS cross section arise from the electrically charged nature of the participants. The acceleration of the charged fermions prior and subsequent to the interaction influence the cross section by introducing the possibility of the emission of an additional photon that changes the energies of the participants. For charged current interactions there are four possible diagrams at the lowest order level of corrections (Figure B.1).

The corrections for all but the muon-leg (Figure B.1(d)) processes are applied as a multiplicative factor modifying the "bare" cross section: $\sigma_{corrected} = K \, \sigma_{bare}$. The correction scales as a function of the momentum transfer to the struck quark, $s_q = 2E_\nu x M + (xM)^2$, but it is only a slowly-varying *log* dependence.

Llewellyn-Smith and Wheater[33, 34, 35], have calculated the box diagram corrections for scattering off d-like (charge $\pm\frac{1}{3}e$) and u-like (charge $\pm\frac{2}{3}e$) quarks to be:

$$K_d = 1 + \frac{\alpha}{\pi}\left\{\left[\ln\frac{M_{W^\pm}^2}{s_q} + \frac{9}{4}\right] - \frac{1}{9}\left[\frac{2}{3}\ln\frac{s_q}{m_d^2} + \frac{1}{6}\left(\pi^2 - \frac{19}{4}\right)\right]\right\}$$

$$K_u = 1 + \frac{\alpha}{\pi}\left\{\left[\ln\frac{M_{W^\pm}^2}{s_q} + \frac{1}{2}\right] - \frac{4}{9}\left[\frac{2}{3}\ln\frac{s_q}{m_u^2} + \frac{1}{6}\left(\pi^2 - \frac{43}{4}\right)\right]\right\}$$

These corrections tend to be an small increase, on the order of $\leq 2\%$, of the cross section over the bare value.

Final state radiation of a photon by the outgoing muon involves distinguishing between "soft" collinear and "real" photons. Without a cutoff any calculation of such a process would be divergent as one included the infinite number of infinitesimally small photons. The muon-leg process was accounted for in the cross section calculation by a leading-log approximation based on work performed by de Rùjula et al.[32]. This is incorporated into the Monte Carlo by generating a energy fraction loss of the muon with the correct spectrum and normalization. The energy is then removed from the muon and a photon, collinear to the muon, is added into the hadron recoil system. In this scheme the total cross section remains same but the effective observed y distribution is shifted to higher values. This decreases the observed $Q_{vis}^2 \simeq 4E_\nu E_\mu \sin^2\left(\frac{\theta_\mu}{2}\right)$ as E_ν and θ_μ remain the same while E_μ decreases. This, along with the increase in the measured E_h, serves to drive the observed x distribution to lower values.

B.2 NLO cross sections

The basic charged current cross section (Equation 1.15), reproduced below, arises out of the Quark-Parton Model (QPM) after a number of simplifying approximations have been made. In general those approximations work reasonably well but are aesthetically distasteful. In other cases the approximations are quite poor and calculations might be off by as much as a factor of two.

$$\frac{d^2\sigma}{dxdy} = \frac{G_F^2(s-M^2)}{2\pi(\hbar c)^4} \times \frac{M_W^4}{(Q^2+M_W^2)^2} \times \tag{B.1}$$
$$\left\{ [1 - y - \frac{M^2 xy}{(s-M^2)}] F_2^{(\bar{\nu})CC} + \frac{y^2}{2} 2x F_1^{(\bar{\nu})CC} \pm (y - \frac{y^2}{2}) x F_3^{(\bar{\nu})CC} \right\}$$

We can improve upon Equation B.2 by starting from first principles, replacing what may be instinctively straightforward with something more elegant, but possibly less intuitive initially. In Section 1.3.3 importance was placed on the spin structure of the interactions. By expanding on this idea one can eliminate many of the egregious approximations. This section is derived and condensed from a much more complete work by Tung, *et al.*[14, 31, 69]. Ignoring some of the kinematic quantities for the moment (lumped in as $\mathcal{S}$), we symbolically start with:

$$\frac{d^2\sigma^\nu}{dxdy} = \mathcal{S} \times L_{\lambda\lambda'} d(\psi)_\sigma^\lambda d(\psi)_{\sigma'}^{\lambda'} W^{\sigma\sigma'} \tag{B.2}$$
$$= \mathcal{S} \times \left[d_{11}^2(\psi) F_L + d_{12}^2(\psi) F_0 + d_{13}^2(\psi) F_R \right]$$
$$= \mathcal{S} \times \left[\left(\frac{1+\cosh\psi}{2}\right)^2 F_L + \frac{\sinh^2\psi}{2} F_0 + \left(\frac{1-\cosh\psi}{2}\right)^2 F_R \right]$$

with the rotation angle[1] given by:

$$\cosh\psi = \frac{E_\nu + E_\mu}{\sqrt{Q^2 + \nu^2}} = \frac{\eta^2 M^2 - Q^2 + 2\eta(s - M^2)}{\eta^2 M^2 + Q^2} \xrightarrow[\text{M} \to 0]{} \frac{2 - y}{y}$$

where η plays the analogue of x when one accounts for the target mass. In the case of anti-neutrinos, the roles of the *helicity structure functions F_R and F_L* are reversed. One should note that we completely recover the original from in the limit $M \to 0$ where the rotation matrices reduce to:

$$\left(\frac{1 + \cosh\psi}{2}\right)^2 \to \frac{1}{y^2} \,, \; \frac{\sinh^2\psi}{2} \to \frac{2(1 - y)}{y^2} \,, \; \left(\frac{1 - \cosh\psi}{2}\right)^2 \to \frac{(1 - y)^2}{y^2} \quad \text{(B.3)}$$

By choosing the helicity formalism we do away the the assumption of zero-mass partons (which leads to the Callan-Gross relation) and the implicit assumption about M in certain parts of the formula. By retaining the assumption of zero-mass neutrinos (and negligible muon mass) the formalism still reduces to only three structure functions when the most general hadronic tensor is contracted with the leptonic tensor. At this point the equations are completely general and assume only small lepton masses and Lorentz kinematics.

The next stage involves the QCD factorization of the measured structure functions into parton distributions that can be used in perturbation theory. The factorization theorem states that the dominant contributions of the hadron tensor structure functions arise from on-shell, collinear partons. This factorizes into the convolution of

---

[1]For space-like q, ψ is actually a hyperbolic angle specifying a Lorentz boost.

finding a parton of momentum fraction ξ with the hard cross section for the exchange boson scattering off that parton, summed over all parton species. The hard cross section factor plays an analogous role to the hadron structure functions.

By retaining the helicity structure it is straightforward to show that the longitudinal structure function cannot be neglected even to leading order. For charm production by neutrinos, neglecting the struck quark mass (d or s), one obtains:

$$\frac{d^2\sigma(\nu \to c)}{dxdy} = \frac{G_F^2}{(1+Q^2/M_W^2)^2}\left[\tilde{d}(\xi,Q)|V_{cd}|^2 + s(\xi,Q)|V_{cs}|^2\right] \qquad \text{(B.4)}$$
$$\frac{yQ^2}{\pi}\left[(\frac{1+\cosh\psi}{2})^2 + \frac{m_c^2}{2Q^2}\frac{\sinh^2\psi}{2}\right]$$

where $\tilde{d}$ accounts for the isoscalar symmetry between protons and neutrons. The cross section for anti-neutrino production of $\bar{c}$ is:

$$\frac{d^2\sigma(\bar{\nu} \to \bar{c})}{dxdy} = \frac{G_F^2}{(1+Q^2/M_W^2)^2}\left[\tilde{d}(\xi,Q)|V_{cd}|^2 + \bar{s}(\xi,Q)|V_{cs}|^2\right] \qquad \text{(B.5)}$$
$$\frac{yQ^2}{\pi}\left[(\frac{1-\cosh\psi}{2})^2 + \frac{m_c^2}{2Q^2}\frac{\sinh^2\psi}{2}\right]$$

The correspondence is more apparent when one realizes that $yQ^2 = 2ME_\nu xy^2$.

At this point, all that has been discussed is the leading-order diagram as shown in Figure B.2(a). A secondary source of charm production can issue from the *gluon-fusion mechanism* [cf. Fig. B.2(b)]. While one might naively expect such a diagram to be suppressed due to its higher-order nature (two vertices), one must also account for the fact that gluons are much more numerous than strange quarks. In much of the available phase space the two contributions are of comparable magnitude. One
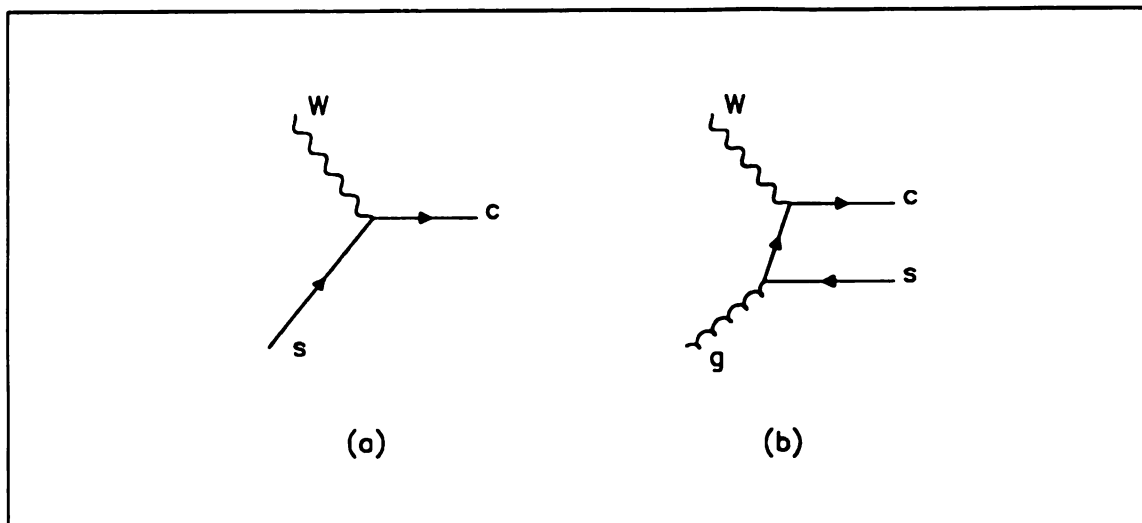
Figure B.2: Charged Current charm producing Feynman diagrams.
(a) leading order quark-W scattering (b) next-to-leading order gluon-W scattering.

must also recognise that the two are not entirely distinct; this is obvious when one ponders where strange quarks come from within an non-strange hadron. It is self-evident that they stem from gluon splitting. As the s-quark line between the two vertices becomes closer to meeting the on-shell (and collinear) criteria the ambiguity becomes more pronounced. Any attempt to incorporate this NLO diagram must also contain a subtraction term that removes the double counting. The details of such a calculations are far too involved to be covered in this thesis. Work done in this regard was made possible by the code generously provided by Wu-Ki Tung, Fred Olness and M.A.G. Aivazis, upon which their paper [31] was based. They show that the effects of NLO and the wrong and longitudinal helicity structure functions tends to suppress the cross section. The NLO cross section can be as little at 50% of the LO cross section in important regions. This would indicate that the present estimates for $s(x, Q)$ are low, and that indeed κ is closer to one than previously believed.

A third diagram enters the picture at the same order as the gluon-fusion process. This is simply the case, similar to the leading diagram, with the modification that a quark line radiates a gluon. One can make a simple order of magnitude estimate to show that this diagram can be neglected. Recall, that the physical cross section is the convolution of the PDF with the parton cross section. For that case of the LO diagram, $f_q(x, Q) \otimes {}^0\hat{\omega}_q$, relative to gluon fusion, $f_G(x, Q) \otimes {}^1\hat{\omega}_G$, one can write:

$$\frac{\sigma_{LO}}{\sigma_{fusion}} \sim \frac{xf_q}{xf_G} \cdot \frac{{}^0\hat{\omega}_q}{{}^1\hat{\omega}_G} \sim \frac{0.05}{0.5} \cdot \frac{1}{\alpha_s(Q)} \sim 1. \tag{B.6}$$

Where ${}^0\hat{\omega}_q$ represents the leading order parton cross section. The NLO cross section is smaller by one order of the strong coupling constant. For the NLO gluon radiation case it should be evident that lacking the substantial enhancement that comes with the gluons, one is left with

$$\frac{\sigma_{LO}}{\sigma_{g\text{-}rad}} \sim \frac{xf_q}{xf_q} \cdot \frac{{}^0\hat{\omega}_q}{{}^1\hat{\omega}_q} \sim \frac{1}{\alpha_s(Q)} \sim 10. \tag{B.7}$$

Thus little harm is done by ignoring this second contribution, at least relative to the disastrous consequences awaiting those that haplessly ignore the gluon fusion case. But it must be emphasized that one also must not blindly calculate the gluon-fusion contribution without due concern for the overlap region were double counting could occur. An overall consistent framework is necessary for dealing with collinear and on-shell conditions.

# Appendix C

Kinematics Comparisons

This appendix contains a compendium of plots demonstrating the physics distributions that one observes in neutrino interactions. A comparison is made with the Monte Carlo. The two are normalized to have an equal number of total charged current interactions after the standard cuts have been applied. In each plot, the data is represented by the points with error bars, while the Monte Carlo is simply an outline. In the case of the distributions representing dimuon events, the estimated background has been subtracted from the data. This background is then plotted as a hashed region.

Figures C.1 through C.6 display present the E_ν, x, y, E_h, Q, and W distributions. Of the four frames in each figure, the left side is devoted to total charged current distributions and the right to dimuons events; the (lower)upper half are (anti-)neutrino induced events. Figures C.7 and C.8 show E_μ and θ_μ for the primary muons of charged currents and dimuons, respectively. Figure C.9 shows the same for the dimuon secondaries. The opening angle between the muons, θ_{12}, and the

relative azimuthal angle, ϕ_{12}, (in the plane perpendicular to the incident neutrino) can be found in Figure C.10. The last two sets of distributions are the measured fragmentation variable z, and the muon asymmetry. Not shown are the muon p_T distributions for the dimuon events; these can be found earlier in Figure 4.11.
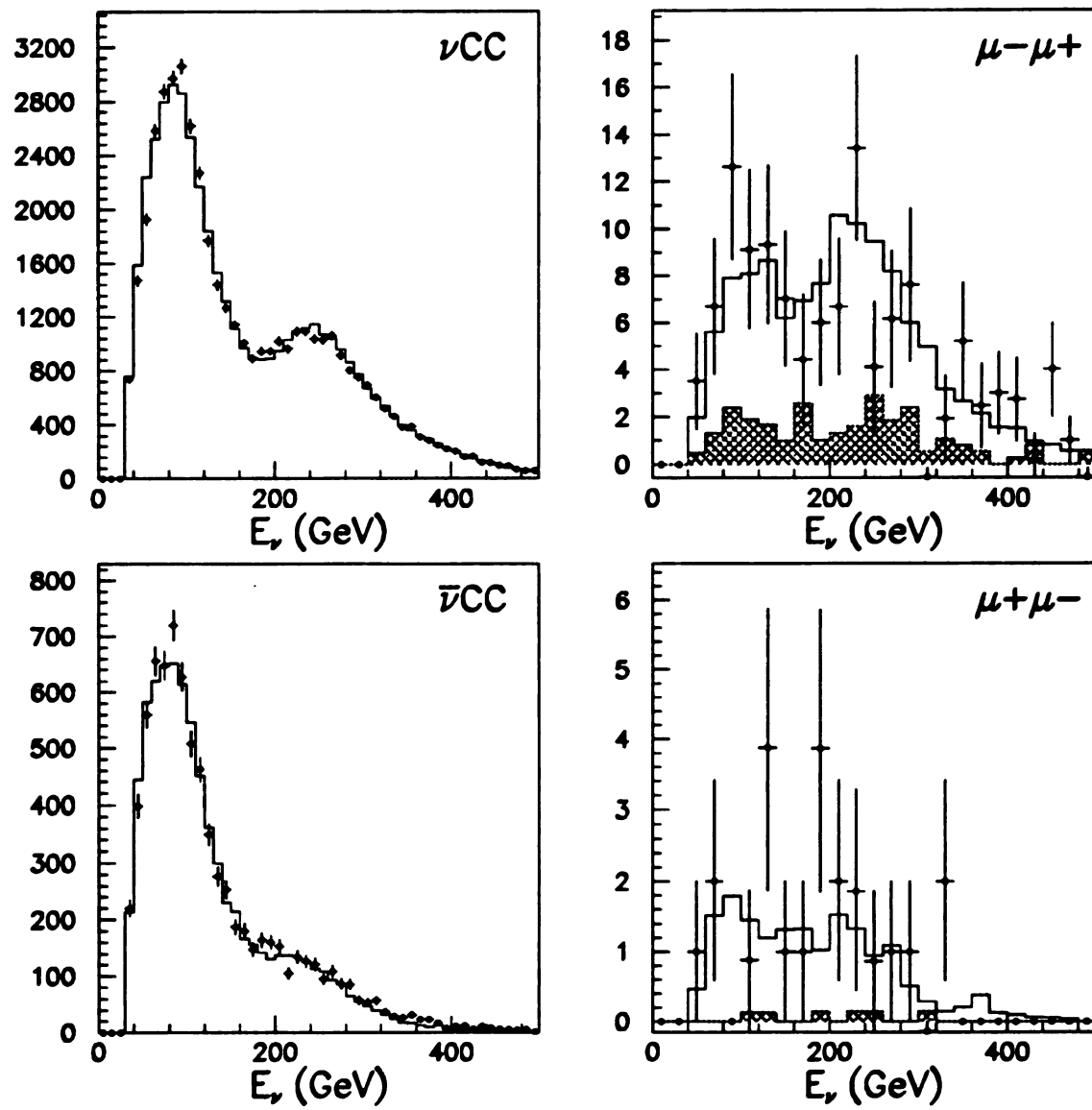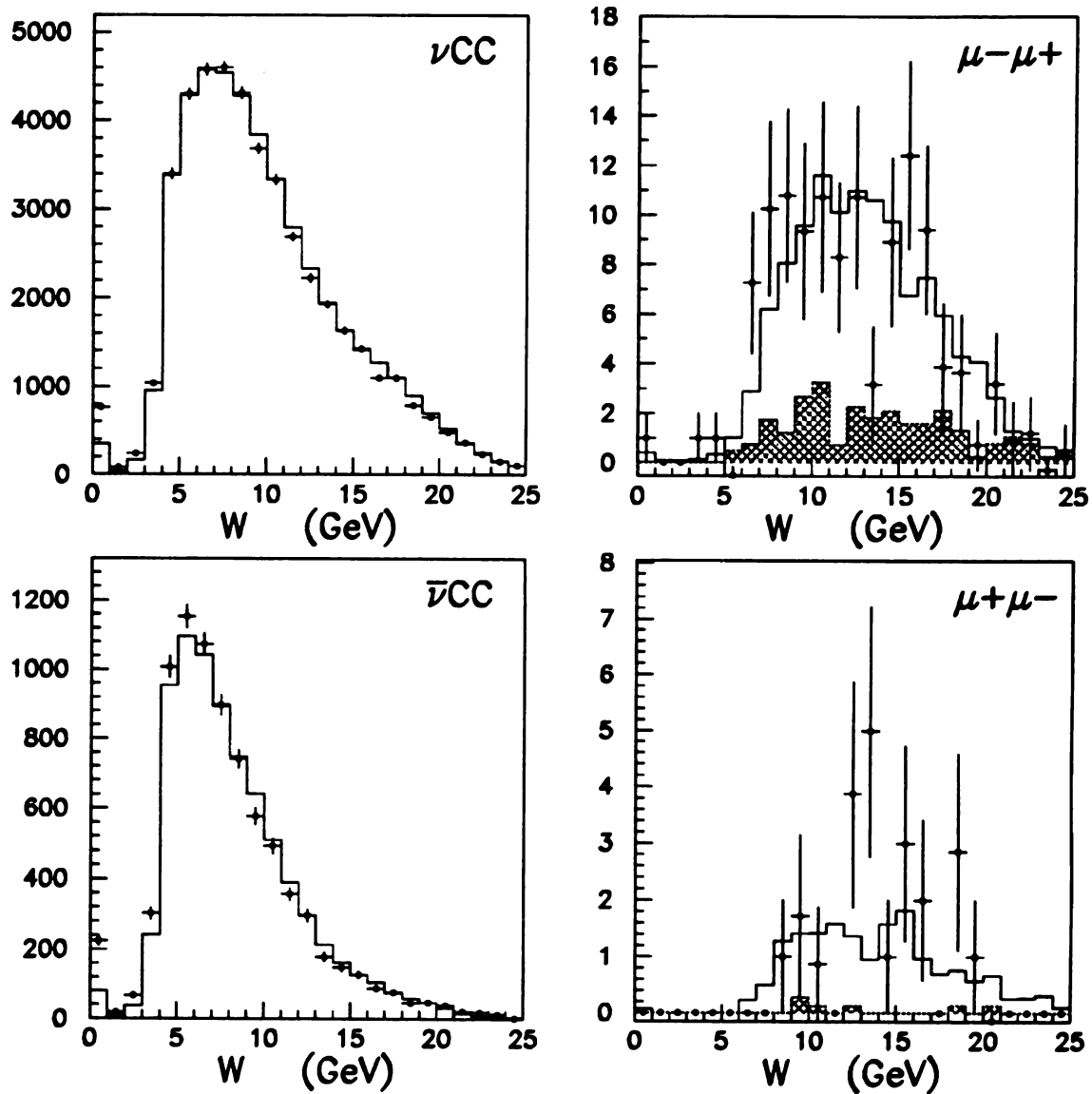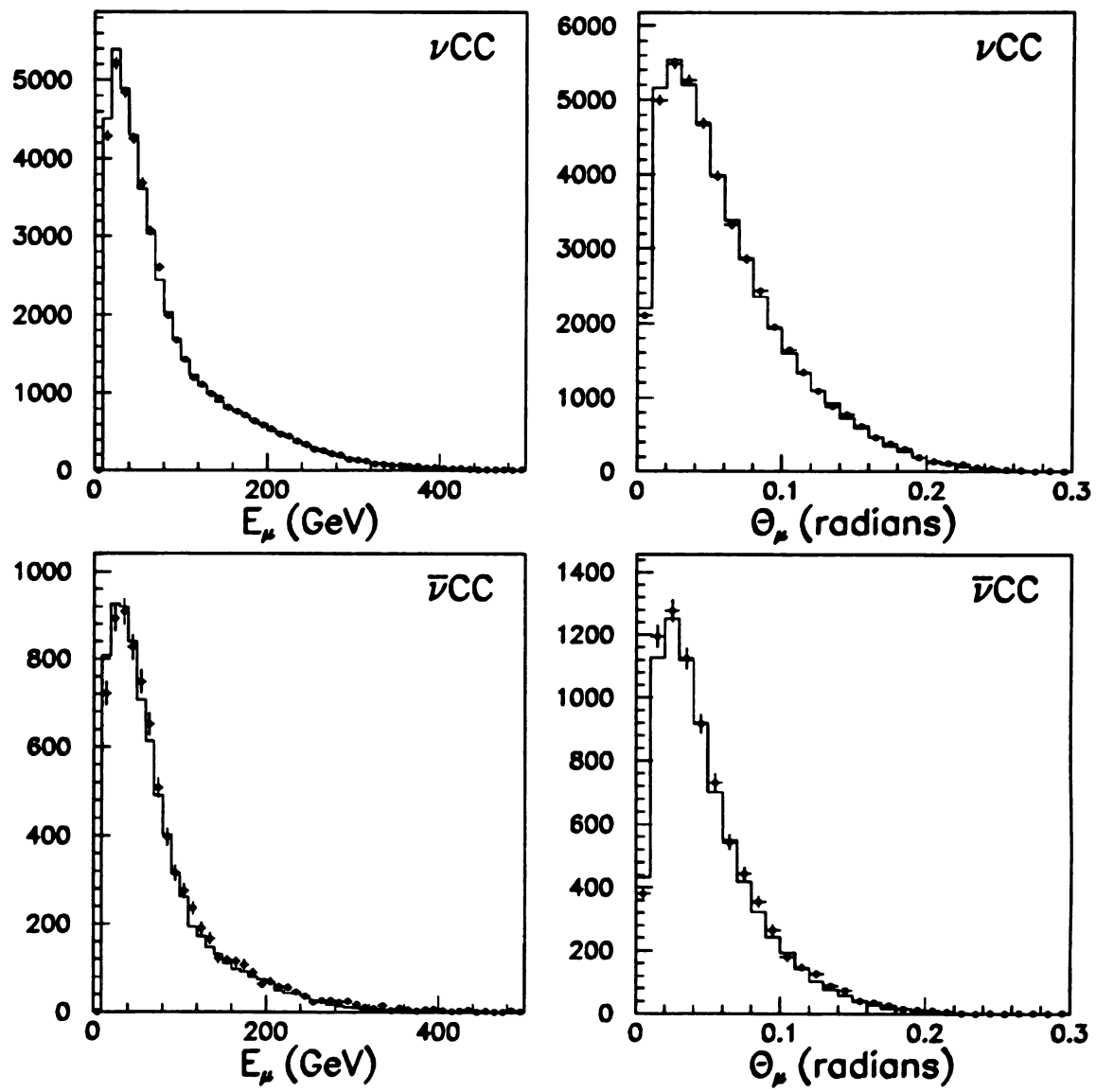
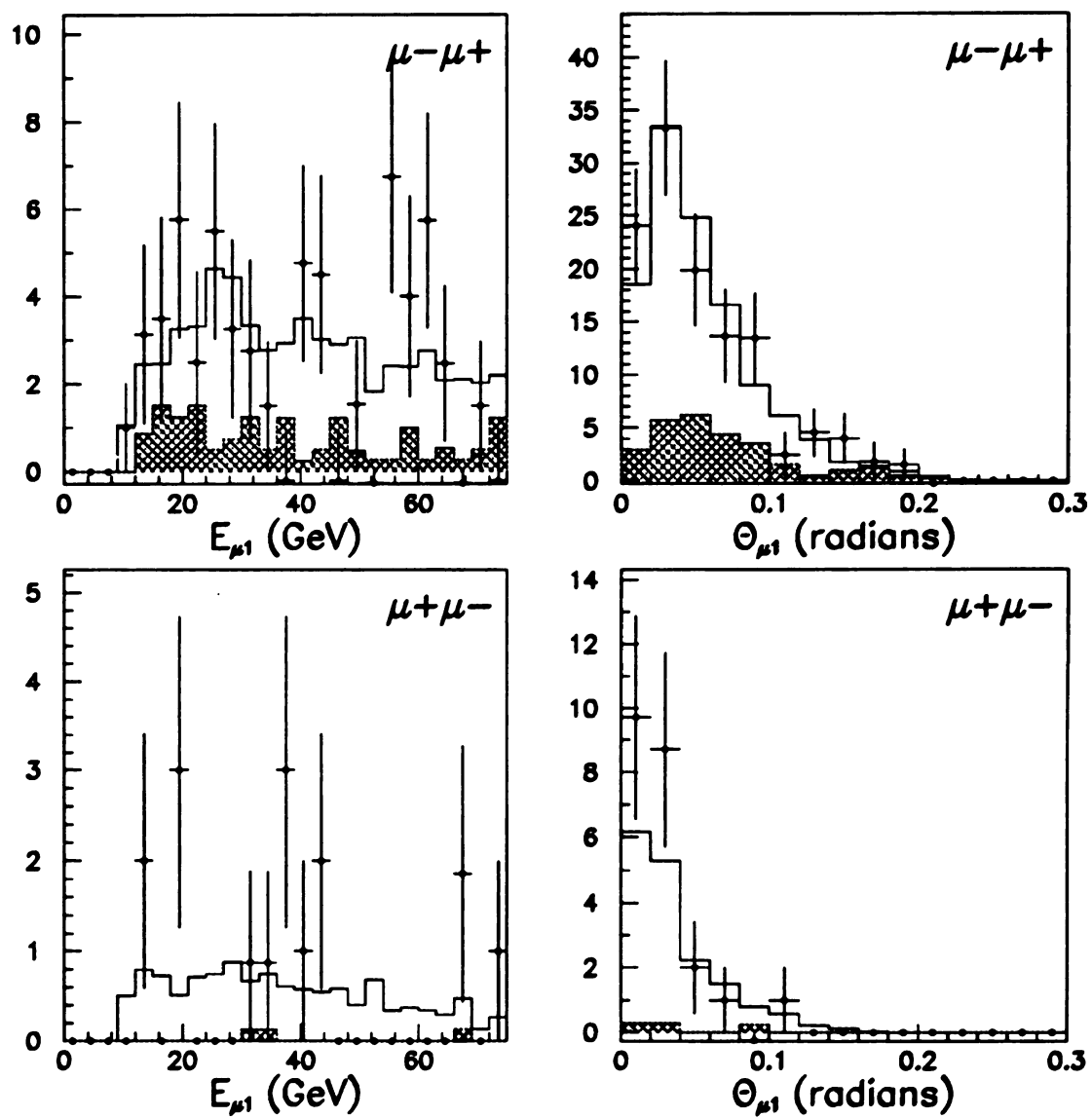Figure C.1: E_ν distributions
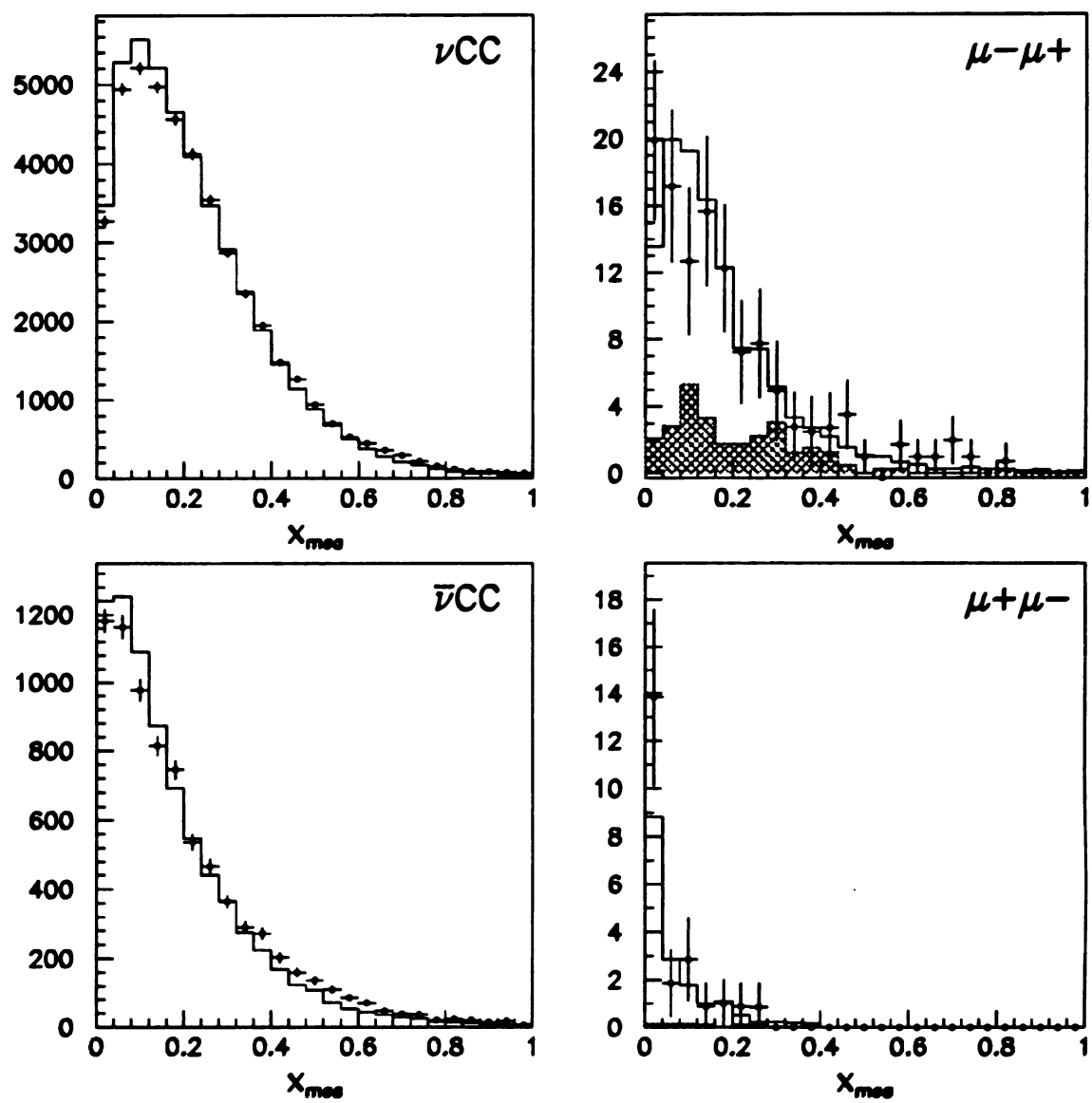
Figure C.2: x distributions
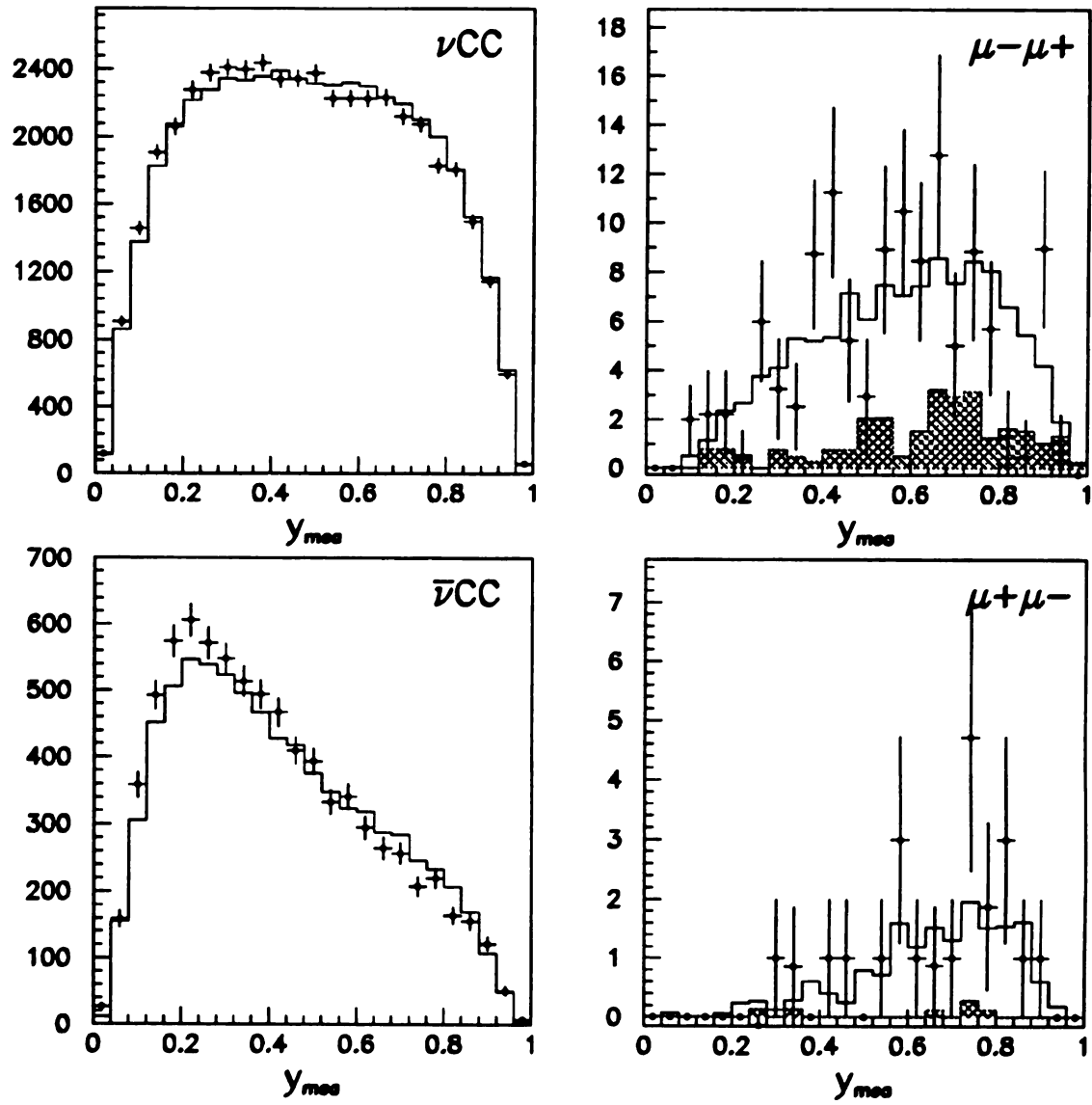
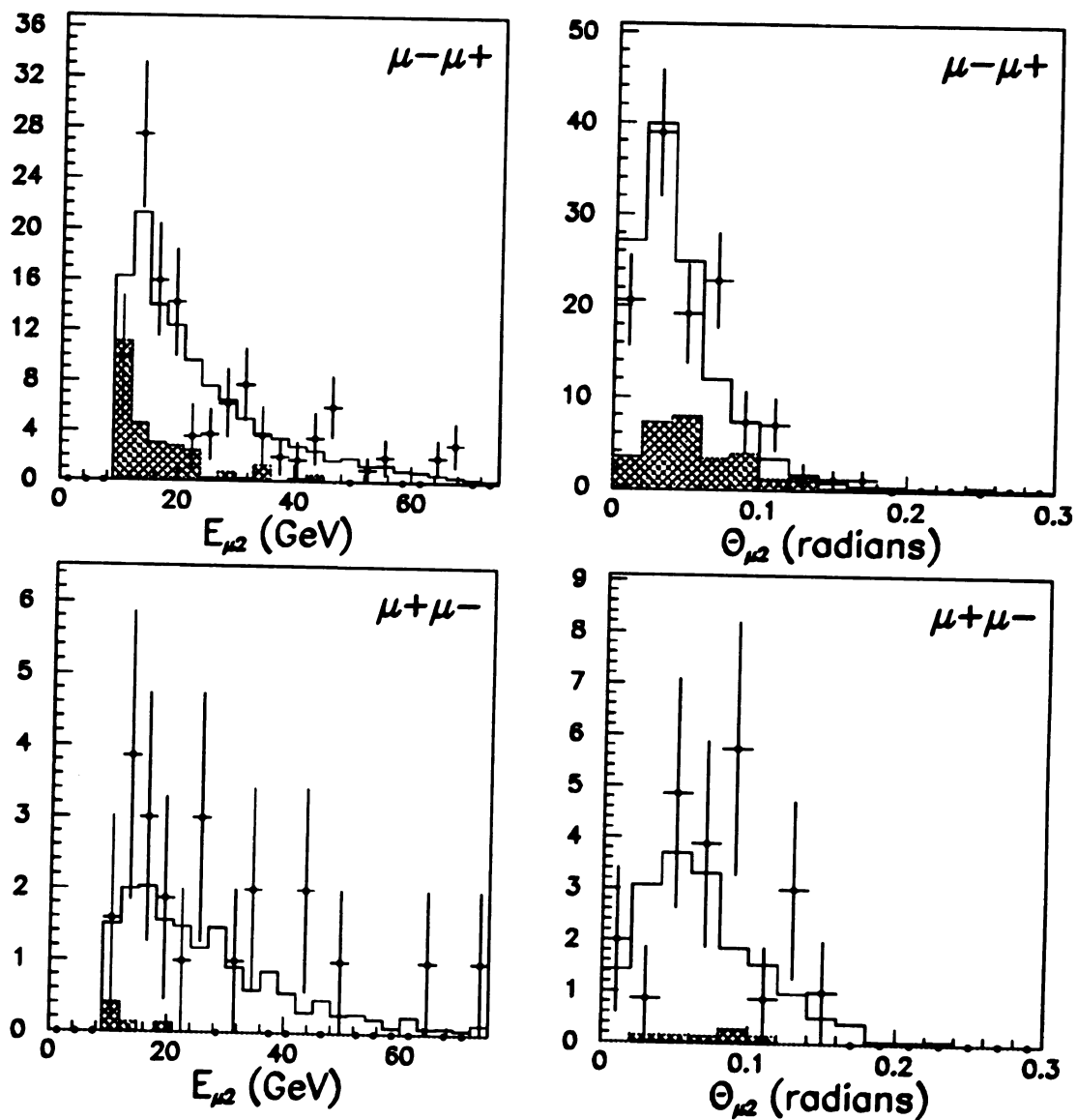Figure C.3: y distributions
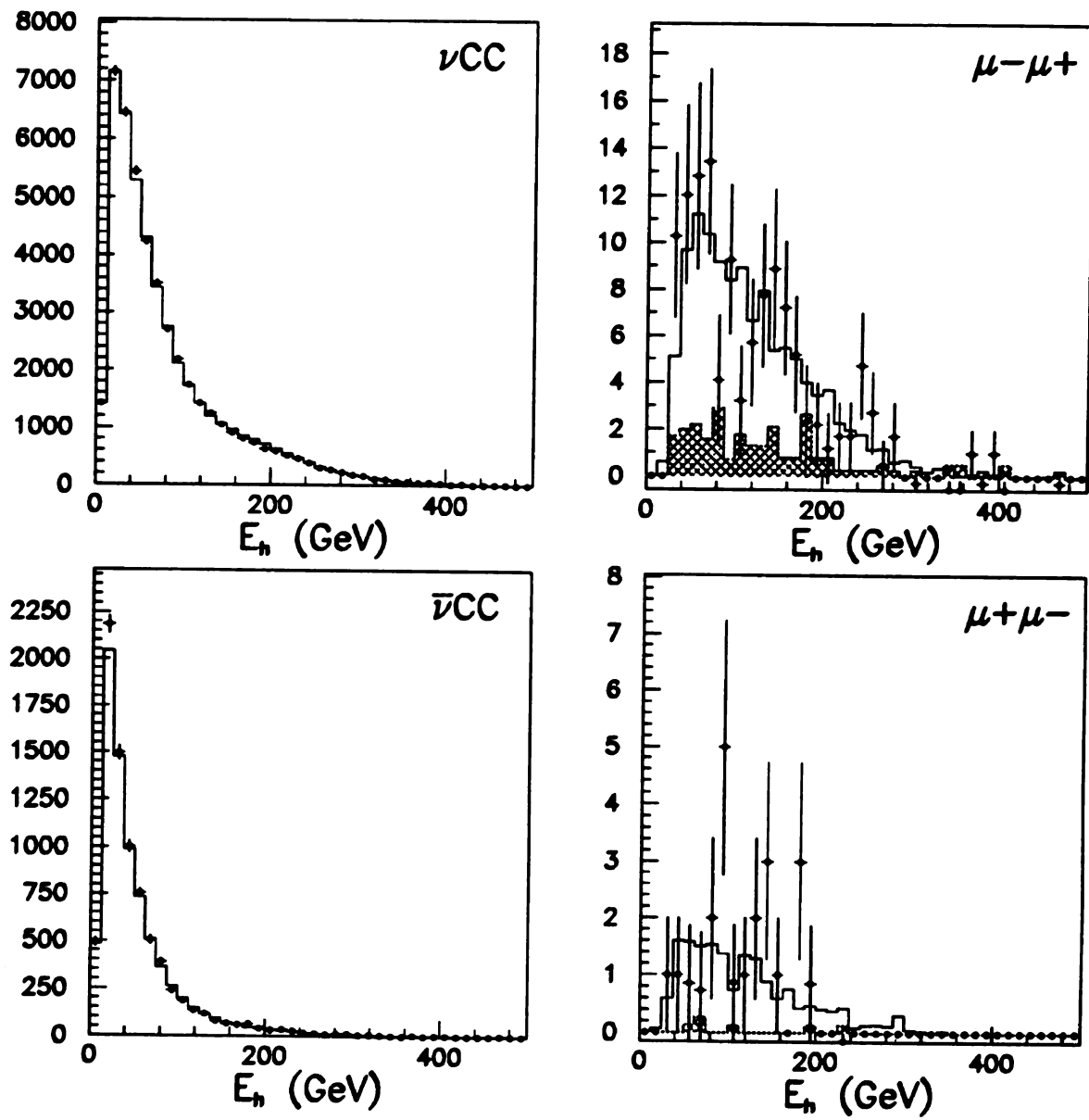
Figure C.4: E_h distributions
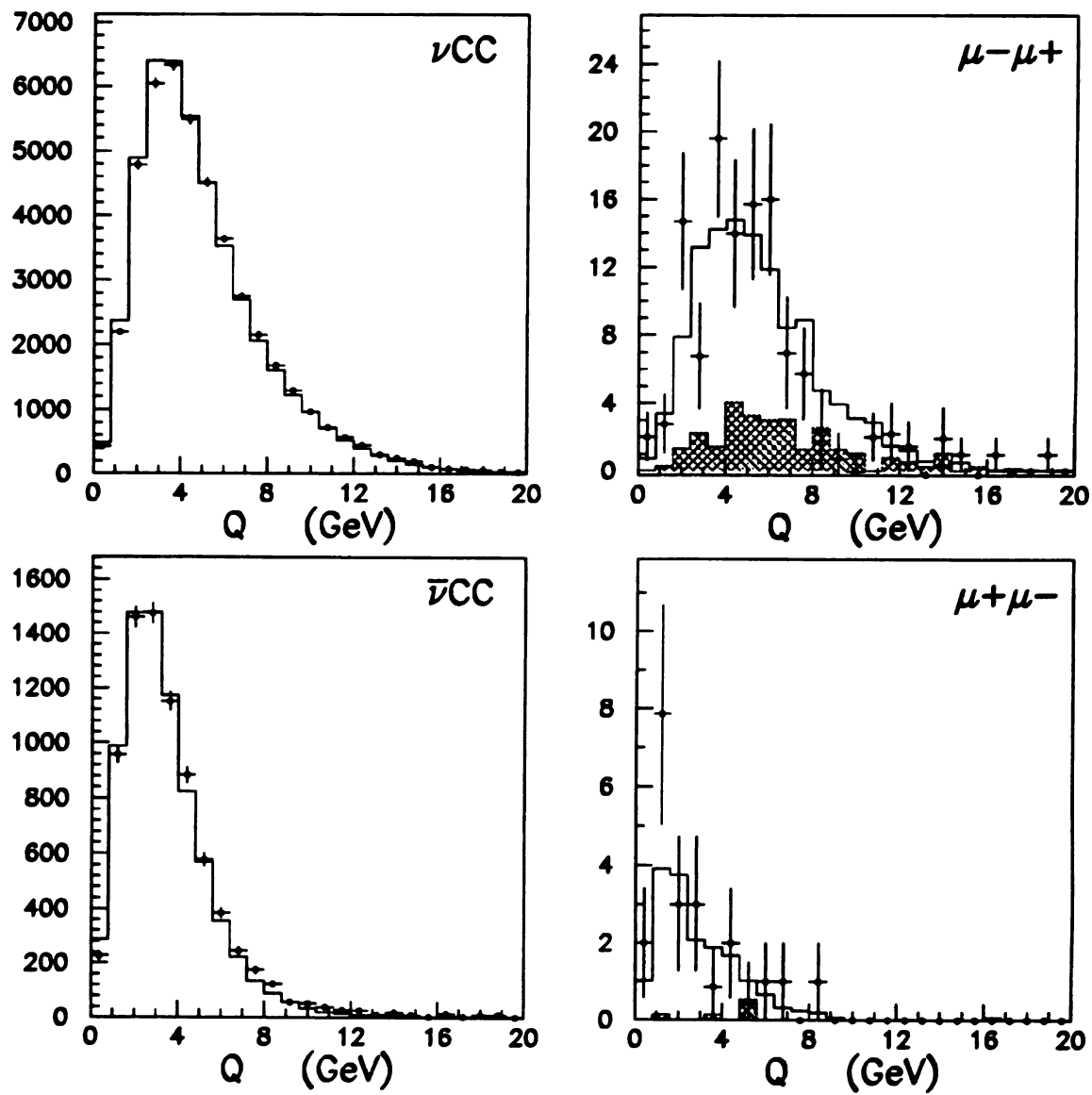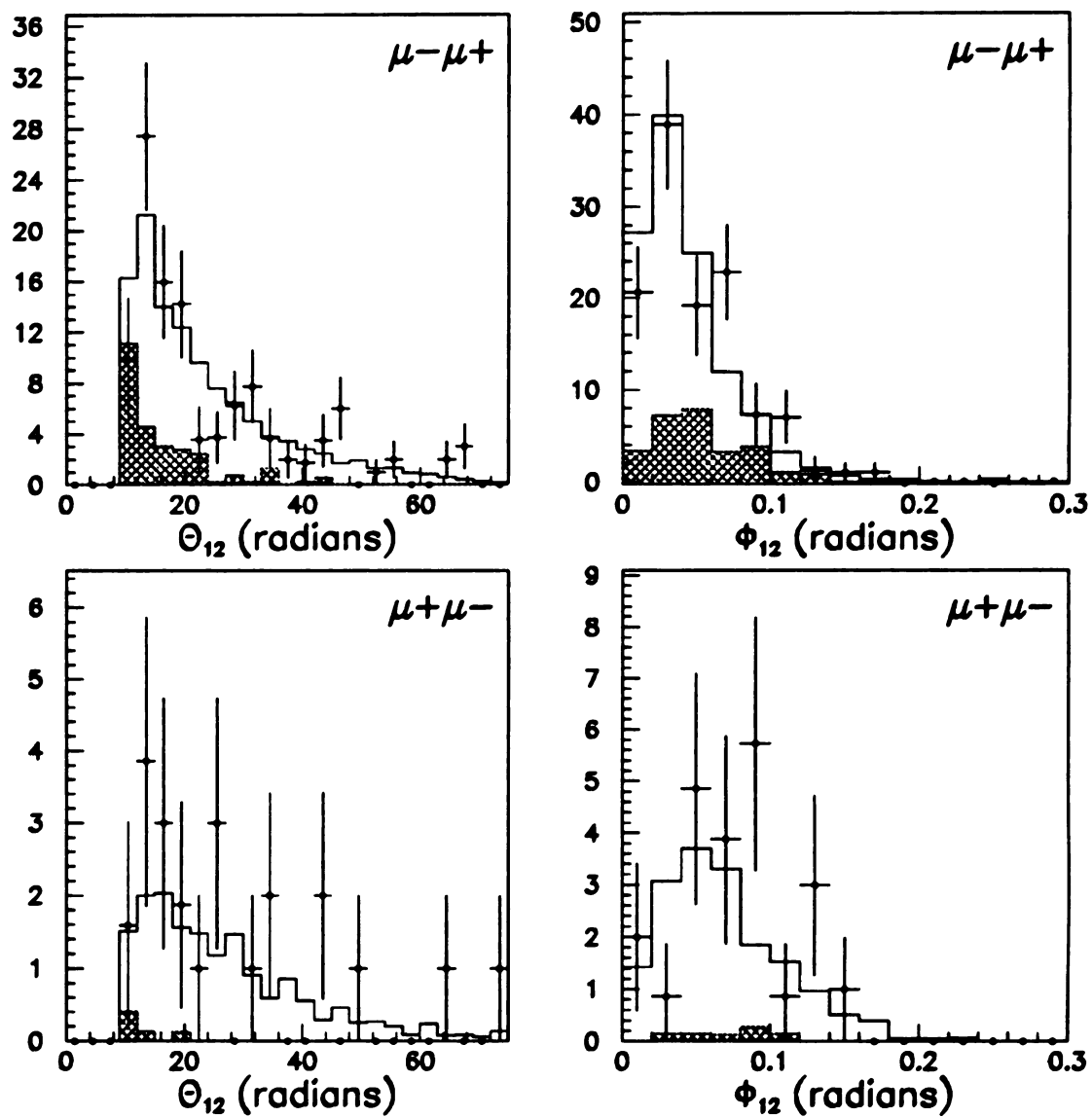
Figure C.5: Q distributions

Figure C.6: *W* distributions

Figure C.7: CC E_μ, θ_μ distributions

Figure C.8: Dimuon $E_{\mu 1}$, $\theta_{\mu 1}$ distributions

Figure C.9: Dimuon $E_{\mu 2}$, $\theta_{\mu 2}$ distributions

Figure C.10: Dimuon angular correlation θ_{12}, ϕ_{12} distributions

28

24

20

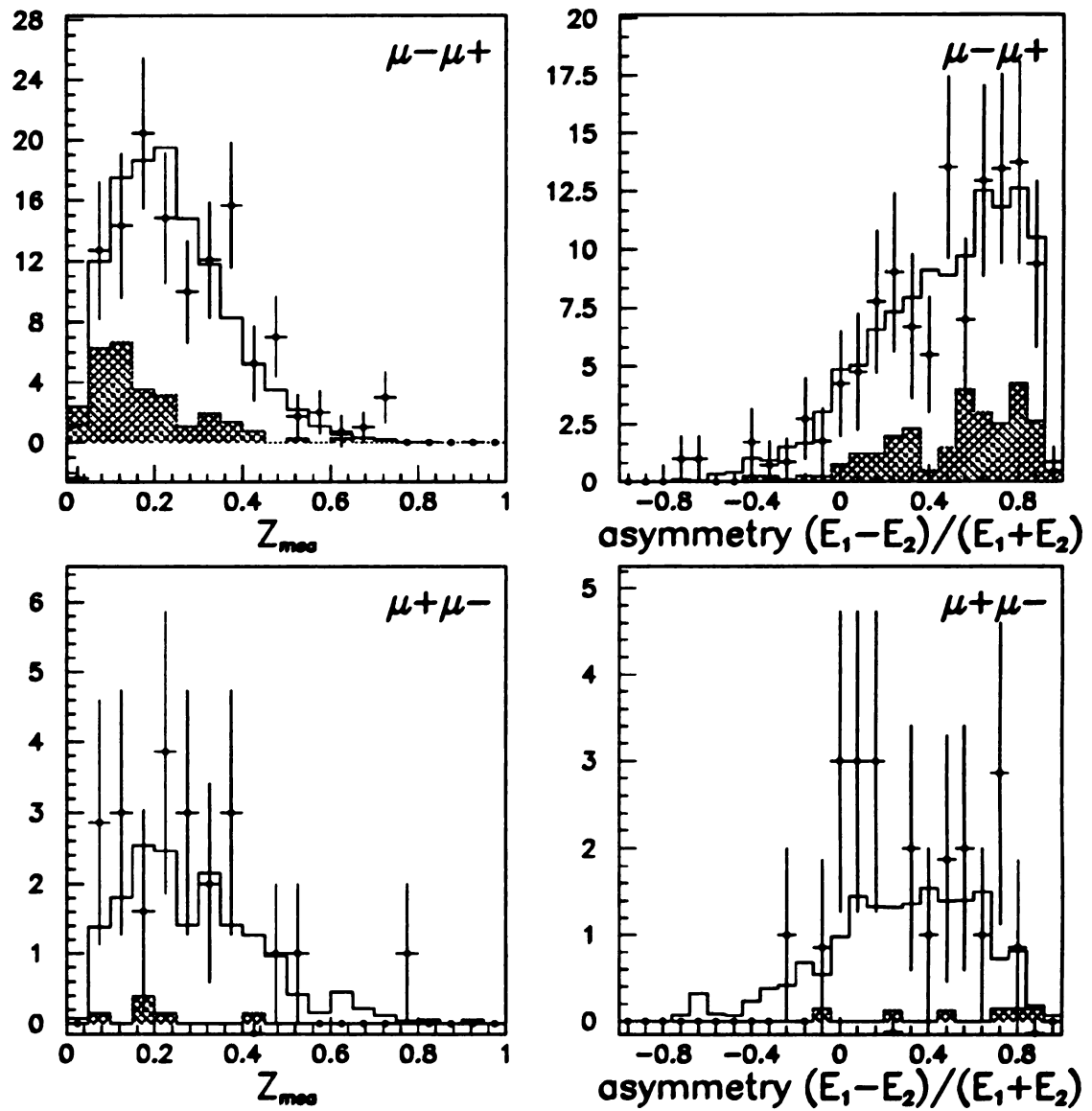16

12

8

4

0

6

5

4

3

2

1

0

Figure C.11: Dimuon z_{mea}, muon E_μ asymmetry distributions

BIBLIOGRAPHY

Bibliography

[1] David J. Griffiths. *Introduction to Elementary Particles*. John Wiley & Sons, Inc., 1987.

[2] Donald H. Perkins. *Introduction to High Energy Physics*. Addison-Wesley Publishing Company, second edition, 1982.

[3] F. E. Close. *An Introduction to Quarks and Partons*. Academic Press, 1979.

[4] Elliot Leader and Enrico Predazzi. *An Introduction to Gauge Theories and the 'New Physics'*. Cambridge University Press, 1982.

[5] Peter Renton. *Electroweak Interactions: an introduction to the physics of quarks and leptons*. Cambridge University Press, 1990.

[6] The Particle Data Group. Review of particle properties. *Phys. Rev. D*, 45 (Part II)(11), 1 June 1992.

[7] G. Altarelli and G. Parisi. Asymptotic freedom in parton language. *Nuc. Phy.*, B(126):229, 1977.

[8] H. Georgi and H.D. Politzer. Freedom at moderate energies: Masses in color dynamics. *Phys. Rev. Lett.*, 36(22):1281–1284, 31 May 1976.

[9] H. Georgi and H.D. Politzer. Freedom at moderate energies: Masses in color dynamics. *Phys. Rev. D.*, 14(7):1829–1848, 1 Oct. 1976.

[10] R. Michael Barnett. Evidence for new quarks and new currents. *Phys. Rev. Lett.*, 36(20):1163–1166, 17 May 1976.

[11] R. Michael Barnett. Evidence in neutrino scattering for right-handed currents associated with heavy quarks. *Phys. Rev. D*, 14(1):70–79, 1 July 1976.

[12] Jean Kaplan and François Martin. Testing quark charged currents in neutrino experiments. *Nuc. Phys.*, 115:333–364, 1976.

[13] Raymond Brock. Dimuon measurements and the strange-quark sea. *Phys. Rev. Lett.*, 44(16):1027–1029, 21 Apr 1980.

[14] M.A.G. Aivazis, Fredrick I. Olness, and Wu-Ki Tung. A unified QCD formulation of charged current and neutral current heavy quark production in deep inelastic scattering. preprint, July 1992. SMU-HEP/92-04; IIT-92/17.

[15] A. de Rùjula, H. Georgi, S.L. Glashow, and H.R. Quinn. Fact and fancy in neutrino physics. *Rev. Mod. Phy.*, 46(2):391–407, Apr. 1974.

[16] S. A. Rabinowitz et al. Measurement of the strange sea distribution using neutrino charm production. *Phys. Rev. Lett.*, 70(2):134–137, 11 Jan 1993.

[17] B. Strongin et al. Study of opposite-sign dimuon production in high-energy neutrino-nucleon interactions. *Phys. Rev. D*, 43(9):2778–2786, 1 May 1991.

[18] C. Foudas et al. Neutrino production of opposite-sign dimuon measurements at Fermilab Tevatron energies. *Phys. Rev. Lett.*, 64(11):1207–1210, 12 Mar 1990.

[19] K. Lang et al. Neutrino production of dimuons. *Z. Phys*, C(33):483–503, 1987.

[20] H. Abramowicz et al. Experimental study of opposite-sign dimuons produced in neutrino and antineutrion interactions. *Z. Phys*, C(15):19–31, 1982.

[21] J. Botts et al. CTEQ parton distributions and flavor dependence of sea quarks. *Phys. Lett.*, 304B:159–166, 1993.

[22] George J. Perkins. *A Measurement of the Ratio of Neutral Current to Charged Current Deep Inelastic ν_μ Scattering Interactions in a Fine Grain Detector at FNAL*. PhD thesis, Michigan State University, East Lansing, MI, 1992.

[23] William Gilbert Cobau. *Nucleon Structure Functions from Deep Inelastic Charged Current Neutrino Scattering*. PhD thesis, Michigan State University, East Lansing, MI, 1992. not yet in print.

[24] Elizabeth J. Gallas. *A Search for Weakly Interacting Massive Particles in the Fermilab Tevatron Wide Band Neutrino Beam*. PhD thesis, Michigan State University, East Lansing, MI, 1993.

[25] A. Benvenuti et al. A large-area magnetic spectrometer for the study of high-energy neutrino interactions. *NIM*, 125:447–456, 1985.

[26] Boris Strongin. *Opposite Sign Dimuon Production in High Energy Neutrino-Nucleon Interactions*. PhD thesis, Massachusetts Institute of Technology, May 1989.

[27] F. James. Monte Carlo theory and practice. *Rep. Prog. Phys.*, 43:1145–1189, 1980.

[28] A.J. Malensek. Empirical formula for thick target particle production. Technical report, FNAL, 12 October 1981. Fermilab Internal Note: FN-341.

[29] H.W. Atherton et al. Precise measurements of particle production by 400 GeV/c protons on beryllium targets. Technical report, CERN, 22 August 1980. CERN Report 80-7.

[30] D.C. Carey, K.L. Brown, and Ch. Iselin. DECAY TURTLE. Technical report, FNAL, March 1982. Fermilab Program Note: PM0031.

[31] M.A.G. Aivazis, Fredrick I. Olness, and Wu-Ki Tung. QCD formulation of charm production in deep-inelastic scattering and the sea-quark-gluon dichotomy. *Phys. Rev. Lett.*, 65(19):2339–2342, 5 Nov. 1990.

[32] A. de Rùjula, R. Petronzio, and A. Savoy-Navarro. Radiative corrections to high-energy neutrino scattering. *Nuc. Phy.*, B(154):394–426, 1979.

[33] C.H. Llewellyn Smith and J.F. Wheater. Electroweak radiative corrections and the value of $\sin^2 \theta_w$. *Phys. Lett.*, 105B(6):486–488, 22 Oct. 1981.

[34] J.F. Wheater and C.H. Llewellyn Smith. Electroweak radiative corrections to neutrino and electron scattering and the value of $\sin^2 \theta_w$. *Nuc. Phys.*, B208:27–76, 1982.

[35] J.F. Wheater and C.H. Llewellyn Smith. Errata: Electroweak radiative corrections to neutrino and electron scattering and the value of $\sin^2 \theta_w$. *Nuc. Phys.*, B226:547, 1983.

[36] P.N. Harriman, A.D. Martin, W.J. Stirling, and R.G. Roberts. Parton distributions extracted from data on deep inelastic scattering, prompt photon production and the drell-yan process. *Phys. Rev. D*, 42(3):798–810, 1 Aug. 1990.

[37] Jorge G. Morfin and Wu-Ki Tung. Parton distributions from a global QCD analysis of deep inelastic scattering and lepton-pair productions. *Z. Phy. C*, 53:13–29, 1991.

[38] C. Peterson, D. Schlatter, I. Schmitt, and P. M. Zerwas. Scaling violations in inclusive e^+e^- annihilation spectra. *Phys. Rev. D*, 27(1):105–111, 1 Jan 1983.

[39] H. Albrecht et al. Production and decay of the charged D^* meson in e^+e^- annihilation at 10 GeV centre-of-mass energy. *Phys. Lett. B*, 150(3):235–241, 3 Jan. 1985.

[40] D. Bortoletto et al. Charm production innonresonant e^+e^- annihilations at $\sqrt{s} = 10.55$ GeV. *Phys. Rev. D*, 37(7):1719–1743, 1 Apr. 1988.

[41] N. Ushida et al. Charmed hadron production by neutrinos. *Phys. Lett.*, 121B(4):292–296, 3 Feb. 1983.

[42] N. Ushida et al. Cross sections for neutrino production of charmed particles. *Phys. Lett. B*, 206(2):375–379, 19 May 1988.

[43] N. Ushida et al. Production characteristics of charmed particles in neutrino interactions. *Phys. Lett. B*, 206(2):380–384, 19 May 1988.

[44] K. Kleinknecht and B. Renk. Charm fragmentation function – a comparison of neutrino and $e + e-$ data. *Z. Phy. C*, 17:325–328, 1983.

[45] Torbjörn Sjöstrand. Status of fragmentation models. preprint/talk, Dept. Theoretical Physics, Univ. of Lund, Sweden, Aug 1986. LU TP 86-16, August 1986; minirapporteur talk in the parallel session on Jets and Fragmentation at the XXIII Intl. Conf. on HEP, July 16-23, 1986, Berkeley.

[46] Torbjörn Sjöstrand. The Lund monte carlo for jet fragmentation and e^+e^- physics: JETSET version 6.2. Technical report, Dept. Theoretical Physics, Univ. of Lund, Sweden, October 1985. LU TP 85-10.

[47] G. Ingelman. LEPTO: The Lund monte carlo for deep inelastic lepton-nucleon scattering. Technical report, Theory Group, DESY, Hamburg.

[48] Daniel Mark Coffman. *The Properties of Semileptonic Decays of Charmed D Mesons*. PhD thesis, California Institute of Technology, Pasadena, Calif., 1987. Submitted Dec. 8, 1986; CALT-68-1415.

[49] R. Brun, F. Bruyant, M. Maire, A.C. McPherson, and P. Zanarini. GEANT3. Technical Report DD/EE/84-1, CERN, May 1986.

[50] H. Fesefeldt. The simulation of hadronic showers - physics and applications -. Technical report, Physikalisches Institut, RWTH Aachen, FRG, 1985.

[51] A. Van Ginnekin. Energy loss and angular characteristics of high energy electromagnetic processes. *NIM*, A(251):21–39, 1986.

[52] Michael Albert Tartaglia. *A Measurement of the Elastic Scattering Cross Section, $\nu_\mu + e^- \rightarrow \nu_\mu + e^-$*. PhD thesis, Massachusetts Institute of Technology, 1984. Submitted July. 6, 1984.

[53] M. Tartaglia. Hadron calorimetry with proportional tubes in E-733 at Fermilab. In *Proc. Gas Sampling Calorimetry Workshop II*, pages 256–290. Fermi Nat. Accel. Lab., August 1986.

[54] Womersley et al. Hadron showers in a low-density fine-grained flash chamber calorimeter. *NIM*, A(267):46–68, 1988.

[55] A. Benvenuti et al. Further observation of dimuon production by neutrinos. *Phys. Rev. Lett.*, 35(18):1199–1202, 3 Nov. 1975.

[56] A. Benvenuti et al. Rates and properties of opposite-sign dimuons from neutrinos and antineutrinos. *Phys. Rev. Lett.*, 41(18):1204–1206, 30 Oct. 1978.

[57] T. Trinko et al. Yield of prompt like-sign dimuons from neutrino interactions. *Phys. Rev. D*, 23(9):1889–1894, 1 May 1981.

[58] M. Holder et al. Like-sign dimuon events produced in narrow-band neutrino and antineutrino beams. *Phys. Lett.*, 70B(3):396–398, 10 Oct 1977.

[59] J.G.H. de Groot et al. Investigation of like-sign dimuon production in neutrino and antineutrino reactions. *Phys. Lett.*, 86B(1):103–107, 10 Sept. 1979.

[60] K. Nishikawa et al. Observation of prompt like-sign dimuon production in neutrino reactions. *Phys. Rev. Lett.*, 46(24):1555–1559, 15 June 1981.

[61] K. Nishikawa et al. Errata: Observation of prompt like-sign dimuon production in neutrino reactions. *Phys. Rev. Lett.*, 54(12):1336, 25 Mar 1985.

[62] M. Jonker et al. Experimental study of opposite-sign and same-sign dimuon events produced in wide-band neutrino and antineutrino beams. *Phys. Lett.*, 107B(3):241–248, 10 Dec 1981.

[63] H. Burkhardt et al. Are there "prompt" like-sign dimuons? *Z. Phys.*, C(31):39–49, 1986.

[64] W.K. Sakumoto et al. Neutrino production of same sign dimuons at the Fermilab Tevatron. In *DPF '92, Batavia, IL*, page 935:937, Nov. 11-14 1992.

[65] Computing Application Software Group and CERN Networks Division. MINUIT function minimization and error analysis, v92.1. Technical Report CERN Program Library Long Writeup D506, CERN, March 1992.

[66] Constantinos Foudas. *Neutrino Production of Opposite Sign Dimuons at the FNAL Tevatron*. PhD thesis, Columbia University, Irvington, NY, 1989. R-1421,CU-378,NEVIS-272.

[67] Steven Alan Rabinowitz. *Opposite Sign Dimuon Production in Neutrino Interactions at the Femilab Tevatron*. PhD thesis, Columbia University, Irvington, NY, 1992. R-1486,CU-385,NEVIS-279.

[68] U. Baur et al. The charm content of $W + 1$ jet events as a probe of the strange quark distribution function. preprint, FSU,UW Madison, INFN, Aug. 1993. FSU-HEP-930816; MAD/TH/93-6; MAD/PH/788; hep-ph/9308370.

[69] T.P. Cheung and Wu-Ki Tung. General local interactions and tests of $V - A$ theory in neutrino scattering processes. *Phys. Rev. D*, 3(3):733–744, 1 Feb. 1971.